UNIVERSIDADE FEDERAL DE SANTA CATARINA
PROGRAMA DE PÓS-GRADUAÇÃO EM ENGENHARIA MECÂNICA

INTERFERÔMETROS ROBUSTOS APLICADOS À MEDIÇÃO DE DESLOCAMENTOS RADIAIS EM CILINDROS INTERNOS USANDO HOLOGRAFIA ELETRÔNICA

TESE SUBMETIDA Á UNIVERSIDADE FEDERAL DE SANTA CATARINA PARA OBTENÇÃO DO GRAU DE DOUTOR EM ENGENHARIA MECÂNICA

Meinhard Sesselmann

Florianópolis, outubro 2000

INTERFERÔMETROS ROBUSTOS APLICADOS À MEDIÇÃO DE DESLOCAMENTOS RADIAIS EM CILINDROS INTERNOS USANDO HOLOGRAFIA ELETRÔNICA

Meinhard Sesselmann

Esta tese foi julgada adequada para obtenção do título de

"DOUTOR EM ENGENHARIA "

Especialidade ENGENHARIA MECÂNICA –
Área de concentração METROLOGIA E INSTRUMENTAÇÃO,
e aprovada em sua forma final pelo PROGRAMA DE PÓS-GRADUAÇÃO EM ENGENHARIA MECÂNICA

.....
Prof. Armando Albertazzi Gonçalves Jr., Dr.Eng.
ORIENTADOR

.....
Prof. Júlio César Passos, Dr.
COORDENADOR DO PROGRAMA DE PÓS-GRADUAÇÃO

BANCA EXAMINADORA

.....
Prof. Armando Albertazzi Gonçalves Jr., Dr.Eng.

.....
Prof. Alexander Nickolayvich Titov, Ph.D.

.....
Prof. Frank Hrebabetzky, Dr.rer.nat.

.....
Prof. Guillermo Héctor Kaufmann, D.Sc.

.....
Prof. Marco Antonio Martins Cavaco, Ph.D.

AGRADECIMENTOS

- ao meu filho e a minha esposa pelo grande apoio e compreensão

- ao técnico Danilo J. Santos pelo apoio na parte experimental

- à estudante Fernanda Assuiti pelo apoio na programação de software e na fabricação do multiplexador

- ao Prof. Armando Albertazzi Gonçalves Jr. por sua contribuição na qualidade de orientador

- ao Prof. Frank Hrebabetzky pelas constantes discussões

- a todos os amigos e colegas do LABMETRO/CERTI que diretamente ou indiretamente contribuiram para a realização deste trabalho

CONTENTS

Constants

$\vec{d}$	Displacement vector of the object
$\vec{e}$	Unitary vector
$\vec{E}$	Electrical field strength
$\vec{k}$	Wave vector
$\vec{m}$	Unitary vector
$\vec{n}_i$	Unity vector with origin at the object pointing to the illuminating source
$\vec{n}_o$	Unity vector with origin at the object pointing to the entrance pupil of the observation system
$\vec{r}$	Spatial location vector
$\vec{S}$	Sensitivity vector of the interferometer

Φ	Initial phase of speckle
δ	Phase due to object displacement
γ	Complex degree of coherence
λ	Wavelength of light
β	Optical magnification
σ	Standard deviation
ρ	Out-of plane rotation of object
ρ	Density
φ	Rotation angle
η	Intensity noise
ψ	Angle between linear polarizations
ε	Phase-step error
α	Phase step
Δ	Uncertainty, misalignment
κ	Dilatation coefficient
θ, r	Polar coordinates
ε_{max}	Maximum angle of incidence
Φ_{max}	Maximum tolerable phase change during CCD integration
Φ_v	Phase vibration due to mechanical vibration

Δx, Δy	Lateral rigid body motion/shear
A_v	Amplitude of mechanical vibration
A, B	Index of observation channel
a	Fiber core diameter
B	Monitor brightness
c	Correlation coefficient
c	Vacuum speed of light
D	Aperture diameter
E_{max}	Maximum error
f	Focal length
f	Frequency of laser light
F	Normalized frequency
$f^{\#}$	Aperture number
FO	Fringe order
f_v	Frequency of mechanical vibration
$f_{x,y}$	Spatial (carrier) frequency
GP	Geometric path length
I	Intensity
K	Proportional constant
k	Number of phase steps
l	Object to lens distance
LSB	Least significant bit
m	Integer number
m	Modulation of phase components
n	Number of bits
n	Index of refraction
NA	Numeric aperture
n_e	Electronic noise of CCD camera
OP	Optical path length
Q	Quantization
r	Intensity ratio between object and reference beam
R	Radius of specimen cylinder
s	Geometric path along a light beam
SNR	Signal to noise ratio
T	Period of mechanical vibration
T	Temperature,
t	Time
u	In-plane motion
v	Propagation velocity of light
V	Visibility
V_{sub}	Visibility of subtraction correlation fringes
w	Out-of plane displacement of object
w_r	Out-of plane displacement in radial direction of object
x, y, z	Spatial coordinates

Robust Interferometers for the Measurement of Radial Displacements of Internal Cylinder Surfaces by Electronic Speckle Pattern Interferometry

Abstract

The principle of a measurement system is described that is capable to measure radial displacements of the interior surface of hollow cylindrical work pieces in the submicrometer range using phase-shifting Electronic Speckle Pattern Interferometry (ESPI). The behavior of this particular measurement system against typical disturbances is analyzed and a simplified model of its measurement error is derived. A new phase-shifting algorithm for phase-difference determination and several modifications of the arrangement of conventional out-of-plane sensitive interferometers are proposed and analyzed in detail. These modifications make measurements of radial displacements feasible outside the laboratory in an industrial environment.

Keywords: speckle interferometry, electronic speckle pattern interferometry, spatial phase-stepping, robust interferometers, measurement in adverse conditions
94 pages

Interferômetros Robustos Aplicados à Medição de Deslocamentos Radiais em Cilindros Internos usando Holografia Eletrônica

Resumo

Este trabalho descreve os princípios de um sistema de medição capaz de medir deslocamentos radiais em superfícies cilíndricas internas usando holografia eletrónica e deslocamento de fase. O comportamento deste sistema de medição em relação à perturbações típicas é analisado e um modelo simplificado do erro de medição é desenvolvido. Um novo algoritmo para deslocamento de fase e modificações na configuração convencional dos interferômetros sensíveis a deslocamentos fora do plano são propostos e seu desempenho analisado detalhadamente. Estas modificações tem como objetivo viabilizar medições de deslocamentos radiais fora do laboratório ótico em condições ambientais típicas de chão de fabrica.

Palavras-chave: interferometria speckle, holografia eletrónica, passos de fase paralelos, interferômetros robustos, medição em ambientes desfavoráveis
94 páginas

1 Introduction

1.1 Localization within the scientific context

In the last decades many optical methods have been developed for non-contact inspection. But most techniques have been applied to study outer surfaces. More recently new techniques were introduced in order to accomplish non-contact inspection of interior surfaces like for hollow cylindrical work pieces.

Reported applications include the detection of surface defects [57] and deformation measurement [14, 45] among others. Especially the possibility to measure radial deformations in the submicrometer range has attracted considerable interest of automotive and other industries since it might help to solve a variety of problems in R & D, experimental mechanics and quality control.

Whatever the technique is for internal inspection, it requires a panoramic view of the specimen surface. Such systems for panoramic imaging have been developed for more than 100 years[13]. They can be classified in two main groups: those which rotate (part of) the imaging device to scan the area of interest and those compound systems consisting of several optical elements that obtain a single panoramic view. The many drawbacks of both scanning and compound systems led to the development of the Panoramic Annular Lens (PAL) [18], which consists only of a single piece of glass with spherical surfaces to capture a panoramic image.

In order to measure submicrometer displacements of internal cylinder surfaces, the PAL was combined with Holography [14]. However quantitative analysis of fringe patterns was found to be rather difficult, mainly due to non-uniform sensitivity generated by the PAL.

If one is only interested in the radial displacement component, the optical system can be drastically simplified [16]. At our department the PAL was replaced by a conical mirror for radial-only illumination and observation and Electronic Speckle Pattern Interferometry (ESPI) instead of Holography was applied as a standard optical technique to obtain quantitative measurement data.

Because of the high sensitivity of the applied interferometer to environmental instabilities, the resultant measurement system has been proved to work successfully under laboratory conditions only. That means the specimen has to be transported to the laboratory where the measurements can be taken isolated from ground vibrations on an optical table under well controlled ambient conditions.

However, there are many cases where transportation of the specimen to the laboratory is either not possible or too costly. Therefore it would be highly desirable to measure "in situ", i.e. in an industrial environment like found on the shop floor.

For such a harsh environment several robust interferometers have been proposed. They are based on fringe tracking [20], phase-shifting in the video blanking interval [63], or spatial phase-shifting [38], to name just a few. The common approach of the techniques mentioned above is to freeze the dynamic disturbances by rapid data acquisition into unique fringe patterns that can be recognized and compensated.

However present systems still show serious limitations creating space for innovations. For example, active feedback systems [58] may compensate only piston type mechanical vibrations between the interferometer head and flat external surfaces. Yet, they can neither compensate tilt vibrations of the specimen nor vibrations between the internal cylinder surfaces and the device used for its panoramic inspection.

To make radial displacement measurement of such surfaces feasible in an industrial environment, an alternative robust interferometer for that particular ESPI system needs to be developed that is insensitive to environmental changes, typically found for light manufacturing.

1.2 The problem

Being focused on ESPI systems that measure radial displacements of internal cylinder surfaces, the work of this thesis is to conceive, develop, evaluate and optimize an interferometer capable of measuring satisfactorily in an industrial environment, typically found for light manufacturing.

As a result, a prototype interferometer should be constructed that has been tested and qualified.

1.3 About this work

This work is summarized in eight chapters. After this brief introduction, the necessary theoretical background will be given in chapter 2. It consists, basically, of an analysis of an existing measurement system with respect to static and dynamic disturbances. For this measurement system, routinely used in the laboratory for measurements of radial displacements in internal cylinder surfaces, a simplified model of measurement error is derived. Finally, conclusions are drawn for the design of robust interferometers.

Based on this theoretical conclusions to narrow bibliographic research, chapter 3 gives a brief overview on the state of art for the design of robust interferometers. The applicability, advantages and disadvantages of the various techniques and methods are discussed, further details for the design of robust interferometers are concluded and space for innovation is outlined. The following chapters intend to fill this space.

Chapter 4 describes the proposed new phase-step algorithm designed for spatial phase-stepping ESPI. An error analysis is included that studies the behavior of the algorithm to various system error sources by means of numerical simulation. From the analysis, some important conclusions are drawn for a successful experimental implementation of this algorithm in a new interferometer.

The configuration and alignment of the resulting new spatial phase-stepping ESPI system is detailed in chapter 5. The results of its experimental evaluation are presented in chapter 6 which also points out the present system limitations.

Possible alternatives to overcome these problems are given in chapter 7 where the concepts of an portable ESPI system are described. Finally, in chapter 8 are summarized basic conclusions of this work. Included in this chapter are a brief outlook to future progress, that might be expected for the use of ESPI in adverse conditions, and some suggestions made for future research.

2 Theory

2.1 Principle of Electronic Speckle Pattern Interferometry (ESPI)

ESPI, that represents only a few out of a range of possible optical configurations in Speckle Interferometry, utilizes speckles to achieve information about the object surface [5, 40].

Speckles are generated by the interference of coherent light scattered from different points on an optically rough surface [17]. This information can relate to relative displacement under load, strain, shape or vibration characteristics of the object surface.

The displacement information is interferometrically encoded either by superposing the speckle pattern with a second speckle pattern or by mixing it with a smooth reference beam. The resulting two-dimensional interference pattern is captured by the CCD sensor of a camera. Because of the low spatial resolution of the CCD (about 10 μm pixel size) the angle between object and reference beam has to be as small as possible when superposed. This is accomplished by making the wave vectors $\vec{k}_O, \vec{k}_R$ collinear which is referred to as in-line reference in literature. To obtain temporally stable interference patterns only waves of equal frequency are superposed. As a result, the interference phase in equation (A6) simplifies to Φ which denotes the (spatial) random phase difference between object and reference wave.

The intensities of object and reference beam are affected by, mainly, non-uniform illumination and/or reflection. Hence all quantities in the equation describing interference (A6) become variables of *x,y*-pixel position on the CCD target. For convenience the *x,y*-pixel position will always be dropped in further mathematical description.

To measure displacements between deformation states, an exposure of interference pattern is taken by the CCD camera with the object in the undeformed state and the frame is stored in the computer. The resulting speckle intensities are

$$I_1 = I_m(1 + V\cos\Phi) \tag{2.1}$$

Then the object is deformed and another exposure is taken. The corresponding intensity equation is

$$I_2 = I_m(1 + V\cos(\Phi + \delta)) \tag{2.2}$$

where δ carries the information of the object displacements. It is reasonable to assume that Φ will remain constant during small displacements, as it depends only on the reference and object waves and the object surface roughness.

ESPI working with continuous-wave laser is most commonly used in the subtraction mode. The equation governing this mode follows from equations (2.1) and (2.2). The result is a speckled fringe pattern of the form

$$I_{sub} = I_1 - I_2 = I_m V[\cos\Phi - \cos(\Phi + \delta)] = 4\sqrt{I_O I_R}\,|\gamma|\sin\left(\Phi + \frac{\delta}{2}\right)\sin\left(\frac{\delta}{2}\right) \tag{2.3}$$

This signal contains positive and negative values. The television monitor will, however, display negative values as total blackness. To avoid such a loss, the signal is squared and the brightness B on the monitor, proportional to I_{sub}^2, can be expressed as

$$B = 16\mathrm{K} I_{\mathrm{O}} I_{\mathrm{R}} |\gamma|^2 \sin^2\left(\Phi + \frac{\delta}{2}\right) \sin^2\left(\frac{\delta}{2}\right) \tag{2.4}$$

where K is a proportional constant. The brightness is maximum when $\delta = (2m+1)\pi$ and minimum when $\delta = 2m\pi$, m being an integer. Therefore bright and dark fringes are formed on the monitor.

Equation (2.4) shows that there are fringes due to the information carrier phase δ as well as due to the random speckle phase $\Phi+\delta$. The high spatial frequency of the latter term causes modulation of the information carrier and thus makes the fringes noticeably noisy especially around maximum brightness.

Another approach to interpret the intrinsically noisy fringes generated by ESPI is given by Jones and Wykes [32]. By introducing a correlation coefficient of the speckle patterns between two exposures (undeformed and deformed state) it can be shown that maximum correlation is achieved if $\delta = 2m\pi$, whereas the two speckle patterns become completely uncorrelated if $\delta = (2m+1)\pi$, m being an integer.

This also explains why subtraction mode is most commonly used in static displacement measurements. Subtraction fringes have intrinsically better visibility, since their minimum show zero intensity, while addition fringes do not.

2.1.1 Conventional ESPI system for measurement of out-of-plane displacements

The conventional ESPI system for measurement of out-of-plane displacements is sketched in Figure 2.1a. It is based on a Mach-Zehnder interferometer. After the laser light is divided into reference and object beams by a beam splitter, the scattered light from the object is imaged through a lens onto the CCD sensor of the camera. The (spatially filtered) reference beam is mixed in-line to the object beam by a beam combiner. The video signal from the CCD camera is processed via frame grabber and computer to be displayed on the TV monitor.

Another practical set-up, where the strict alignment problems of the previous interferometer are released, is shown in Figure 2.1b. The Mach-Zehnder set-up is substituted by a Twyman-Green interferometer where beam division and recombination is merged together in one single beam splitter. However, the simpler set-up combines two noisy speckle patterns which lead to poorer fringe visibility.

The computer allows subtraction of consecutively grabbed speckle patterns in real-time. The result, displayed as correlation fringe pattern, shows the displacement encoded in the phase change δ. The relation between the displacement and the phase change δ is [15]

$$\delta = \frac{2\pi}{\lambda} \vec{S} \cdot \vec{d} \tag{2.5}$$

where λ is the wavelength of laser light, $\vec{S}$ is the sensitivity vector and $\vec{d}$ is the displacement vector. The sensitivity vector is the summation of the unitary vectors $\vec{n}_{\mathrm{o}}$ and $\vec{n}_{\mathrm{i}}$ pointing in direction of observation and illumination respectively. The dot product in equation (2.5) indicates that only displacement components in direction to $\vec{S}$ contribute to a phase shift δ.

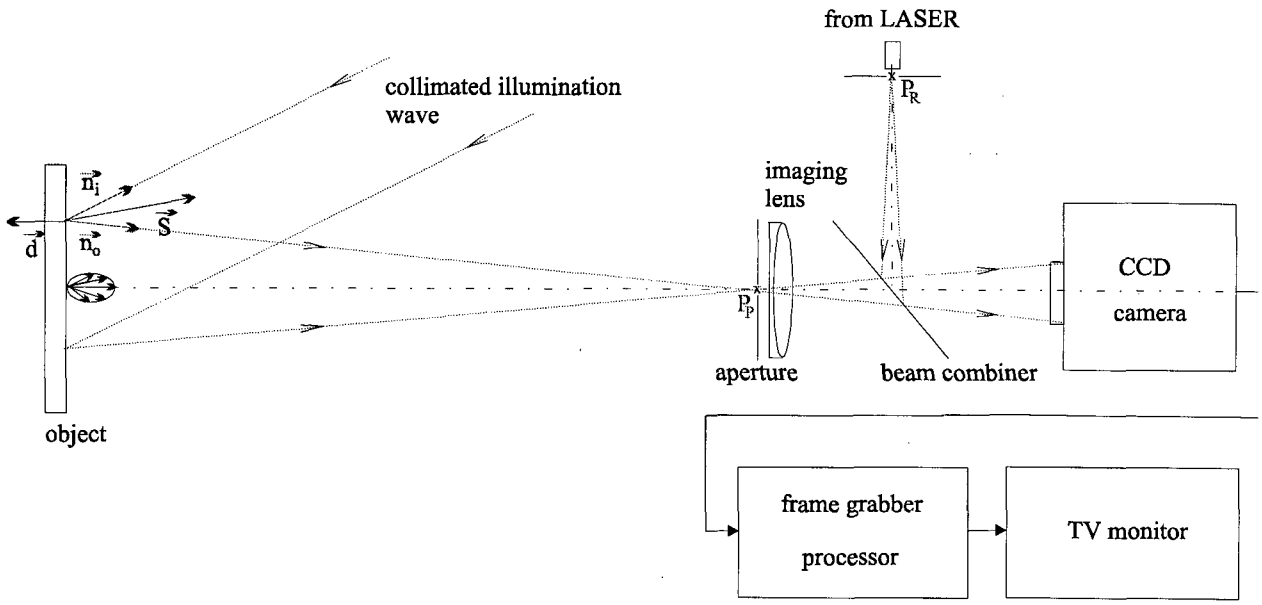

Figure 2.1a Classical ESPI system using smooth in-line reference

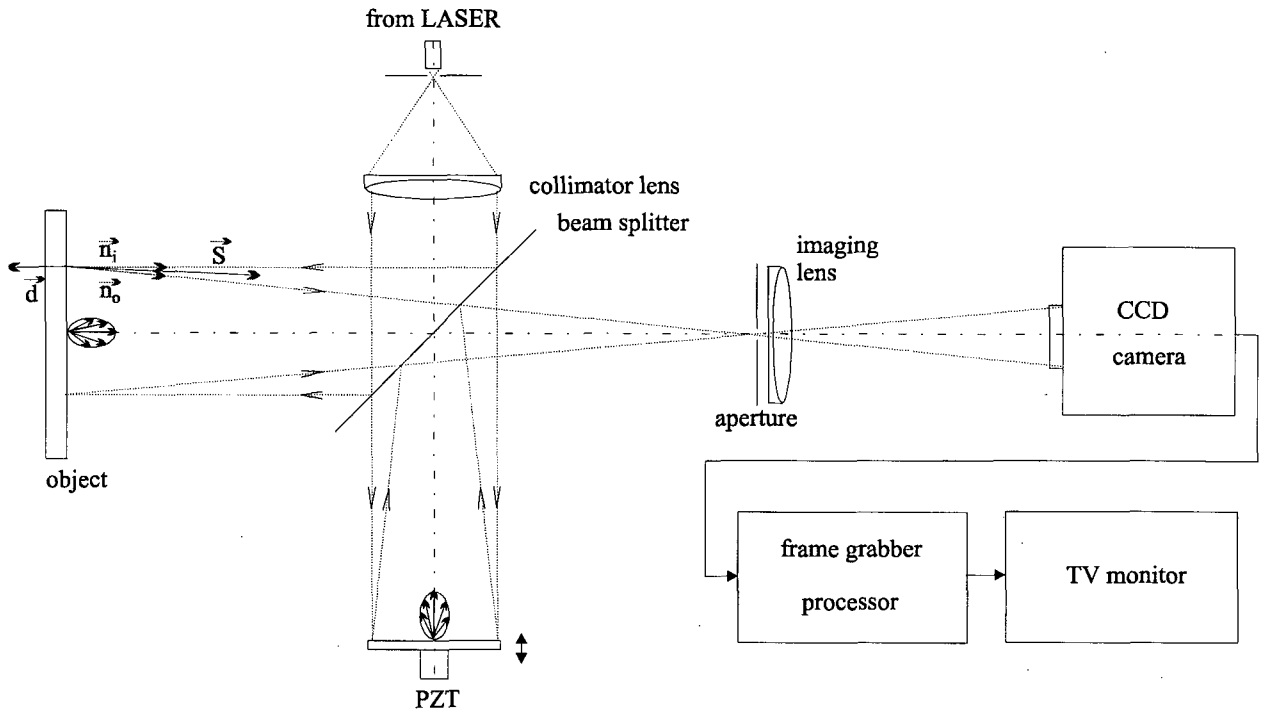

Figure 2.1b Classical ESPI system using speckled reference

The maximum sensitivity is reached when the unitary vectors $\vec{n}_i$ and $\vec{n}_o$ become collinear. If they are, in addition, perpendicular to the surface of the object under study (quasi accomplished for interferometer in Figure 2.1b, fringes of pure out-of-plane displacement are generated by the interferometer and equation (2.5) can be simplified to

$$\delta = \frac{4\pi}{\lambda} w \tag{2.6}$$

where w is the out-of-plane component of $\vec{d}$. Note that phase term and deformation vector or component are also spatially dependent variables, whereas the sensitivity vector can be approximated to be constant for sufficient large ratios of object distance to object size.

2.1.2 ESPI system for measurement of radial displacements of internal cylinder surfaces

The measurement of radial surface displacements of hollow cylinders with ESPI was first investigated by Goçalves Jr.[15] The successfully applied interferometer set-up is shown in Figure 2.2. The principal optical element is a conical mirror (45°) which is placed inside the cylinder. If the conical mirror is properly aligned to the camera and cylinder axis, it allows radial illumination and (in a good approximation) radial observation of the internal cylinder surface simultaneously. This way maximum sensitivity is reached and only radial displacement components w_r contribute to phase changes δ.

$$\delta = \frac{4\pi}{\lambda} w_r \tag{2.7}$$

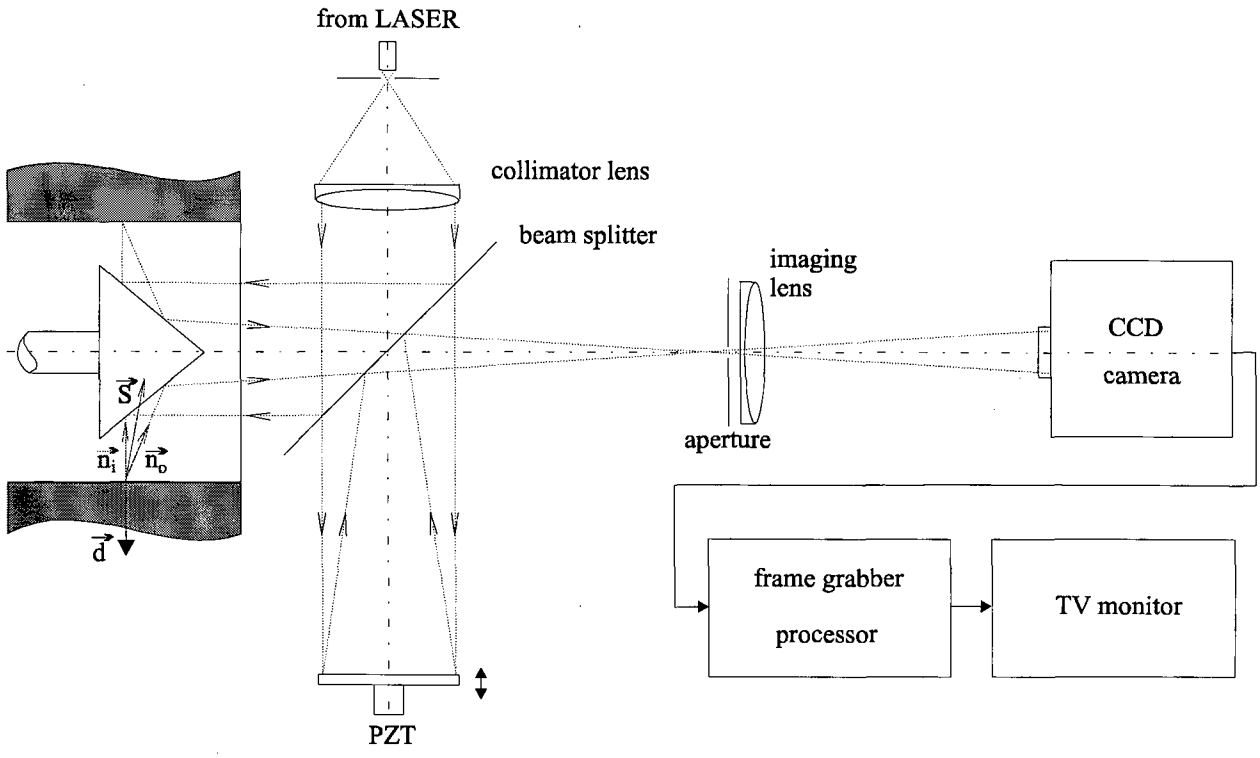

Figure 2.2 ESPI system proposed by Gonçalves Jr. for measurement of radial displacements of internal cylinder surfaces

2.2 Static disturbances affecting fringe quality

Since the displacement information is encoded in the speckle correlation fringes, it is important to achieve a good fringe quality to minimize measurement errors.

Therefore, it is necessary to know the principal disturbances which may contribute to a deterioration of fringe quality. The study analyzes the influence of those static disturbances that are typically found in a laboratory environment.

Fringe contrast or visibility and signal to noise ratio are usually utilized to quantify the quality of fringes in the presence of disturbances. The visibility V_{sub} and signal-to-noise ratio SNR of correlation fringes in ESPI-subtraction mode can be expressed as [48]

$$V_{sub} = \frac{\langle (I_1 - I_2)^2 \rangle_{max} - \langle (I_1 - I_2)^2 \rangle_{min}}{\langle (I_1 - I_2)^2 \rangle_{max} + \langle (I_1 - I_2)^2 \rangle_{min}}; \quad SNR = \frac{\langle (I_1 - I_2)^2 \rangle_{max}}{\langle (I_1 - I_2)^2 \rangle_{min}} \tag{2.8}$$

where $\langle (I_1 - I_2)^2 \rangle_{max}$ is the maximum mean intensity (along lines of minimum speckle correlation) and $\langle (I_1 - I_2)^2 \rangle_{min}$ is the minimum mean intensity (along lines of maximum speckle correlation).

However, unless decorrelation of speckle pattern through deformation is considered, the visibility of correlation fringes as defined in equation (2.8) will always yield unity, i.e. the signal-to-noise ratio would be infinite. This stems from the fact that, so far, only noise free conversion of illumination into monitor brightness was assumed.

But any type of camera requires a certain minimum intensity to give rise to a camera voltage which can be detected above background electronic noise. The noise is specified by the manufacturer and will be represented here as n_e in % (for SNR of reasonable cameras > 50 dB that yields n_e< 0.3 %).

Hence, whenever the normalized average minimum of correlation fringes is (theoretically) below the level of electronic noise, one has to substitute $\langle (I_1 - I_2)^2 \rangle_{min} / 2\langle I \rangle^2$ by n_e in equation (2.8), $\langle I \rangle = \langle I_1 \rangle = \langle I_2 \rangle$ denoting the average intensity of one speckle pattern.

$$V_{sub} = \frac{\langle (I_1 - I_2)^2 \rangle_{max} - \frac{n_e}{100\%} \cdot 2\langle I \rangle^2}{\langle (I_1 - I_2)^2 \rangle_{max} + \frac{n_e}{100\%} \cdot 2\langle I \rangle^2}; \quad SNR = \frac{\langle (I_1 - I_2)^2 \rangle_{max}}{\frac{n_e}{100\%} \cdot 2\langle I \rangle^2} \tag{2.9}$$

The fringe visibility is maximized when the signal-to-noise ratio is maximum.

2.2.1 Speckle size

The pixel size of the CCD sensor defines the minimum speckle size that can be resolved by the camera. With increasing deformation the fringe spacing decreases until it reaches the resolvable speckle size and fringe visibility drops down to zero [32]. Hence the higher the spatial resolution of the CCD the higher will be the fringe visibility for a constant fringe spacing caused by a given deformation.

The limited spatial resolution of CCD sensors introduces a sampling of continuous intensity signal. From the Nyquist criterion for digital sampling it follows that the maximum spatial frequency in the speckle pattern should be less than half the spatial frequency of the photo detectors on the CCD array. It is not necessary to strictly satisfy this condition since higher frequencies are aliased into lower frequencies which, still, contribute useful data to the speckle pattern [32]

In general, it is acceptable to let the minimum size of speckles be the same of the picture cells (pixels) on the CCD. Most commonly, the speckle size is controlled by the entrance pupil of the imaging system. The optimal adjustment of the so called subjective speckle is governed by the equation [12]

$$\text{speckle size} = \text{pixel size} \quad , \quad f^{\#} = \frac{\text{pixel size}}{\lambda \cdot (1+\beta)} \tag{2.10}$$

with $f^{\#}$ denoting the aperture number (f-number) and β indicating the optical magnification. For typical values λ = 632.8 nm, pixel size = 10 μm (active area) and magnifications varying from unity to zero the aperture should be set in the range from 8 to 16. Higher f-numbers will increase the speckle size and, hence, lower maximum fringe spacing and fringe visibility.

From equation (2.10) it can be readily seen that higher spatial resolution of CCD (lower pixel size) allows the use of larger lens apertures (smaller f-numbers), thus, collecting more light. This fact becomes especially important when larger structures have to be studied with acceptable fringe visibility but with limited laser power.

2.2.2 Intensity ratios

The choice of object and reference intensities should be such that the overall intensity of the speckled patterns is just below the saturation level of the camera. If one defines the intensity deviation of these speckle patterns to be $\sigma_I = \langle I^2 \rangle - \langle I \rangle^2$ together with the condition

$$I_{sat} = \langle I \rangle + 2\sigma_I \tag{2.11},$$

the camera will operate below saturation over 95% of the image [32]. Then the intensity ratios including the mean reference intensity $\langle I_R \rangle$, mean object intensity $\langle I_O \rangle$ and saturation intensity I_{sat} can be shown to be[48]

$$\frac{I_{sat}}{\langle I_R \rangle} = 1 + r + 2\sqrt{1+r^2}; \quad r = \frac{\langle I_O \rangle}{\langle I_R \rangle} \text{ speckled reference} \tag{2.12a}$$

$$\frac{I_{sat}}{I_R} = 3 + r \quad ; \quad r = \frac{\langle I_O \rangle}{I_R} \text{ smooth reference} \tag{2.12b}$$

with r indicating the ratio of object-to-reference intensity.

The interference term should make good use of the dynamic range of the camera, i.e. the visibility V in equations (2.1) and (2.2) should be as close as possible to unity which is satisfied when r is unity $(\langle I_R \rangle = \langle I_O \rangle)$. Then equation (2.12a) states that the mean intensities of the individual beams should be about 20% of the intensity for which the camera saturates. If a smooth reference is used, their intensity should increase to 25% (like in classical interferometry). In the latter case the fringe quality can be further increased by choosing r smaller than unity. This was first investigated by Jones and Wykes [32]. By optimization of the signal-to-noise ratio they showed that, for a smooth reference beam, the optimum ratio of object-to-reference intensity yields 0.59.

Another, more comprehensive, treatment of the problem is given by M. Owner-Petersen [49]. All studies indicate that inproper intensity ratio may have large influence upon fringe visibility (see also Figure 2.3). However, these theoretical studies do not explain satisfactorily the experimental experience that the decrease of visibility with intensity unbalance is much weaker for a smooth reference than it is for a speckled one. In fact, smooth reference is quite robust to intensity unbalance. Some authors state ratios of reference-to-object intensity larger than twenty, still achieving a reasonable fringe visibility [31]. When a speckled reference beam is used instead, this ratio should be near unity.

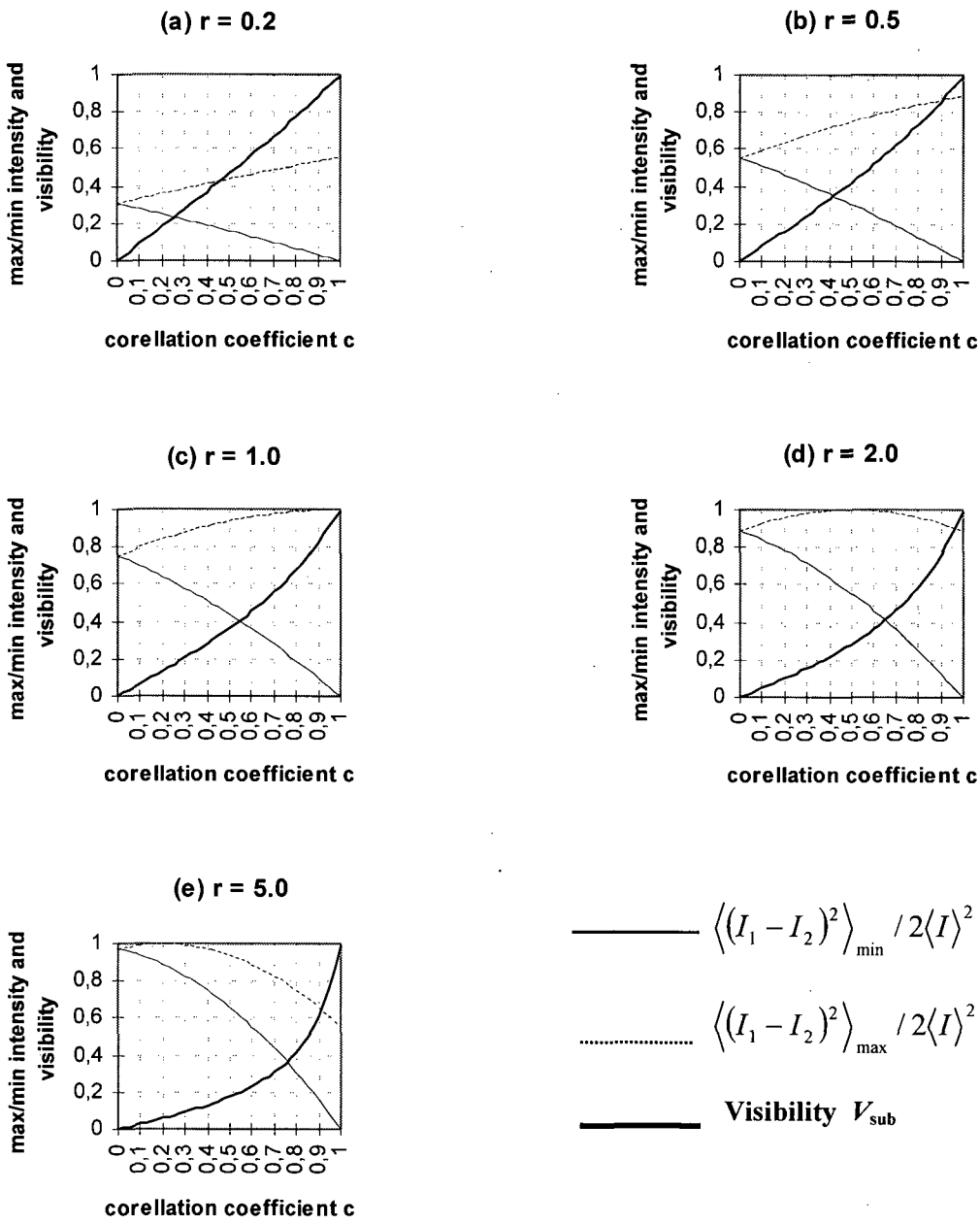

Figure 2.3 Influence of intensity ratio r upon visibility of correlation fringes (Owner-Petersen)

2.2.3 Speckle decorrelation

So far, it has been assumed that the random amplitude and phase of individual speckles in equation (2.1) do not alter significantly with deformation and inevitable rigid body motions caused by the loading process.

However, this approximation is only valid until such displacements reach a certain value. Further displacement causes the random amplitude and phase to change until the speckle patterns become totally uncorrelated and fringe visibility drops down to zero.

The relationship between deformation and decorrelation was studied by Jones and Wykes [32] and Owner-Petersen [48]. The latter describes out-of-plane deformation in form of a tilt and derives useful information about fringe visibility for varying intensity ratios and deformations (decorrelations). Some results of this source are shown in Figure 2.4. The maximum tilt angle ρ_{max} is reached when the correlation coefficient c is zero [48]

$$\rho_{max} = \frac{D}{2 \cdot l} = \frac{1}{2f^{\#}} \cdot \frac{\beta}{\beta + 1} \tag{2.13}.$$

where l denotes the object to lens distance and D the aperture diameter. Equation (2.13) states that the smaller the magnification β the less the tolerance to out-of-plane rotation.

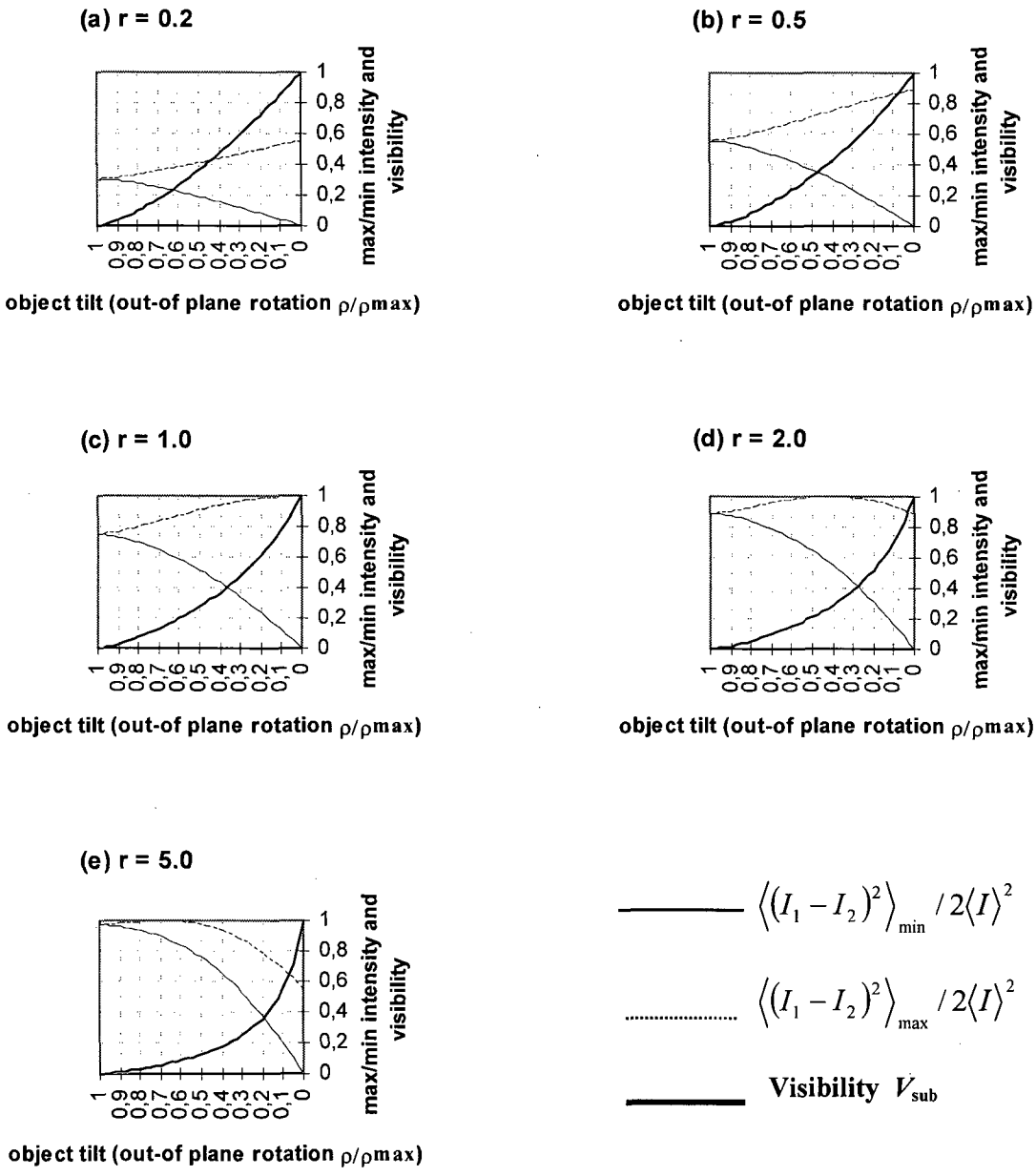

Figure 2.4 Influence of decorrelation upon visibility of correlation fringes (Owner-Petersen)

It should be emphasized that the results in Figure 2.4 represent best cases for out-of-plane sensitive ESPI interferometers. Merely decorrelations under load were considered. In-plane and/or out-of plane rigid body motions will further deteriorate the visibility of correlation fringes.

The relationship for maximum out-of-plane rigid body motion w_{max} yields [32]

$$w_{max} = \sqrt{2\,l\,\lambda} \tag{2.14}$$

The smaller this distance the smaller the tolerance to out-of plane rigid body motions. The maximum in-plane rigid body motion u_{max} yields [48]

$$u_{max} = 1.22 \cdot \frac{\lambda \cdot l}{D} = 1.22 \cdot \lambda \cdot f^{\#}\left[\frac{\beta + 1}{\beta}\right] \tag{2.15}.$$

Here, the higher the magnification the smaller the tolerance to in-plane rigid body motion.

2.2.4 Complex degree of coherence

The complex degree of coherence can be approximated to be a product of temporal and spatial coherence[12]. Thus, $|\gamma|$ can be calculated for a given laser source and interferometer set-up.

A loss of spatial coherence in out-of-plane sensitive ESPI is assumed to be less critical. Apart from that, in classical interferometers, the temporal coherence is kept at unity by proper control of the reference and object arm lengths. However, the knowledge of $|\gamma|$ becomes particularly important when limits of quasi-equal-path interferometer set-ups have to be studied.

Extending the theoretical constraint of Owner-Petersen the maximum and minimum intensities and the visibility V_{sub} can be calculated as functions of object to reference intensity ratio r, correlation $|c|$ (hence also for decorrelation under load ρ/ρ_{max}) and the complex degree of coherence $|\gamma|$.

$$\left\langle (I_1 - I_2)^2 \right\rangle_{max} = 2\langle I \rangle^2 \left[\frac{(1+|c|)(r^2(1-|c|)+2r\gamma^2)}{(1+r)^2}\right] \tag{2.16a}$$

$$\left\langle (I_1 - I_2)^2 \right\rangle_{min} = 2\langle I \rangle^2 \left[\frac{(1-|c|)(r^2(1+|c|)+2r\gamma^2)}{(1+r)^2}\right] \tag{2.16b}$$

$$V_{sub} = \frac{2|c|\gamma^2}{r(1-c^2)+2\gamma^2} \tag{2.16c}$$

Some results are summarized in Figure 2.5 as examples.

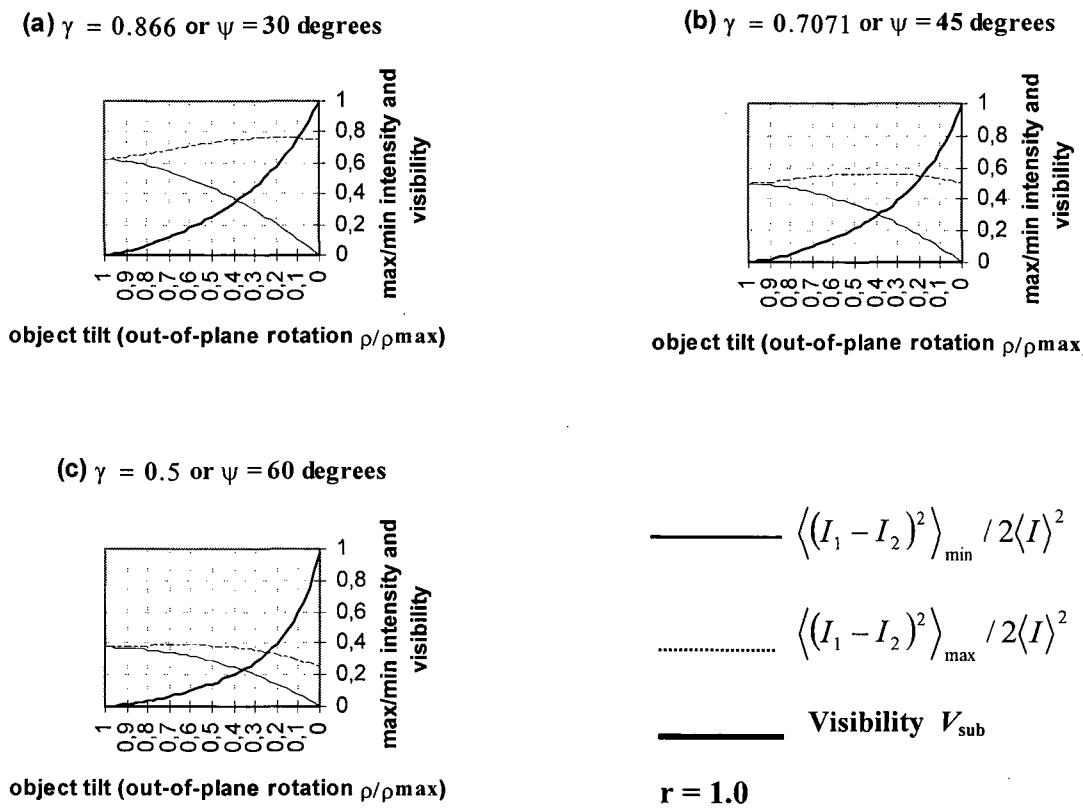

Figure 2.5 Influence of coherence and polarization upon visibility of correlation fringes

2.2.5 Polarization

The simplification made in equation (A4) assumes that waves of equal linear polarization are superposed. The photo detectors on the CCD matrix are not sensitive to polarization. Hence, whenever linear polarization of object and reference wave deviate from above assumption the visibility V from equation (A7) will be decreased by an additional factor $\cos\psi$ to give

$$V = \frac{2\sqrt{I_O I_R}}{I_O + I_R} |\gamma| \cdot |\cos\psi| \tag{2.17}$$

where ψ denotes the angle between linear polarization states. Such an unwanted angle could be introduced by reflections at (and transmission through) dielectric surfaces under oblique angle or total internal reflections with polarization states different than parallel or perpendicular to the plane of incidence [19], to name just a few.

From equation (2.17) it can be readily seen that when orthogonally polarized waves are superposed ($\psi = 90°$), the visibility yields zero and no interference effect will be observed in equations (A6), (2.1) and (2.2).
The effect of angle ψ on the maximum and minimum intensities as well as the visibility of correlation fringes can be quantified by substituting γ^2 by $\gamma^2 \cdot \cos^2\psi$ in equations (2.16a-c). Figure 2.5 gives some examples.

2.2.6 Misalignment

Misalignment of mechanical parts of the interferometer may further deteriorate the fringe visibility. The mechanical parts which are most sensitive to alignment errors are the beam combiner in the case of a smooth in-line reference and the proper conical mirror.

beam combiner :

So far, it has been assumed that the wave vectors $\vec{k}_O$ and $\vec{k}_R$ are perfectly collinear. In the case of a smooth in-line reference that means, the point of divergence of the reference beam P_R and the center of the exit pupil of the lens system P_P (see Figure 2.1a) have to be perfect conjugate points. This condition is difficult to satisfy by alignment of the beam combiner and, inevitably, additional spatial frequencies are introduced in the intensity pattern due to the altered interference phase $\Phi = \Phi_O - \Phi_R + (\vec{k}_O - \vec{k}_R)\vec{r}$ in equations (2.1) and (2.2). If the spatial frequencies from the additional term are equal or greater than the maximum spatial frequency resolvable by the camera the speckle information will be lost and correlation fringes are not obtainable.

Jones and Wykes [32] showed that especially transversal misalignments are critical, i.e. where the conjugate point P_R does not coincide with point P_P but is laterally displaced to it. Results demand alignment errors to be less than 0.1 mm for most interferometer set-ups. A more accurate calculation of the maximal allowable longitudinal departure from conjugacy was recently given by Peng and Joenathan [50]. The longitudinal alignment is less stringent since errors of some mm up to some cm can be tolerated.

conical mirror :

For convenience, the optical axis is assumed to equal the cylinder's rotational axis. Misalignment of the conical mirror is considered to be a superposition of its lateral displacement Δx and Δy from the optical axis as well as rotations around axes perpendicular to the optical axis. Figure 2.6 gives an illustration.

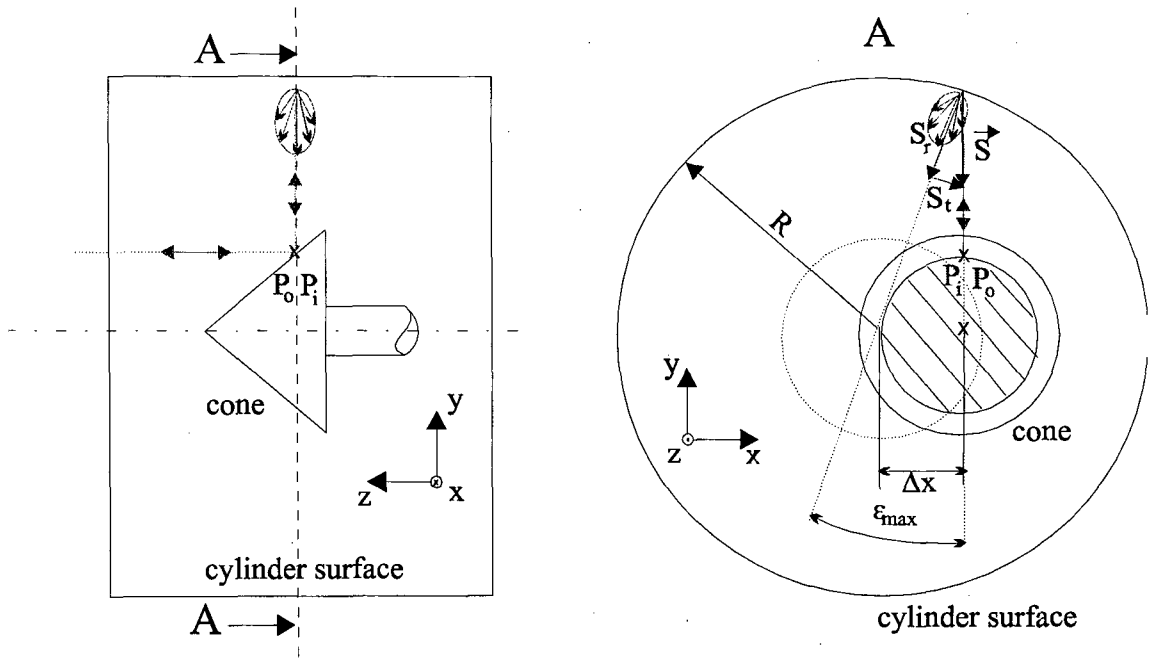

Figure 2.6a Misalignment error by lateral displacement Δx

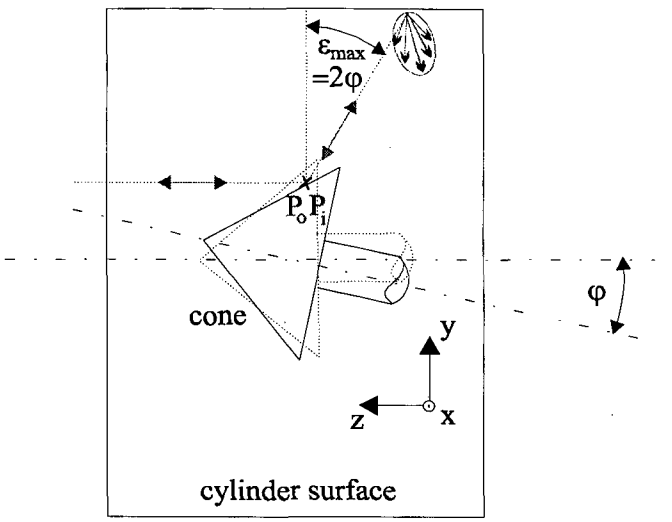

Figure 2.6b Misalignment error by rotation φ

Because of the diffuse reflection, the illumination point P_i and observation point P_o on the cone remain unaltered in the presence of lateral misalignment (Δx in Figure 2.6a). For sufficient large distances between camera and cylinder they can be considered to coincide on the cone. However, the intensity of light reflected back from the cylinder surface varies along the circumference according to the incidence angle ε of illumination toward the cylinder surface and its diffusive reflection characteristics. As a consequence the camera observes an inhomogeneous intensity pattern.

Since then optimal intensity ratio cannot be adjusted anymore for the entire surface under study, areas of low speckle modulation will remain which give rise to a decrease of visibility of correlation fringes. The lowest intensities are detected perpendicular to the direction of lateral misalignment (Δx) whereas, in direction to it, the intensities do not experience any alteration.

In addition, the sensitivity vector $\vec{S}$ deviates up to an angle ε_{max} from the ideal radial-only direction. Therefore, a small sensibility component in tangential (in-plane) direction is introduced. With S_r and S_t indicating the radial and tangential components respectively the new sensitivity can be described as

$$\vec{S} = S_r \cdot \vec{e}_r + S_t \cdot \vec{e}_t = \left(2\sqrt{1-\left(\frac{\Delta x}{R}\right)^2} \right) \vec{e}_r + 2\frac{\Delta x}{R} \cdot \vec{e}_t \quad \text{with}: \varepsilon_{max} = \arcsin\left(\frac{\Delta x}{R}\right) \qquad (2.18a).$$

Equation (2.18a) also states that the maximum angle of incidence ε_{max} depends on the radius R of the cylinder. The larger this radius the less the tangential component of sensitivity and, also, the less the intensity loss for constant alignment error Δx.

For example, an unpainted steel cylinder with an inner diameter of 20 mm was studied using an interferometer like illustrated in Figure 2.2. An upper limit of Δx = 0.2 mm was found experimentally, i.e. the fringe visibility was still acceptable for this alignment error.

Figure 2.6b illustrates that the same constraint developed above also applies for small mirror rotations. The maximum deviation angle of the sensitivity vector from ideal radial-only direction ε_{max} is, then, twice the rotation angle φ.

The ESPI system measures displacements by operating in the subtraction mode. Hence, unless lateral displacements and/or rotations of the cone are introduced during the loading process, they will not distort the correlation fringes that carry the information about the displacement field.

For small arguments ε_{max}, the error introduced to radial sensitivity is

$$\Delta S_r = \left|\vec{S}\right| - S_r = 2(1 - \cos\varepsilon_{max}) \approx \hat{\varepsilon}_{max}^2 \qquad (2.18b).$$

Equation 2.18b states that small alignment errors introduce only second order errors to the radial sensitivity. Therefore, they will not significantly alter the sensitivity vector.

They may, however, contribute to a significant loss of fringe visibility. The sensitivity of fringe visibility to these misalignments is, above all, a function of diffusive reflection characteristics of the cylinder surface under study. A white diffusive paint on such surface is expected to release the requirements for very careful alignment.

2.3 Extraction of phase data from electronic speckle-pattern-interference fringes

Like in any optical metrology system involving fringe displays, the objective of ESPI is the data reduction of these images into quantitative information. To obtain displacement data from the fringe patterns, it is necessary to extract the phase information δ intrinsically carried in the fringes. However, the fringe pattern of equation (2.4) is ambiguous as it contains no information about the displacement sense.

There are several methods for computer aided interference phase determination. For ESPI systems applied under laboratory conditions, temporal phase shifting/stepping is most frequently used. It follows a short description of this method and its principal error sources.

2.3.1 Temporal phase shifting and phase stepping

This method consists of phase stepping or shifting in one of the interferometer beams, mostly the reference. Many different techniques have been developed to perform accurate phase shifts. Most commonly used is the shifting of reflecting mirrors using a piezoelectric transducer (see Figure 2.1b). Less common is the use of rotating polarizers[28] and tilted glass plates.

In classical interferometers the phase difference varies smoothly over the detector array. However, in ESPI the phase varies randomly because of the random phase Φ of individual speckles. In literature basically two methods have been proposed to suppress this random speckle phase.

In the first method, no speckle correlation fringes are formed. Instead, several interferograms (speckle patterns) with mutual phase shift are recorded consecutively, before and after deformation [7]. The phase at each pixel is determined from the phase-stepped speckle patterns to yield two phase maps.
The phase change δ corresponding to the displacement can be calculated by subtraction of the two phase maps. This method will be referred to as difference of phase.

Several phase-stepped interferograms can be mathematically expressed as

$$I_i = I_m(1 + V\cos(\Phi + \alpha_i)) \qquad i = 1,\ldots,k \qquad k \geq 3 \tag{2.19}$$

where α_i are the discrete phase steps. If α_i is known, there remain three unknowns. Hence, at least three different interference patterns are necessary to solve this system of equations for the random phase Φ. If α_i is unknown but constant between pairs of consecutive recordings, the minimum number of interferograms increases to four. The same algorithm applied after deformation yields the interference phase $\Phi+\delta$ corresponding to the deformed state. The raw phase map due to phase change δ, calculated by subtraction, needs to be smoothed by means of adequate low-pass filter.

On the other hand, if the map of subtraction-correlation fringes as described in equation (2.4) is low-pass filtered it yields a similar form as equation (2.19). Note that mean intensity and fringe visibility are modified and Φ stands then for phase change δ. Hence, a second method uses suitable filters to remove the unwanted speckle noise from correlation-fringe maps. The phase change δ is calculated from several mutually phase-shifted and low-pass filtered fringe maps [47]. This method will be referred to as phase of difference.

To determine the interference-phase distribution, several different algorithms have been developed. The pointwise solution of the non-linear system of equations (2.19) for the interference phase becomes particularly simple, if the phase between consecutive interferograms is shifted by $2\pi/k$ in (k-1) equal steps, where k is an integer.

It is practical to restrict the value of k to 3, 4 or 5 as a compromise between accuracy of phase determination and computational effort. The perhaps most common algorithm for phase calculation is the four-frame method ($k = 4$ with $\alpha_i = 0, \pi/2, \pi, 3\pi/2$). The phase determined point by point becomes then

$$\Phi = \arctan\left\{\frac{I_4 - I_2}{I_1 - I_3}\right\} \quad ; \quad -\pi \le \Phi \le \pi \tag{2.20}$$

Instead of the discrete phase steps the reference phase can be shifted linearly during recording of the interferograms. One obtains the integrated intensities resulting in an expression that can be shown to be equivalent to equations (2.19), only the visibility term is modified by a constant factor [37]. Hence phase shifting is equivalent to phase stepping, both expressions used synonymously here.

2.3.2 Experimental requirements

The temporal phase-shifting method requires a sequence of constant phase shifts and, thus, atmospheric and mechanical stability of the experimental arrangement must be high. Algorithms where applied phase steps have to be known "a priori" demand calibration of the phase-shifting device. Therefore, they even increase the stability requirements. On the other hand, temporal phase shifting offers easy computation where the sign ambiguity is removed automatically which makes this method very fast.

2.3.3 Phase-measurement uncertainty

Most authors investigated systematic error sources of phase shifting like unknown sensitivity and non-linear response of the phase-shifting device [1, 31, 35]. A variety of so called error-compensating algorithms were proposed, usually increasing the necessary number of phase steps and the amount of data to be processed. Creath[8] gave a comprehensive overview of available algorithms.

Few authors considered the random errors by phase-shifting ESPI. In ESPI the random distribution of intensity causes some of the pixel elements to saturate and others to fail to give enough interference modulation above electronic noise level. Either in the correlation fringes (phase of difference) or the phase map (difference of phase), the introduced noise must be lowered until acceptable random errors of phase measurement are achieved. This is usually done by averaging and applying filter techniques.

Most investigators used Gaussian error propagation and described the rms-phase error by the variance. The error was estimated as a function of intensity ratios [56, 39], electronic noise[56, 39, 23], speckle size [39, 23] and speckle decorrelation [23, 10, 62].

The optimal intensity ratio and speckle size were found to be nearly the same as were derived in section 2.3.2 and 2.3.1 respectively. This emphasizes the close connection between optimal fringe contrast and lowest possible random error of phase measurement. Therefore, it is not astonishing that the random error increases, above all, with speckle decorrelation and thus with the loading (as can be expected from Figures 2.3, 2.4 and 2.5). However, in the absence of any other disturbance, the fast increasing error due to the loading lowers the acceptable out-of-plane rotation to about one tenth of the value corresponding to complete decorrelation [48].

The uncertainty derived theoretically from systematic and random errors demonstrate good agreement with the uncertainty found experimentally.

In general, the difference-of-phase method is considered more accurate than the phase-of-difference method, because smoothing of data by suitable filters is applied to one map of phase fringes rather than several correlation-fringe maps. Apart from this, false phase data from speckles (pixel elements) modulating above saturation level or below a certain minimum intensity (greater than noise level) can be marked invalid before other filter techniques are applied [7].

Typically, an uncertainty in the range of $2\pi/20...2\pi/30$ rad is quoted for the difference of phase[15, 46] compared with $2\pi/10...2\pi/15$ rad for the phase of difference [37, 47]. However, a new algorithm has been recently proposed [46] to overcome the disadvantages of the phase-of-difference approach by making low-pass filtering of correlation fringes unnecessary.

2.3.4 Conclusions:

The phase-of-difference approach uses secondary interferograms, i.e. calculates phase from correlation fringes, whereas the difference-of-phase method uses primary interferograms, i.e. speckle patterns.

For an algorithm of k-1 equal steps the phase-of-difference method requires k +1 recorded interferograms while the difference-of-phase method needs $2k$ interferograms. Hence, the lower uncertainties in phase measurement using the difference-of-phase method are achieved at the expense of increased time and memory for data acquisition.

	phase stepping/shifting	
	phase of difference	difference of phase
Number of recorded interferograms before deformation	typical: 3 or 4 rarely: ≥ 5	typical: 3 or 4 rarely: ≥ 5
Number of recorded interferograms after deformation	1	Same as before deformation
Sensitivity to external influences	moderate to high	moderate to high
Uncertainty $\Delta\delta$ [2π rad]	1/10...1/15	1/20...1/30

Figure 2.7 Comparison of methods for interference-phase determination by temporal phase shifting/stepping

2.4 Measurement error - a simplified model

The entire ESPI system still includes electronic modules for data processing. Nevertheless, it is reasonable to assume that the proper interferometer and phase-shifting device provide the main contributors to the uncertainty of measurement of radial displacement fields.

From equation (2.7) the radial displacement can be approximated to be

$$w_r = \frac{\lambda \cdot \delta}{S_r \cdot 2\pi} = \frac{\lambda}{S_r} \cdot FO \quad \text{with}: S_r = 2 \tag{2.21}$$

with FO denoting the fringe order. Since the variables are all considered statistically independent from each other, the radial displacement error Δw_r can be expressed as

$$\Delta w_r = \left[\left(\frac{\partial w_r}{\partial \lambda} \cdot \Delta\lambda \right)^2 + \left(\frac{\partial w_r}{\partial S_r} \cdot \Delta S_r \right)^2 + \left(\frac{\partial w_r}{\partial FO} \cdot \Delta FO \right)^2 \right]^{\frac{1}{2}} \tag{2.22}$$

Typical uncertainty of the He-Ne-laser wavelength is $\Delta\lambda = 0.03$ nm [15]. The sensitivity vector may show deviation from radial-only direction due to uncertainties of the angle of conical mirror (typical $< \pm 1^\circ$), small alignment errors of the cone as well as deviation from ideal collimated illumination. The maximal deviation angle was estimated to be $\varepsilon_{max} = \pm 2^\circ$, which yields a maximal sensitivity error of $\Delta S_r = 0.0012$.

On the basis of Figure 2.7 (section 2.4.3) the uncertainty of determination of fringe order was estimated to be $\Delta FO = \pm 0.05$. If a total number of ten fringe orders is considered, above uncertainty values inserted in equation (2.22) will yield a radial displacement error of

$$\Delta w_r = \left[22.5 \cdot 10^{-3} + 3.6 + 250 \right]^{\frac{1}{2}} \approx 16\,\text{nm} \tag{2.23}.$$

A comparison of the values in equation (2.23) clearly shows that the contribution of fringe-order uncertainty is dominant in the error-propagation equation. Hence, the error for radial displacement can be approximated by

$$\Delta w_r = \frac{\lambda}{2} \cdot \frac{\Delta\delta}{2\pi} = \frac{\lambda}{2} \cdot \Delta FO \tag{2.24}.$$

The approximation error committed when using equation (2.24) instead of equation (2.22) is less than 1%. Equation (2.24) states that the measurement error of radial displacement increases linearly with the phase-measurement uncertainty.

However, the phase-measurement uncertainty used in the error calculation requires relative good fringe visibility. Poor visibility of correlation fringes introduces more noise to the phase patterns, hence, increases further the radial displacement error.

2.5 Dynamic disturbances

So far, operation and error sources of the ESPI system have been studied for relative stable ambient conditions as typically found in the laboratory. It was shown that accurate displacement measurement requires, above all, accurate phase measurement.

Phase measurement takes time that is dominated by the loading process of the specimen (often takes several minutes). Therefore, other time dependent phenomena tend to be superposed to the phase data. Hence, outside the laboratory dynamic disturbances will introduce additional errors to the phase measurement. It is therefore necessary to know the quantities which will affect the interference phase in an unstable environment.

Equation (A3) yields the random phase of individual speckles found in ESPI

$$\Phi = \Phi_{OP_O} - \Phi_{OP_R} = 2\pi \cdot \left(\frac{GP_O}{\lambda_O} - \frac{GP_R}{\lambda_R} \right) \tag{2.25}.$$

The wavelength is defined as

$$\lambda = \lambda(v, f) = \frac{v}{f} \tag{2.26}$$

where v is the propagation velocity of light. Therefore, three disturbances which may affect the interference phase have to be analyzed. These are variation of propagation velocity v, variation of geometrical path length GP and variation of laser frequency f.

2.5.1 Variation of propagation velocity

The interference phase may change if the propagation velocities of object and reference beam are altered unequally. To describe such changes one uses the index of refraction n being the velocity ratio

$$n_{\text{medium}} = \frac{v_{\text{vacuum}}}{v_{\text{medium}}} = \frac{c}{v_{\text{medium}}} \tag{2.27}.$$

The index of refraction of vacuum is defined unity. In isotropic mediums and in the absence of frequency changes due to the Doppler effect, frequency f is a constant. Equation (2.26) and (2.27) allows

$$\lambda_{\text{medium}} = \frac{\lambda_{\text{vacuum}}}{n_{\text{medium}}} \tag{2.28}.$$

The laser light is supposed to propagate through air. The index of refraction of air changes linearly with the density ρ which itself is dependent on temperature T, humidity and air pressure to name just a few. Furthermore, if one describes the change of density of air only by temperature drift ΔT, the error for the index of refraction committed neglecting the other contributions is about 6 % (for temperature drift in ambient air of (20 ± 10) °C.

Therefore, the change of index of refraction of air can be approximated by [58]

$$\Delta n = \frac{n_{air(20°)} - 1}{\rho_{air(20°)}} \cdot \frac{\partial \rho}{\partial T} \cdot \Delta T \qquad (2.29).$$

As a result of equation (2.29), the index of refraction of air varies with about 10^{-6} per Kelvin. Since increasing temperatures causes the density of air to decrease, positive temperature drifts diminish its index of refraction. The same result one could obtain by using the empirical equations named after Edlen[60].

2.5.2 Variation of geometrical path length

The geometrical path length may vary with mechanical vibrations of parts of the interferometer, especially the reference and specimen surface. Their amplitude is directly proportional to the interference phase.

Temperature drift may also affect the geometrical path length as parts or the entire structure of the interferometer dilate. Dilation of geometrical path can be expressed as

$$\Delta GP = GP_{20°} \cdot \kappa \cdot \Delta T \qquad (2.30)$$

where κ is the dilation coefficient of the dilating material.

2.5.3 Variation of laser frequency

Whenever relative movements between laser source and detector occur, a shift of laser frequency due to the Doppler effect is generated. Such movements may be introduced by vibrations of reflecting parts of the interferometer including the proper specimen surface.

If, for example, a retroreflector vibrates in direction of the wave vector the maximum change of wavelength can be expressed as a function of vibration velocity [3]

$$\Delta\lambda = \frac{\frac{-2A_v}{c}}{1 + \frac{2A_v}{c}} \cdot \lambda \approx \frac{-2A_v}{c} \cdot \lambda \quad \text{for: } A_v << c \qquad (2.31)$$

where A_v is the velocity amplitude of the vibration and c is the propagation velocity of light in vacuum. It follows from equation (2.31) that velocities greater than 7100 m/s are required to cause a significant change of wavelength $\Delta\lambda > 0.03$ nm. Such high velocities are beyond the levels ever caused by vibrations to be expected here.

2.5.4 Principal error sources

There are, above all, two types of dynamic disturbances which influence the random phase of individual speckle (equation 2.25) and, hence, the phase measurement. These are temperature changes and mechanical vibrations.

a) Temperature changes:

Significant temperature fluctuations are most probably introduced by thermal air currents or air flow. They can be represented by a stochastic function $T(t,\vec{r})$ where the spatial location $\vec{r} = (x,y,z)^T$ describes the temperature field throughout the beam paths and variable t its change with time.

On the shop floor the temperature of air may vary from 10...40 °C. However, maximum amplitude of temperature fluctuation is only reached by very slow drifts since, usually, the stronger the noise the lower its frequency. On the other hand small temperature gradients of only a fraction of a Kelvin may change very rapidly as a result of thermal turbulence.

Due to relative large collimating of the object beam (>20 mm), local temperature gradients are not only present along that beam path but also in transversal direction to it. According to equation (2.29) and above arguments the refractive index of air becomes a function of space and time. Hence, to illustrate better the effect of temperature change upon phase measurement one can rewrite equation (2.25)

$$\Phi(t,x,y,z_0) = \Phi_{OP_O}(t,x,y,z_0) - \Phi_{OP_R}(t,x,y,z_0) = \frac{2\pi}{\lambda}\cdot\left(OP_O(t,x,y,z_0) - OP_R(t,x,y,z_0)\right)$$

$$\text{with:} \quad OP_O(t,x,y,z_0) = \int_0^{GP_O} n(t,\vec{r})\,ds \quad , \quad OP_R(t,x,y,z_0) = \int_0^{GP_R} n(t,\vec{r})\,ds \qquad (2.32)$$

$$\text{and:} \quad \vec{r} = \left(x(s),y(s),z(s)\right)^T$$

where $z = z_0$ defines the image plane (CCD sensor), s expresses the geometric path along the beam and ds denotes its differential. Equations (2.32) demonstrates the influence of two temperature dependent quantities, geometrical path GP_O, GP_R and index of refraction $n(t,\vec{r})$, upon the optical path and consequently, upon interference phase Φ.

Phase errors may only occur where temperature changes affect unequal beam paths. The amplitude of phase error will be proportional to the temperature change and the path length affected by it.
For example, a bubble of air with an extension of 50 mm which differs only by 0.65 K from the mean room temperature (20 °C) introduces an error as large as one tenth of a fringe order when drifting through one of the interfering beams. Many such events could be integrated along long unequal paths, increasing the resultant phase error. Therefore, unequal-path interferometers (see Figures 2.1 and 2.2) with long object-to-camera distances are particularly sensitive to temperature noise.

For temperature changes affecting the geometrical paths of object and reference beam equally, the phase error due to temperature dependency of refractive index cancels out. However, low frequencies with large amplitudes like the drift of mean room temperature may cause phase errors due to dilation of parts of the interferometer during the loading process or altered characteristics of the phase-shifting device.

If temporal phase-shifting is applied, the time dependency of phase Φ illustrates that strong temperature noise may cause the loss of fringes in the phase map. Few and fast frame grabbing, like in fringe tracking or modified phase-shifting, may "freeze" the temperature turbulence at each deformation state.

Phase data calculated from these speckle patterns may visualize the information carrier together with phase turbulence due to the stochastic process of thermal air currents, but the information carrier can not be retrieved securely from this superposition.

b) Mechanical vibrations:

A common method to describe complex mechanical vibrations is to decompose it into individual vibrations, each with its own amplitude, frequency and phase.

The components of such complex vibration found in an industrial environment commonly range from low frequency motion (object drift and building vibrations) up to medium frequency (from nearby vibration sources). Their maximum level can be derived from several standards about vibrations allowed at work [24, 25, 26]. From these standards one can conclude that the possible level of vibrations does not exceed

- 100 µm of displacement (f_v = 1...1.6 Hz)
- 1 mm/s of velocity (f_v = 1.6...160 Hz)
- 1 m/s^2 of acceleration (f_v = 160...500 Hz.)

Therefore, the ESPI system may only be exposed to these maximum values allowed in the machinery shop. In an environment where light manufacturing is performed, vibrations with displacement amplitudes A_V in the micrometer range have frequencies f_v < 100 Hz [44].

Equations (2.14) and (2.15) illustrate why the large amplitudes of low frequency vibrations described by the above limits usually cause already speckle decorrelation and, thus, the complete loss of fringes. It is important to note that in-plane motions, i.e. motions the interferometer is supposed to be not sensitive to, might lead to complete decorrelation as well. For radial displacement measurements, where vibration between the specimen cylinder and the conical mirror causes in-plane and out-of plane motion as a function of polar angle, the in-plane component of vibration is the limiting factor since it usually causes faster decorrelation. The only countermeasure against such large amplitudes is still reasonable mechanical isolation.

The higher frequencies with typical lower amplitudes do not cause speckle decorrelation. However, vibrations with out-of-plane component affect the geometrical path length and, hence, cause considerable vibrations of the phase. For example, the above mentioned limit at 500 Hz still introduces an amplitude as large as 1/3 of a fringe. Assuming small enough shutter times to "freeze" such rapid motions into the image, one usually ends up taking snap shots at different vibration states since frame acquisition rate is limited to about 30 frames/s and the exact vibration spectrum is unpredictable. As a consequence, the effective phase steps for temporal phase stepping techniques become unpredictable, causing large errors in the algorithm and, very often, the complete loss of deformation fringes.

Therefore, the major drawback of phase measurement by a temporal phase-stepping technique is the increase of necessary acquisition time which makes it susceptible to vibration noise. Beside proper mechanical isolation to avoid speckle decorrelation, two different ways were proposed so far in order to deal with vibrations in phase stepping.

One solution is based on statistical arguments that small phase vibrations are "averaged out" by taking several images per phase step and/or increasing the number of phase steps. Recently, de Groot [9] showed for vibration amplitudes smaller than 0.5 rad (<1/13 of a fringe) that any arbitrary vibration can be built up from individual tones, each of which makes, in a linear approximation, a contribution to the total phase-measurement error. Making use of the linear approximation, he describes the sensitivity of common phase-shifting algorithms by a phase-error-transfer function in the vibrational frequency domain.

Beside the possibility to study the sensitivity of various algorithms to particular vibrational frequencies, this phase-error-transfer function represents a practical tool to predict the effects of continuous complex vibration spectra. If the vibrational frequency spectrum is well defined, experimental results confirm the statistical arguments and show that temporal phase shifting might be performed without complete mechanical isolation.

The other solution is searched in decreasing necessary acquisition time for each deformation state which is dominated by successive readouts of the pixel array. To defeat this readout time, several modifications of the standard temporal phase-shifting technique have been proposed. They include spatial instead of temporal phase shifting [59] as well as new algorithms operating with less phase steps [34, 63] combined with fast phase-shifting devices [63, 6].

All these modifications exploit the fact that mechanical vibration can be considered as rigid body motion which causes the phase to vibrate uniquely over the pixel elements of the camera. Now, the necessary information at each deformation state is captured so fast that fringes due to mechanical vibrations are essentially "frozen" into the phase map. Because rigid body motions cause unique fringe patterns, they can be recognized and compensated [16] by software, as long as their amplitude is small enough.

The method of fast acquisition is particularly suited in the presence of low frequency vibrations (<10 Hz) with relative large amplitudes (>1/4 of a fringe) where "averaging methods" already fail. However, if expected amplitudes are much less and the frequency spectrum of vibration is well defined, the "averaging method" demonstrates that one can do much to improve the performance of temporal phase shifting in the presence of vibration without necessarily changing the hardware.

2.6 Conclusions

From the arguments given in the previous section some conclusions may be drawn for the construction of robust interferometers:

(1) Temperature noise may only cause phase measurement errors where light beams travel at separate paths. It is due to the spatial random nature of temperature turbulence why interferometer set-ups with separate beam paths are prone to large errors, no matter how fast frame acquisition is at each deformation state. Therefore, an equal or quasi-equal-path design should be favored in a robust interferometer. These designs are the only set-ups that are insensitive to strong temperature turbulence.

(2) A robust interferometer should be based on a proper isolation against large mechanical vibrations that avoids speckle decorrelation and decreases vibration amplitudes to acceptable values. It is reasonable to assume that these are amplitudes in the submicrometer range causing the phase to vibrate less than 3 fringe orders (6π rad).

(3) It is believed that proper mechanical isolation could be achieved by stiff attachment of the specimen cylinder to the interferometer (or vice versa). The entire structure might need to be mounted on a platform damped against vibrations up to 500 Hz.

(4) Very fast frame acquisition at each deformation state can freeze the remaining phase vibration into the phase map. In order to delete this unwanted portion from the phase map, the same algorithms developed for compensation of rigid body motions may be applied. It is believed that a reasonable phase uncertainty for the measurement system equal to or better than 1/10 of a fringe (1/10 of 2π rad) is feasible.

3 State of art for design of robust interferometers

3.1 Compensation of temperature noise

The simplest countermeasure against temperature noise is a proper isolation of the two beam paths. By attaching the specimen to the interferometer head, a shielding material can reduce substantially the sensitivity of the interferometer to temperature turbulence of air.

Another solution is to choose modified interferometers that are naturally insensitive to temperature noise. One of the principal conclusions drawn from the previous section was that such insensitivity can be achieved if the interfering beams travel substantially the same path. So far, the following modifications of ESPI were developed to achieve this merit.

3.1.1 Electronic Shearography

Electronic Shearography was introduced by Hung [22]. Like ESPI it is a computerized process. A typical set-up is shown in Figure 3.1. If one is only interested in the out-of-plane component, the illumination and observation are normal to the specimen surface.

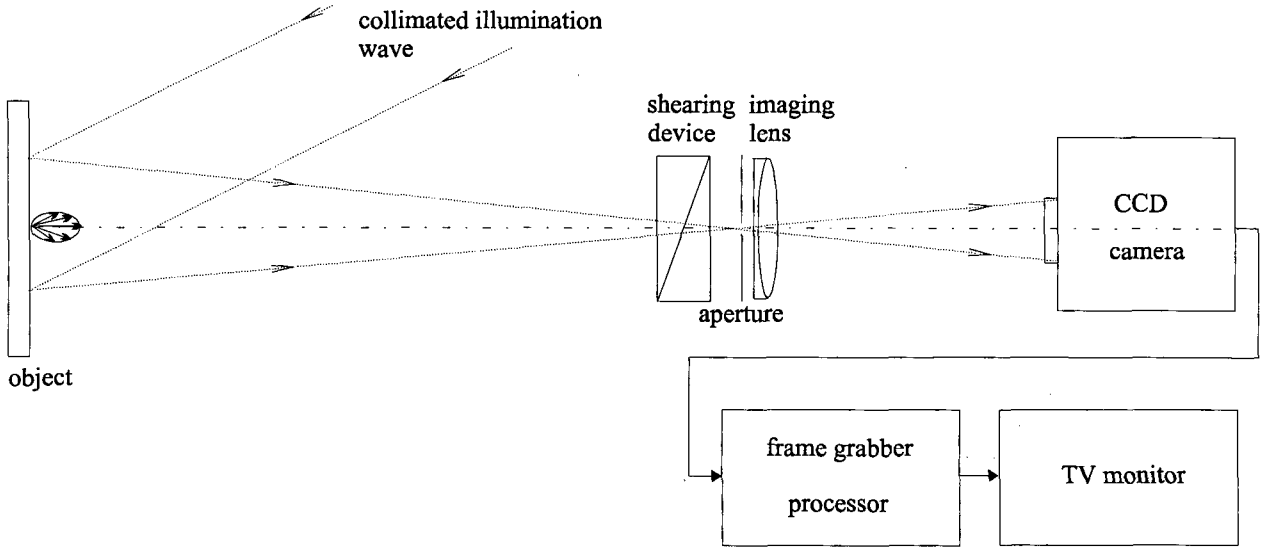

Figure 3.1 Interferometer set-up for Electronic Shearography (Hung)

One difference in Electronic Shearography is that the object is imaged by a CCD camera through a shearing device. The shearing device brings the rays scattered from one point on the specimen surface to interference with those scattered from a neighboring point. In other words, two lateral sheared images are viewed by the camera which gave this technique the name.

Since the shearing is very small, the optical paths of the interfering beams are essentially the same. As a consequence of the lateral shear, Electronic Shearography measures displacement derivatives instead of displacements. Assuming a lateral shearing only in x-direction (Δx) and zero in-plane component of the deformation vector the phase change δ for the arrangement sketched in Figure 3.1 is governed by the equation

$$\delta = \frac{4\pi}{\lambda} \cdot \frac{dw}{dx} \cdot \Delta x \qquad (3.1).$$

Electronic Shearography is advantageous for measurement of strain which is proportional to displacement derivatives. To yield information about surface displacements instead, a numerical integration of measured displacement derivatives has to be performed. This certainly introduces an additional error source.

A comprehensive treatment of the subject of major limitations of Electronic Shearography was given by Owner-Petersen [49]. They are principally lower sensitivity and faster decorrelation due to the loading process which, together, lead to poorer fringe visibility and higher uncertainties for phase measurement.

3.1.2 Quasi-equal-path ESPI

The quasi-equal-path systems developed so far for ESPI can be classified in two groups. That are:

- quasi-equal-path ESPI using a speckled reference beam
- quasi-equal-path ESPI using a smooth reference beam

a) Speckled reference:

Modified ESPI systems using a speckled reference beam have been investigated first by Joenathan [29] and later by Wu [64]. Their interferometer arrangements are illustrated in Figures 3.2 and 3.3 respectively.

They have in common that a small mirror mounted on a piezoelectric transducer is placed beside the object to direct part of the illuminating beam to a ground glass located in front of the camera lens. The ground glass serves as a diffuser, thus converting the smooth reference into a speckled one before reaching the CCD. This arrangement was found to be especially insensitive to the angle of the beam that illuminates the ground glass and, therefore, only very little alignment is required.
The optical path lengths of reference and object beam are matched naturally as they travel the same path.

Joenathan placed the ground glass such that it covers approximately half of the aperture (see Figure 3.2). Because a speckled reference beam is used, optimal fringe contrast is achieved when the intensity ratio r between reference and object beam is near unity (see section 2.3.2). Therefore, small alignments of the ground glass are required to equilibrate their intensities.

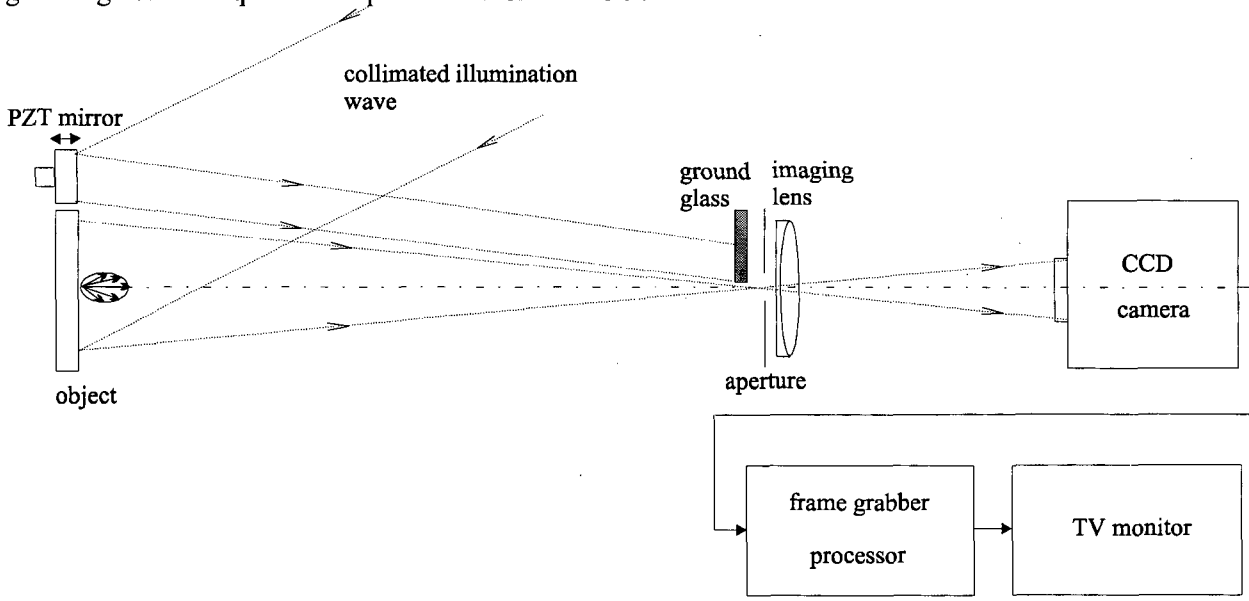

Figure 3.2 Modified ESPI system after Joenathan using speckled reference

Wu further simplified the system by illuminating the object with a diverging beam from a laser diode and placing a tiny diffuser on the optical axis (see Figure 3.3). He proposed that the intensity ratio is adjusted by the camera aperture. However, this will alter the speckle size too and, often, lead to poorer fringe visibility.

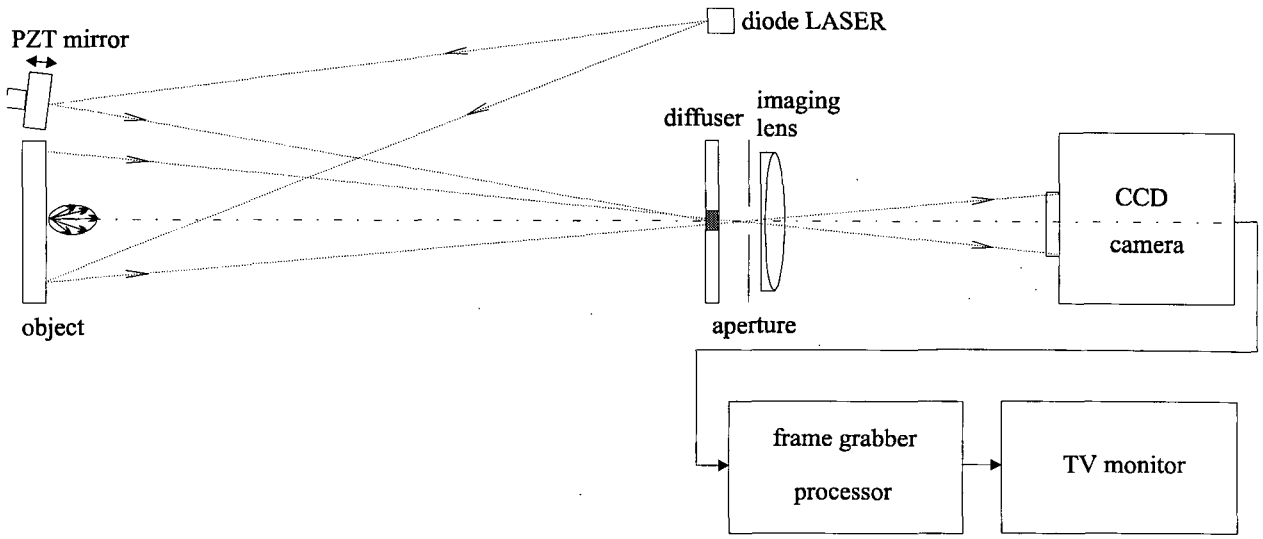

Figure 3.3 Modified ESPI system after Wu using speckled reference

Both arrangements are easy to align and make optimal use of laser power since beam splitters are not required. On the other hand, the optical paths of object and reference beam are only partially the same. As expected by conclusions drawn in section 2.6.4, these interferometers do not properly compensate strong phase turbulence due to local temperature gradients within radial direction of the respective beams. Own experimental experiences indicate that, for a given object-to-camera distance, the larger the object under study the smaller the compensating behavior of the interferometer with respect to phase turbulence.

b) Smooth reference:

Two ESPI-interferometers using a quasi-equal-path arrangement together with a smooth reference beam were developed by Peng and Joenathan [50, 30].

In the first arrangement sketched in Figure 3.4 the object is illuminated by a collimated laser beam [50]. An optical wedge or glass plate placed in front of the object reflects a fraction of about 4% of the incident light which serves as a reference. The major portion of light illuminates the object surface. Because the distance between wedge and object is kept very small, the optical paths traveled by the reference and object beam are essentially the same.

Using a smooth reference, strict alignment is required (see section 2.3.6). However, the lateral alignment of the reference beam is already ensured by the common-path arrangement. The axial alignment can be best achieved if the object is viewed through an object plane telecentric lens, i.e. a lens where the exit pupil is at the back-focal point. The speckle size is controlled by the size of the exit pupil.

To control the intensity ratio, Peng and Joenathan proposed a technique that uses the polarization property of diffusive reflection and is highly efficient in laser-power usage. The object surface painted white amplifies the depolarization effect of light scattered back from a diffuse surface. The reference beam reflected by the glass plate, keeps the original linear polarization of laser illumination due to the

smooth dielectric surface. Using these properties, the intensity of the reference beam can be conveniently adjusted by rotating a polarizer in front of the camera lens while the intensity of the object beam remains almost unchanged. The polarizer also ensures equal polarization of reference and object beam which enhances the modulation of interference pattern and, consequently, the visibility of fringes (see section 2.3.5). Phase measurements are obtained applying the phase-stepping method which is accomplished by translating the glass plate mounted on a piezoelectric transducer.

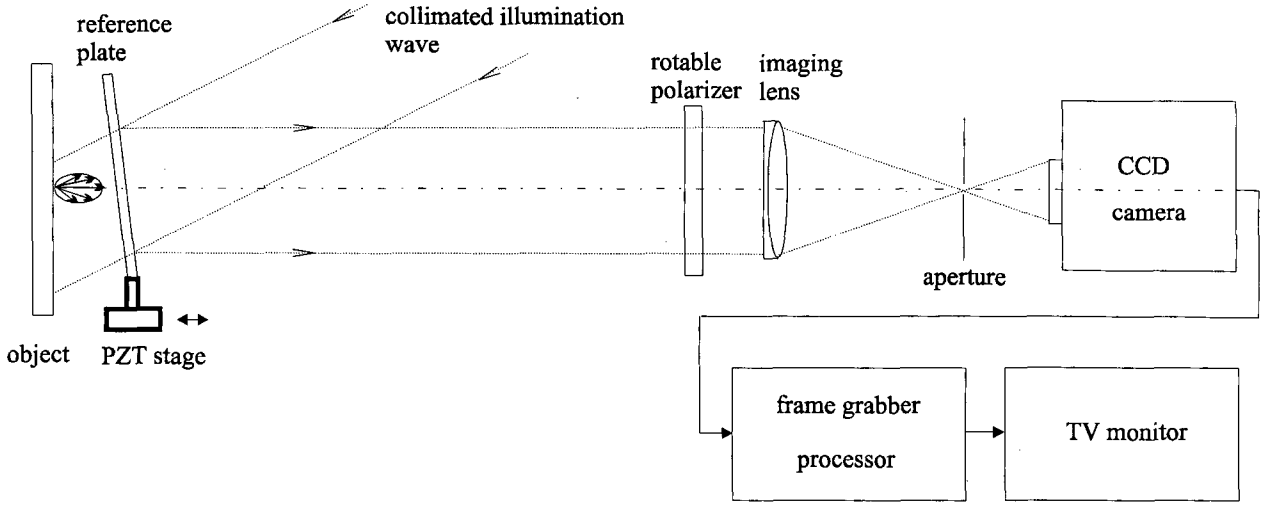

Figure 3.4 Quasi-equal-path interferometer after Peng andJoenathan using reference-glass plate

The object size that can be studied is mainly limited by the size of the reference-glass plate and the clear aperture of the imaging lens. To overcome these limitations, Joenathan proposed a second, modified system where the reference glass plate is substituted by a plano-concave lens so that a converging rather than a collimated reference beam is obtained (see Figure 3.5) [30]. Now, the reference beam can be focused onto the aperture of a normal camera lens, hence, eliminating the restrictions on the imaging system of the previous interferometer.

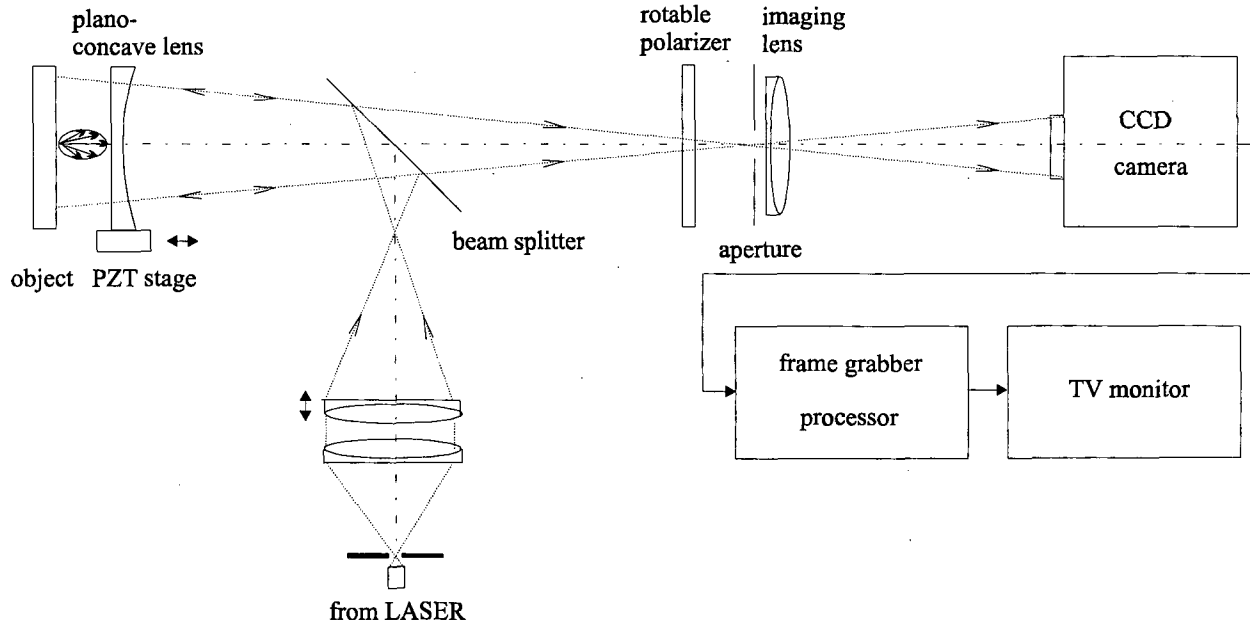

Figure 3.5 Quasi-equal-path interferometer after Joenathan using plano-concave lens

3.1.3 Comparison of methods

In figure 3.6 is shown a comparison of methods with respect to important parameters.

		Shielding	Shearo-graphy	Quasi-equal path Interferometer	
				Speckled Reference	Smooth Reference
Complexity of experimental arrangement		Low	High	Low	Medium
Computational effort		No	Medium	No	No
Noise Suppression	Temperature noise	Yes	Yes	Partial	Yes
	Mechanical vibration	No	Yes	Partial	Partial
Requirements for quality of optics		No	High	Low	Medium
Requirements for mechanical alignment		No	High	Low	Medium
Sensitivity to radial displacements		N.A.	Low	High	High
Price		Low	High	Low	Medium

Figure 3.6 Performance of methods against temperature fluctuations in radial displacement measurements

It can be seen that shielding is a very simple and cheap method, compared to the others. Although it is very powerful against phase errors due to temperature turbulence in the beam paths, it does not prevent parts of the interferometer to dilate due to thermal drifts.

The solution which comes closest to a common-path arrangement, thus which might be expected most robust to any kind of temperature noise, is Electronic Shearography. Then, an angular shearing device would be necessary to measure radial displacement derivatives in internal cylinder surfaces. That means the original image must be superposed to a slightly rotated one.

An angular shearing device has already been reported [42] that requires non-standard optical elements, thus, increasing dramatically the complexity of the experimental arrangement. Apart from that, the lowered sensitivity and fringe quality together with the need for numerical integration of measured data to finally yield the information wanted, makes this technique inadequate for radial displacement measurement.

A promising solution, that preserves the sensitivity of displacement sensitive interferometers combined with effective compensation of temperature noise, is the quasi-equal-path arrangement using a smooth reference beam.

3.2 Vibration isolation

The ESPI optical head can be built light-weight and compact using stable optical mountings. Then, the most probable origin of phase errors due to mechanical vibration of parts of the interferometer is the necessary distance between the optical head and the specimen surface. One solution to eliminate such mechanical vibrations is proper isolation of the measurement system. That means to mount the interferometer together with the specimen and its loading device on air cushions. This is often very costly because of the weight and/or the size of the entire system to be raised. However, it represents the only countermeasure against large mechanical vibration that causes already speckle decorrelation. Smaller mechanical vibrations can be isolated by using several possible modification of the ESPI system. So far, the following modifications have been proposed:

3.2.1 Active phase stabilization

Whenever the phase vibrates homogeneously over the entire detector area (e.g. due to small rigid body motions between ESPI head and specimen), active phase stabilization can be applied for compensation. That means, small phase shifts introduced by a phase actuator in either the object beam or the reference beam may compensate phase perturbations caused by mechanical vibrations. Active phase stabilization is achieved by a closed-loop system including a phase sensor, a controller and a phase actuator.

Beside the ESPI interferometer, often, a secondary interferometer serves as the phase sensor using part of the interfering beams coupled out for this purpose [21] or another source, typically a laser diode [11]. The beam paths of the ESPI interferometer and the secondary interferometer are essentially the same. Therefore, the intensity of part of its fringe pattern can serve as a measure for the actual phase in the ESPI interferometer. This intensity is detected by a photo diode, a CCD line or another cheap but fast photo detector whose read-out frequency is well above maximum frequency of the vibration (>1 kHz).

The controller processes the intensity signal captured by the photo detector in such a way that it will compensate the phase vibration of speckles by driving the phase actuator. Usually a PID (proportional, integral, differential) controller is applied. Because the maximum frequency of vibration that causes trouble is relative low (<500 Hz), digital control with A/D, D/A converters and proper software can be accomplished on the host computer of the Holographic Station [21].

The phase actuator is usually a light weight mirror mounted on a piezoelectric actuator [21] or an optical fiber wrapped around a piezoelectric actuator [4]. In both solutions the optical path of laser light is altered by variation of its geometrical path length.

It should be emphasized here that none of the found active phase-stabilization systems, really operating under rough conditions, made it superfluous to provide a reasonable passive vibration isolation that avoids the decorrelation of speckles.

3.2.2 Reduction of necessary acquisition time

Another approach to avoid that vibrations destroy the phase data at each deformation state is the reduction of necessary acquisition time to values much shorter than the vibration period. Although many solutions proposed so far come mainly from developments to study fast transient deformations, they also represent solutions for static deformation measurements in adverse conditions.

ESPI interferometers which extract the phase from a single exposure or two time-critical exposures with an integration time down to some milliseconds have already been reported [59, 63].

a) Fringe tracking

An ESPI-interferometer that uses fringe tracking for phase extraction from a single exposure per deformation state does not need any hardware alteration. The method originates from manual fringe counting. It is based on algorithms which search for local brightness maximum and minimum of the fringe pattern [20]. The thinning process results in a fringe skeleton with its fringe extremes corresponding to phase values δ that are integer multiples of 2π. Therefore interpolation has to be applied between loci of fringe extremes and hence, accuracy of fringe tracking is relatively low. Fully automation of this technique is not possible because the sign ambiguity cannot be removed without side information.

Phase measurement techniques that extract the phase without sign ambiguity from a single exposure or two time-critical exposures can be classified in temporal and spatial methods. However, almost all require nonstandard instrumentation and more complicated equipment.

b) Temporal Method:

The solution proposed by Wizinowich to study static deformations in rough conditions applies heterodyning and temporal phase stepping [63]. He developed the 2 + 1 phase-stepping algorithm, where the recorded phase-stepped interferograms are

$$\begin{aligned} I_1 &= I_m(1+V\cos\Phi) \\ I_2 &= I_m(1+V\cos(\Phi-\pi/2)) \\ I_3 &= I_m(1+V\cos(\Phi-\pi)) \end{aligned} \tag{3.2}$$

and the random phase Φ is recovered for each deformation state by the formula

$$\Phi = \arctan\left[\frac{2I_2-(I_1+I_3)}{2I_1-(I_1+I_3)}\right] \quad \text{modulo } 2\pi \tag{3.3}.$$

His basic intention was to require merely two time-critical interferograms, i.e. I_1 and I_2 in equation (3.3). Hence when these two interferograms are recorded on either side of the instant of interline transfer on a standard CCD, exposures of less than 1 ms can be taken as fast as 1 μs apart. This should freeze practically all vibrations into the phase map at each deformation state. The mean intensity, i.e. $I_1 + I_3$ in equation (3.3), can be acquired at any time.

To exploit the advantage of the fast interline transfer (typically less than 1 μs) the phase-shifting device must complete a 90° phase shift in about the same time. The standard arrangement using a moving mirror mounted on a piezoelectric transducer is too slow due to inertia introduced by the mass of the mirror.

Instead, a frequency shift in laser light may produce this phase shift if there is a difference in optical path length between the object and reference legs. More recently, Colucci and Wizinowich used heterodyning by means of an acusto-optic modulator to achieve necessary phase shifts within less than 1 μs [6]. This way the critical acquisition time is reduced to twice the integration time required to achieve a good signal-to-noise ratio for one speckle interferogram. This minimum integration was reached at about 1 ms. A timing sequence for the three speckle interferograms is illustrated in Figure 3.7.

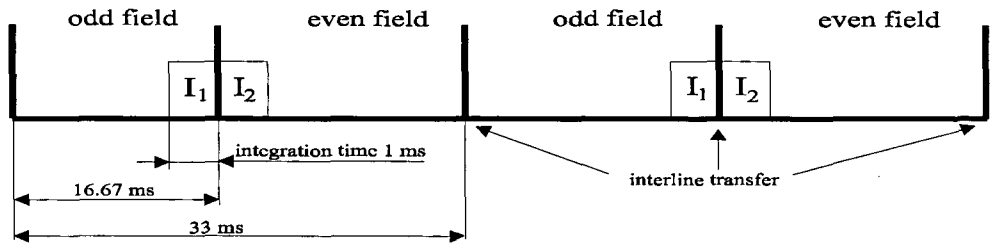

(a) recordance of time-critical interferograms

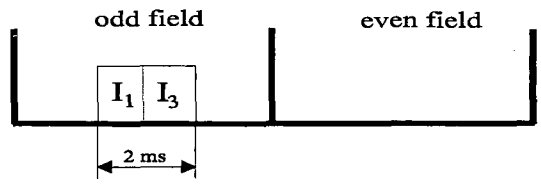

(b) recordance of mean intensity

Figure 3.7 Time sequence for recording of speckle interferograms after Wizinowich

c) Spatial Methods:

Contrary to temporal methods, where the phase information is separated into a sequence of interferograms, in spatial methods the phase information is spatially separated and captured during a single exposure. The spatial methods can be further classified in spatial carrier and phase-stepping techniques.

The spatial carrier phase measurement techniques need no special device for the generation of the carrier phase. It can be achieved by a tilt between reference and object wave, usually introduced by simply tilting a mirror in the reference leg. On the other hand, these techniques require much more sophisticated processing[33] and the range of deformation measurement is reduced with respect to phase-stepping. The intensity patterns before and after deformation are given by

$$\begin{aligned} I_{\text{before}} &= I_{\text{m}}(1 + V\cos(\Phi + 2\pi f_x \text{x})) \\ I_{\text{after}} &= I_{\text{m}}(1 + V\cos(\Phi + \delta + 2\pi f_x \text{x})) \end{aligned} \tag{3.4}$$

with f_x denoting the carrier frequency in x direction. In order to extract the phase due to deformation without ambiguity, certain conditions have to be fulfilled. The maximum gradient of δ should be less than the spatial carrier phase gradient. Mean intensity and visibility should vary slowly compared to the carrier frequency, which itself, should be less than half the sampling frequency in order to obey the Nyquist condition. The processing can be done in the space domain or in the frequency domain which are equivalent but show some particularities. For instance, better accuracy is obtainable with the frequency domain processing but fully automation is more difficult than for space domain processing.

An alternative method, that preserves the measurement range, is spatial phase-stepping. It represents an adaptation of temporal phase-stepping. In order to measure phase instantaneously, phase steps are introduced in, at least, three parallel channels. Therefore, a more complicated experimental arrangement is required. The techniques, that have been proposed so far to generate and record phase-stepped ESPI-interferograms simultaneously, utilize either polarization control or diffraction elements.

For example, Haasteren *et al.*[59] use spatial phase-stepping by polarization control [38] to study transient problems. The optical configuration of their ESPI-interferometer is sketched in Figure 3.8. It is based on the 2+1 phase-stepping algorithm [63] mentioned above. Due to its importance for the concept of this work, their interferometer is described in more detail.

The collimated light of an Ar-ion laser (λ = 514 nm) propagates through a beam splitter with intensity ratio 4-96 %. The major portion of intensity illuminates the object surface while the minor portion is used as a smooth reference. The object is imaged by an imaging lens onto three CCD's simultaneously. An adjustable diaphragm in the front-focal point of the imaging lens controls the speckle size on the CCD arrays.

Object and reference beam are combined by a Glan-Thompson-type polarizing beam-splitter prism that is used backward [2]. Like illustrated in Figure 3.8, only light scattered back from the object that is polarized along the x-axis is transmitted, whereas only light from the reference beam that is polarized along the y-axis is reflected.

The combined beams containing two linear and orthogonal polarizations are then decomposed by a beam splitter into two portions of equal amplitude. The reflected portion propagates through a quarter-wave plate that has its fast axis in 45° to the x-axis and, subsequently, passes through an analyzer with its transmission direction aligned to the fast axis of the quarter-wave plate. The resultant beam represents the 90° phase-shifted interferogram and is recorded by camera 2.

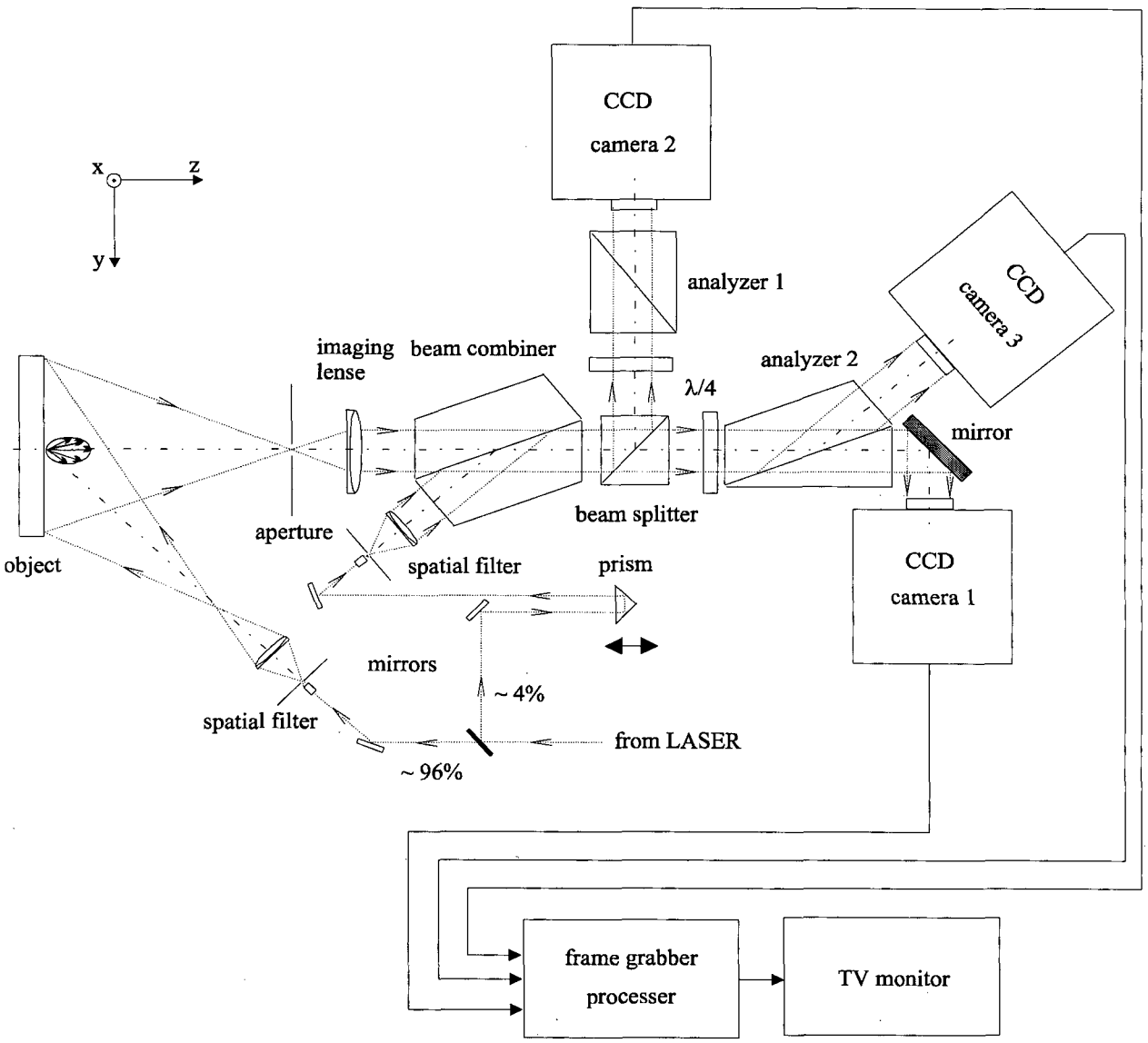

Figure 3.8 ESPI system after Haasteren *et al* using spatial phase stepping by polarization control

The transmitted portion propagates through a quarter-wave plate that has its fast axis in 45° to the x-axis as well. Behind it, another beam division is obtained by a Glan-Thompson-type polarizing beam-splitter prism. Hence the transmitted beam (like sketched in Figure 3.8) polarized along the x-axis represents the unshifted interferogram and is recorded by camera 1 while the reflected beam polarized along the y-axis represents the 180° phase-shifted interferogram which is recorded by camera 3.

Due to the need of high transmittance as well as high extinction ratio to unwanted polarizations, expensive Glan-Thompson-type prism polarizers were applied as analyzer and beam combiner elements.

The cameras had to be aligned such that the three speckle patterns, captured simultaneously by the respective CCD sensors, are sufficiently correlated. Haasteren *et al* concluded that the error of lateral alignment (x,y-position in Figure 3.8) should not exceed 1/10 of the speckle size which is resolved by one pixel, i.e. about 1 μm, while longitudinal alignment errors of 20 μm are still tolerable. Each camera is connected to its frame grabber forming three parallel channels. Since their performance is not absolutely identical, mean intensity I_m and modulation $V \cdot I_m$ need to be tuned.

The random phase Φ can be recovered applying equation (3.3), with I_i (i=1,2,3) indicating the intensities of the interferogram captured by the i-th camera. The phase at each pixel is calculated by a pipeline-image-processing system. Unless image improvement by filter techniques is performed, the processing system achieves phase measurement at video rates, i.e. 25...30 phase maps per second.

Alternatively, simultaneous phase steps can be introduced by gratings [38]. As a Diffraction Optical Element (DOE), it serves two important roles:

1) splitting the diffraction orders either toward different detectors or toward different regions on the same detector
2) introduction of additional phase steps into each of the diffracted beams by
   - movement of one diffraction grating between deformation states
   - adjustment of the relative position of two gratings for the object beam and reference beam, respectively
   - use of modified phase gratings

Figure 3.9 shows the experimental arrangement that was successfully applied by Rodriguez-Vera *et al.*[52] to study transient or static deformations with ESPI. A computer generated modified crossed phase grating was applied that needs no transversal movement during the loading process in order to introduce the necessary phase steps between the four first order diffracted fields. Unlike in a multi-camera design of a polarization controlled interferometer, the diffracted beams are imaged by a single detector. However, the possibility to calculate the interference phase from a single TV-frame is clearly bought at the expense of spatial resolution of the resultant phase map.

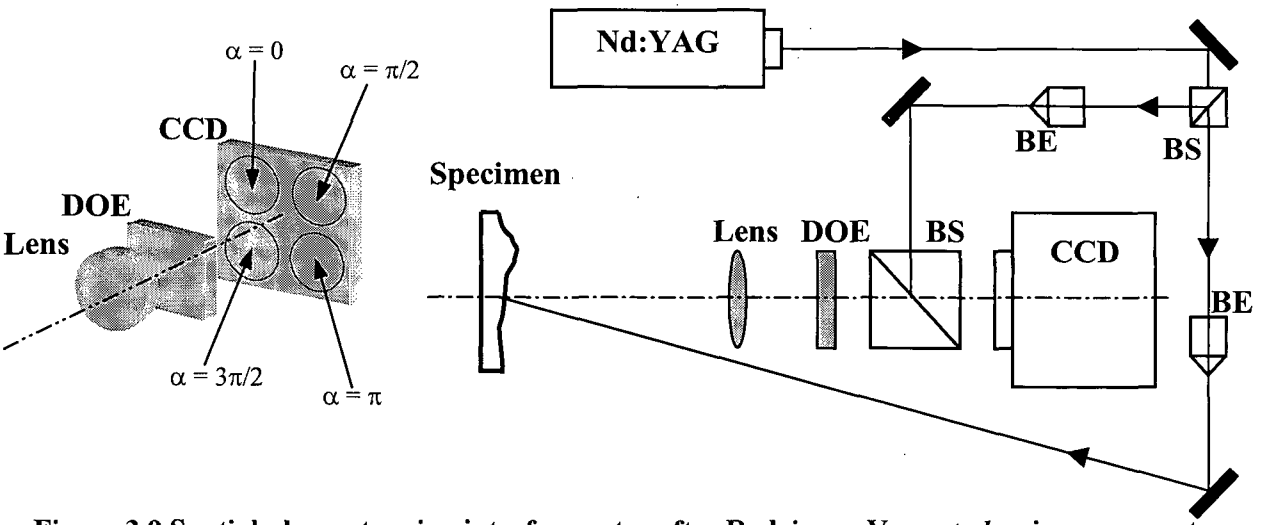

Figure 3.9 Spatial phase-stepping interferometer after Rodriguez-Vera *et al.* using a computer generated modified crossed phase grating (BS: beam splitter, BE: beam expander)

Another technique combines the spatial carrier phase method with phase-stepping. The spatial carrier phase is introduced by a large tilt between reference beam and object beam in order to obtain a constant phase shift between successive pixels. Assuming a constant phase step of 90° between pixels, the grabbed interferogram before deformation can be described by

$$I_i(x,y) = I_m(x,y)\left\{1 + V(x,y)\cos\left[\Phi(x,y) + 2\pi f_x x + \frac{\pi}{2}i\right]\right\} \tag{3.5}$$

where f_x is the carrier frequency. Instead of grabbing at least three phase-stepped interferograms, three or more sequential pixels are used to calculate the phase at x,y – position applying standard phase stepping algorithms. The resultant phase map contains the desired phase plus a phase ramp of 90° per pixel.

However, this additional phase ramp cancels out automatically if the same procedure is repeated for the deformed state and the phase due to deformation is calculated by subtraction.

The technique is applicable whenever $\Phi(x,y)$ varies slowly over the amount of neighboring pixels needed for its calculation. This is clearly not true in ESPI, where the phase of speckle varies randomly over the detector and its intensity is usually resolved by a single pixel. Therefore, spatial carrier phase-stepping is feasible with ESPI, only if the size of speckles is increased by defocusing the image or choosing higher f-numbers of the imaging optics and, hence, a speckle becomes resolved by a large number of pixels. Apart from that, mean intensity and visibility should vary only very slowly. Thus, the relative simple experimental arrangement is gained at the cost of spatial resolution, dynamic range and uncertainty.

3.2.3 Comparison of methods

The above described methods for vibration isolation are compared with respect to several criteria. The results are shown in Figure 3.10. The most important criteria chosen are:

a) Vibration compensation

Beside raising the entire measurement system on an optical table to effectively isolate ground vibration, none of the reported tools for vibration compensation operates satisfactorily alone. Stiff enough attachment between the optical head and the specimen is of major importance for the success of any of the other methods.

From these, active phase stabilization has to be excluded. It is applicable only subject to the condition that the phase vibrates uniformly over all pixel elements of interest. This is certainly not the case for rigid body motions of the specimen cylinder relative to the conical mirror. As has been concluded in section 2.6.4, these motions cause the formation of unique correlation fringes, i.e. the amplitude of phase motion varies over the field of view.

Reducing necessary acquisition time itself does not compensate mechanical vibrations, but offers the possibility to effectively freeze them into the phase map. Compensation of vibration may be accomplished by post-processing the phase maps with dedicated algorithms.

A drawback of temporal phase-stepping in the presence of vibration is that the total acquisition time is, at least, doubled in comparison to spatial phase-stepping. It is, therefore, reasonable to expect that synchronous recording of interferograms at one deformation state yields better results than is attainable with temporal phase-stepping. That means that higher frequencies of vibration may be frozen in order to be compensated later by software.

d) Automation of measurement

The robust ESPI system should be able to measure automatically, i.e. detect inherently sign and size of radial displacements. It is further desired to reduce, by automation, the need for interaction of specially trained personal during the measurement process including post-processing.

Consequently, fringe tracking is not practical, since it is unable to detect the sign of radial displacement without additional information (i.e., fringe numbering). The interactive process of adding necessary side information increases computational effort and decreases velocity. Methods that rely on frequency domain processing naturally need more interaction with the user, decreasing measurement speed. On the other hand, they offer more accuracy since, usually, optimal filter cut-off may be found and applied.

		Active feed-back	Air cushions	Fringe tracking	2+1 Temporal phase-stepping	Spatial carrier phase measurement in		Spatial phase-stepping by		Spatial carrier phase-stepping
						Frequency domain	Space domain	Polarization control	Grating	
Complexity of experimental arrangement		High	High	Low	High	Low	Low	High	Medium	Low
Computational effort		High	No	High	Low	High	High	Medium	Medium	Low
Achievable noise compensation	Vibration	Partial	Yes	Yes	Yes	Yes	Yes	Yes	Yes	Yes
	Temperature	Partial	No	Partial	Partial	Partial	Partial	Partial	Partial	Partial
Optical quality requirements		Low	No	Low	Low	Low	Low	High	Medium	Low
Alignment requirements		Medium	no	Low	Low	Low	Low	High	Medium	Medium
Velocity of measurement				Low	High	Medium	Medium	High	High	High
Automatic sign detection				No	Yes	Yes	Yes	Yes	Yes	Yes
Automation of measurement				No	Yes	Partial	Yes	Yes	Yes	Yes
Number of recorded interferograms	Before deformation			1	≥3	1	1	≥3	1	1
	After deformation			1	≥3* (1**)	1	1	≥3* (1**)	1	1
Sensitivity to system imperfections				Medium	Low	Medium	Medium	High	High	High
Dynamic range, $\lvert \mathrm{grad}\,\delta \rvert_{max}$				Medium	High	Low	Low	High	High	Low
Spatial resolution				High	High	High	High	High	Low	Low
Achievable uncertainty				High	Low	Low	Medium	Medium	Medium	High
Price		Low	High	Low	High	Low	Low	Medium	Low	Low

* difference of phase approach ** phase of difference approach

Figure 3.10 Comparison of methods for vibration isolation in radial displacement measurement

e) Experimental arrangement

The less demanding methods with respect to complexity of the experimental arrangement are fringe tracking and spatial carrier methods, because they need only one interferogram per deformation state.

Other methods that reduce necessary acquisition time, generally require substantial hardware alterations, but less computational effort. Spatial phase-stepping requires complicated multi-camera alignment and tuning, together with alignment of polarization optics or diffraction gratings. In temporal phase-stepping, about the same effort is spent in expensive, fast phase-shifting devices and its synchronization to the interline transfer of the camera.

However, in contrast to spatial methods, where phase-step calibration, alignment and tuning procedures have to be executed only once, in temporal phase-stepping by heterodyning, the phase step to be introduced by frequency shift of laser light strongly depends upon the optical path difference between object leg and reference leg and, consequently, the cylinder diameter investigated. Therefore, temporal phase-stepping, where a new calibration of the phase-step would be necessary each time the cylinder diameter is changed, is clearly not suitable.

c) Dynamic range

The dynamic range is the range between minimum and maximum radial displacement that can be measured. Since the maximum gradient of δ should be less than the spatial carrier phase gradient, spatial carrier methods offer less dynamic range compared to phase-stepping.

d) Spatial resolution

The higher the spatial resolution of the phase map the larger the number of data points for radial displacements that can be calculated for the cylinder. Since the density of fringes increases (hence their visibility decreases) rapidly toward the center of the conical mirror, a high spatial resolution is of prior interest for the feasibility of radial displacement measurement. This is particularly true in the presence of vibration between the conical mirror and the cylinder, as this type of mechanical vibration increases, even more, the fringe density and, thus, reduces the effective measurement area of the cylinder.

Methods using several pixels from a single interferogram to calculate the phase offer less spatial resolution in the resulting phase map. Therefore, spatial carrier phase-stepping ESPI and multiple phase-stepped interferograms diffracted toward a single detector are clearly disadvantageous for radial displacement measurements.

e) Phase-measurement uncertainty

Because fringe tracking applies interpolation between loci of fringe extremes, phase-measurement uncertainties are comparatively large, although uncertainties of about one tenth of fringe order have been reported [20].

Because of the many restrictions of spatial carrier phase-stepping ESPI, its measurement uncertainty is large compared to other methods.

Compared to temporal phase-stepping, in spatial phase-stepping, additional error sources increase the measurement uncertainty, due to the fact that the interferograms are recorded by different cameras or by different parts of one detector. Additional error sources are pixel mismatch due to distortions and misalignments of the imaging optics, as well as intensity differences and noise due to imperfect optics for separate channels.

Comparing the properties of vibration compensating methods in Figure 3.10, one can notice that it is impossible to indicate a clear winner. However, some methods can be excluded. These are active feedback, that can not compensate tilt vibrations or vibrations between the conical mirror and the specimen, and fringe tracking, that does not allow the automation of measurement.

Since, in all circumstances, decorrelation of speckles should be avoided, isolation against large amplitudes of ground vibration is a primary condition for the success of any of the other methods in order to freeze the smaller amplitudes of phase vibration.

Furthermore, it can be concluded that the remaining methods complement each other. They demonstrate some trade-off between principal parameters shown in the comparison of Figure 3.10, basically, complexity of experimental arrangement, dynamic range and price on one side and complexity of processing, velocity and achievable measurement uncertainty on the other side.

Because of the high spatial resolution and dynamic range needed in radial displacement measurements, spatial phase-stepping by polarization control is believed the most promising method to freeze phase vibrations and, therefore, making compensation of mechanical vibration a real possibility.

3.2.4 New algorithms

Phase-shifting algorithms designed particularly for ESPI systems working in the subtraction mode may modify several characteristics for some of the existing phase-stepping methods shown in Figure 3.10. Because it is the phase difference between two deformation states which is of interest, determination of the absolute phase for individual deformation states is redundant. It is important to note that the difference measurement also makes it feasible to design algorithms that require fewer and simpler phase steps, thus reducing the total acquisition time per deformation state or demanding less complicated phase-shifting devices for modified phase-shifting techniques mentioned in the previous section.

Vikram *et al.* [61] found one such algorithm with the particular property that phase-step calibration is not needed. Containing five unknowns, that are mean intensity I_m , modulation intensity $I_m \cdot V$, random phase Φ, phase step α and the phase due to deformation δ which is of interest, at least five independent equations are required to recover δ. The algorithm developed by Vikram *et al* uses six equations, i.e. a total number of six interferograms has to be recorded. This is convenient because three interferograms (e.g. two equal phase steps $+\alpha$ and $-\alpha$) are required for each deformation state. Comparing the result with section 2.4.3 such property could only be achieved with algorithms using at least three equal phase steps.

Assuming the phase step is known, the necessary number of interferograms can be further reduced. With four unknowns a total number of four interferograms can be shown to be sufficient to determine the phase change δ. Using this constraint, a new single-phase-step algorithm has been proposed [53] which requires storage of only two interferograms per deformation state. The intensities of these interferograms can be expressed by

$$\begin{array}{ll} \underline{\text{before deformation:}} & \underline{\text{after deformation:}} \\ I_1 = I_m[1 + V\cos\Phi] & I_3 = I_m[1 + V\cos(\Phi + \delta)] \\ I_2 = I_m[1 + V\cos(\Phi - \alpha)] & I_4 = I_m[1 + V\cos(\Phi + \delta - \alpha)] \end{array} \tag{3.6}$$

with α denoting the single phase step.

Assuming that mean intensity I_m and modulation $I_m V$ do not vary with small deformations, the following combinations of interferograms are possible:

$$\begin{aligned}(I_2 - I_3) + (I_1 - I_4) &= 4I_m V \cdot \sin\left(\frac{2\Phi + \delta - \alpha}{2}\right) \cdot \sin\frac{\delta}{2} \cdot \cos\frac{\alpha}{2} \\ (I_2 - I_3) - (I_1 - I_4) &= 4I_m V \cdot \sin\left(\frac{2\Phi + \delta - \alpha}{2}\right) \cdot \cos\frac{\delta}{2} \cdot \sin\frac{\alpha}{2}\end{aligned} \qquad (3.7).$$

Forming the ratio between the two terms of equation (3.7) yields the searched expression for the phase change δ

$$\delta = 2\arctan\left[\tan\left(\frac{\alpha}{2}\right) \cdot \frac{(I_2 - I_3) + (I_1 - I_4)}{(I_2 - I_3) - (I_1 - I_4)}\right] \qquad \mod 2\pi \qquad (3.8).$$

It can be shown, that the algorithm is less sensitive to imperfect phase-steps α and intensity noise, if the phase step is chosen $\alpha = 90°$.

Applying the phase-of-difference approach, the total number of interferograms may be reduced to three. Kerr *et al.* demonstrated such an algorithm that operates only with a single but known phase step [34]. It requires one interferogram before and two 90° phase-shifted interferograms after deformation, or vice versa.

before deformation:	after deformation:
$I_1 = I_m[1 + V\cos\Phi]$	$I_2 = I_m[1 + V\cos(\Phi + \delta)]$
	$I_3 = I_m[1 + V\cos(\Phi + \delta - \pi/2)]$

(3.9)

From these, two 90° phase-shifted speckle-correlation-fringe maps are formed by subtraction

$$\begin{aligned}I &= (I_1 - I_2)^2 = \{I_m \cdot V(\cos\Phi - \cos(\Phi + \delta))\}^2 \\ &= 4I_O I_R \cdot \{1 - \cos\delta - \cos(2\Phi + \delta) + \cos(2\Phi + \delta)\cos\delta\} \\ I_{\pi/2}^2 &= (I_1 - I_3)^2 = \{I_m \cdot V(\cos\Phi - \cos(\Phi + \delta - \pi/2))\}^2 \\ &= 4I_O I_R \cdot \{1 - \sin\delta - \sin(2\Phi + \delta) + \sin(2\Phi + \delta)\sin\delta\}\end{aligned} \qquad (3.10).$$

The high spatial frequency of the argument $2\Phi+\delta$ compared to δ clearly demonstrates the inherent noise of the raw correlation fringe maps. Therefore, they need to be smoothed by appropriate low-pass filter. If there are only very small variations of mean intensity and visibility over the detector area, the dc-terms of the filtered fringe maps may be removed without explicit knowledge of object and reference intensities, respectively. Only subject to that condition, the phase change δ is simply recovered by

$$\delta = \arctan\left(\frac{\{I_{\pi/2}^2\}_{BP}}{\{I^2\}_{BP}}\right) \qquad \mod 2\pi \qquad (3.11).$$

3.3 Conclusions

To the authors knowledge, a quasi-equal-path interferometer for ESPI using spatial phase-stepping by polarization control has not been reported yet. Such working principle would be essential to combine the two most promising noise-compensating methods. Because both methods make use of polarization control, it is reasonable to believe that their combination in an ESPI interferometer for measurement of radial displacements in cylinders increases significantly the complexity of its arrangement.

However, temperature turbulence in the beam paths, usually, causes much more trouble in an ESPI measurement than does dilation between optical components due to slow temperature drift during the loading process. Therefore, appropriate shielding of the beam paths is considered the most efficient countermeasure. In addition to that, it also contributes to conceive reasonable simple but robust interferometers for this particular measurement application.

The spatial phase-stepping method using polarization control can be simplified if an algorithm of only a single phase step is applied. Then, only two parallel channels are sufficient to generate and grab the necessary interferograms simultaneously, turning that particular interferometer more compact.

Such simplification may be obtained through application of existent single phase-step algorithms, but would continue to require the correlation between either three or four interferograms that have been captured by two cameras. This has to be based on the correlation between channels, i.e. each channel has to produces the same $I_m(x,y)$, $V(x,y)$, $\Phi(x,y)$ and $\delta(x,y)$ to compose an interferogram. With regard to the first three variables, but especially regarding the random phase of speckle $\Phi(x,y)$, such spatial synchronization between channels can only be accomplished in an approximation. As the experience of Haasteren *et al.* demonstrated, in practice, that means the introduction of expensive non-standard optical components together with very strict alignment conditions in which, for example, the two detectors need to be correlated by mechanical alignment within sub-pixel range. As a consequence, the robustness of such interferometer would be certainly lost.

The strict alignment requirements due to $\Phi(x,y)$ could be greatly relaxed, if the correlation of speckle interferograms between channels were no longer required. This could be achieved by, for example, modifying the algorithm proposed by Kerr *et al.* in such a form, that the entire information needed to obtain the sine and cosine components of the phase map is generated and recorded by two separate channels, respectively. Another advantageous result of this approach is an interferometer that requires only cheap standard optical components. The sine and cosine components may be obtained from the 90° phase-stepped correlation fringe patterns of equation (3.10) if their dc-terms $4I_OI_R$, that obviously become channel dependant, are removed prior to the smoothing process. Only then, equation (3.11) may be successfully applied, i.e. reasonable values for the phase measurement uncertainty become feasible.

Obviously, the simplification made by Kerr *et al.* is no longer valid and additional knowledge of object and reference intensities for each channel, respectively, is required. That means, additional four images need to be captured and stored during the experiment. However, they could be recorded sequentially since they are, in a good approximation, time invariant.

Theoretically, an algorithm should exist that requires two time critical, phase-stepped interferograms per deformation state and the time invariant mean intensities for each channel. The advantage of such algorithm, compared to a "spatial" modification of the previous one, would be that one requires only two additional images of mean intensities I_O+I_R which have better signal to noise ratio than their individual components I_O and I_R. This certainly helps to simplify the process of phase determination and decreases the phase measurement uncertainty.

4 New phase extraction algorithm

Following the basic idea to reduce the number of time-critical interferograms per deformation state and, hence, the number of parallel channels needed for their generation, a new phase extraction algorithm is proposed that incorporates the following characteristics:

- Applicable to ESPI in adverse conditions
- Reduces the number of time-critical speckle interferograms and, hence, parallel channels to a minimum of two
- Avoids strict mechanical alignment between channels by adding knowledge of time-invariant mean intensities to the algorithm
- Requires only standard optical components by introducing a 90° phase step in one of the channels during the loading process, rather than a definite phase step between channels
- Calculates the raw cosine and sine component of the phase due to deformation, i.e. the sine component from the phase-stepped channel
- Smoothed phase components due to deformation are obtained by low pass filtering
- Calculates the wrapped phase map due to deformation module 2π

It follows a detailed description of the new phase-step algorithm together with an error analysis that studies the behavior of the algorithm to various system error sources by means of numerical simulation. From the analysis, some important conclusions are drawn for a successful experimental implementation of this algorithm in a new interferometer.

4.1 Single-phase-step algorithm for phase-difference measurement in spatial phase-stepping ESPI

A new single-phase-step algorithm is proposed which requires storage of only two time critical interferograms per deformation state and the time invariant mean intensities. The two time-critical interferograms are produced in two parallel channels and captured simultaneously by two CCD cameras, respectively.

The algorithm is designed for spatial phase-stepping ESPI where the initial phase in the interference term is the phase of speckle that varies randomly over the imaging sensor. It requires only a single phase step introduced in one of the channels during the loading process.

If the two imaging sensors are aligned within a few pixels, the intensities of the time critical interferograms can be expressed by

	before deformation:	after deformation:
Camera A:	$I_1 = I_{mA}\left[1 + V_A \cos\Phi_A\right]$	$I_3 = I_{mB}\left[1 + V_A \cos(\Phi_A + \delta)\right]$
Camera B:	$I_2 = I_{mB}\left[1 + V_B \cos(\Phi_B - \pi/4)\right]$	$I_4 = I_{mB}\left[1 + V_B \cos(\Phi_B + \delta + \pi/4)\right]$

(4.1).

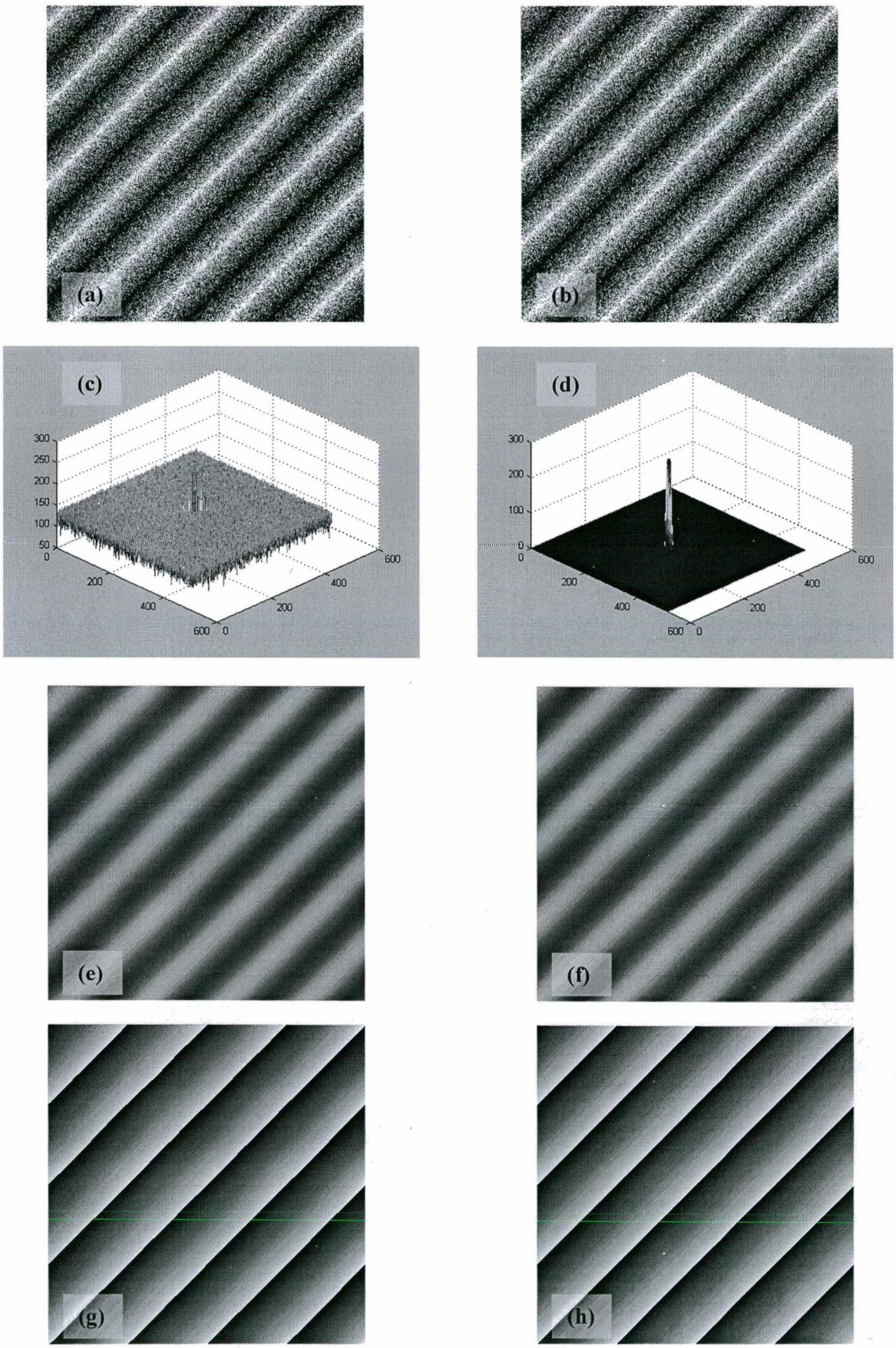

Figure 4.1 (a) raw sine δ, (b) raw cosine δ, (c) Fourier spectrum of (b), (d) Filter mask: 2nd order Butterworth, (e) filtered sine δ, (f) filtered cosine δ, (g) calculated phase map δc, (h) input phase map δ

Assuming that mean intensities I_{mA}, I_{mB}, intensity modulations $I_{mA}V_A$, $I_{mB}V_B$ and initial phases of speckle Φ_A, Φ_B observed by the respective cameras do not vary with small deformations, then, mean intensities can be obtained at any time and the following combination of interferograms are feasible

$$\textit{Camera } A: \quad D = \frac{(I_1 + I_3 - 2I_{mA})^2 - (I_1 - I_3)^2}{(I_1 + I_3 - 2I_{mA})^2 + (I_1 - I_3)^2} = \frac{2(I_{mA}V_A)^2[\cos\delta + \cos(2\Phi_A + \delta)]}{2(I_{mA}V_A)^2[1 - \cos(2\Phi_A + \delta)\cos\delta]} \tag{4.2}$$

$$\textit{Camera } B: \quad N = \frac{(I_2 - I_4)^2 - (I_2 + I_4 - 2I_{mB})^2}{(I_2 - I_4)^2 + (I_2 + I_4 - 2I_{mB})^2} = \frac{2(I_{mB}V_B)^2[\sin\delta - \cos(2\Phi_B + \delta)]}{2(I_{mB}V_B)^2[1 - \cos(2\Phi_B + \delta)\sin\delta]} \tag{4.3}$$

Equations (4.2) and (4.3) represent the noisy cosine and sine components of the phase difference. Figure (4.1a,b) illustrates these noisy patterns obtained when a phase ramp is input. They may be smoothed by adequate low-pass filter, like shown in Figure (4.1c,d). After the filter process we have

$$\textit{Camera } A: \quad [D]_{LP} = m_A \cos\delta \tag{4.4}$$

$$\textit{Camera } B: \quad [N]_{LP} = m_B \sin\delta \tag{4.5}$$

shown in Figure (4.1e,f), where m_A and m_B are the modulations of the filtered cosine and sine components. They can be defined as

$$\begin{aligned} m_A &= \frac{\langle D\rangle_{max} - \langle D\rangle_{min}}{2} \\ m_B &= \frac{\langle N\rangle_{max} - \langle N\rangle_{min}}{2} \end{aligned} \tag{4.6},$$

where $\langle D\rangle_{max}$, $\langle N\rangle_{max}$ and $\langle D\rangle_{min}$, $\langle N\rangle_{min}$ are the maximum and minimum mean intensities of the raw phase components, respectively. Their values depend, basically, on fringe density, decorrelation of interferograms due to deformation and the proper filter process.

If an identical filter process is applied to equations (4.2) and (4.3) and if the two cameras are aligned sufficiently within the depth of focus, then $m_A = m_B$, and the phase due to deformation can be retrieved from equations (4.4) and (4.5) by

$$\delta c = \arctan\left(\frac{m_B \sin\delta}{m_A \cos\delta}\right) \qquad \mod 2\pi \tag{4.7}.$$

Figure 4.1 (g) is shown the measured phase ramp that can be compared to the input phase ramp δ in (h).

4.2 Error analysis

Any phase measurement algorithm is prone to errors and, hence, its performance in the presence of various system error sources need to be analyzed. The system error sources considered in this analysis are:

- Quantization of the detector signal I
- High fringe density produced by the phase change δ
- Poor intensity modulation $I_m V$
- Intensity noise η
- Linear phase-step error ε

Including these error sources into equation (4.1) gives

	before deformation:	after deformation:
A:	$I_1 = I_{mA}\left[1 + V_A \cos\Phi_A\right] + \eta$	$I_3 = I_{mB}\left[1 + V_A \cos(\Phi_A + \delta)\right] + \eta$
B:	$I_2 = I_{mB}\left[1 + V_B \cos\left(\Phi_B - \left(\frac{\pi}{4} + \varepsilon\right)\right)\right] + \eta$	$I_4 = I_{mB}\left[1 + V_B \cos\left(\Phi_B + \delta + \left(\frac{\pi}{4} + \varepsilon\right)\right)\right] + \eta$

(4.8)

Due to the complexity of the algorithm, it is impractical to find an analytical solution for each error source in order to describe its contribution to the phase measurement uncertainty. Therefore, the performance of the algorithm is basically studied by means of numerical simulation. The influence of each error source is estimated by applying the algorithm to computer generated speckle patterns, based on the equations in (4.8).

The phase measurement uncertainty has to be determined relative to some reference standard. As standard serve several continuous phase ramps, generating straight equidistant fringes over a 512 by 512 matrix.. After processing, the calculated phase δc is compared to the standard phase ramp δ. Subtracting image (h) from image (g) in figure 4.1 yields the map of phase error. Figure 4.2(a) illustrates a possible result with an off-set of 128 gray levels added for better visualization. Figure 4.2 (b) shows the three-dimensional version of (a).

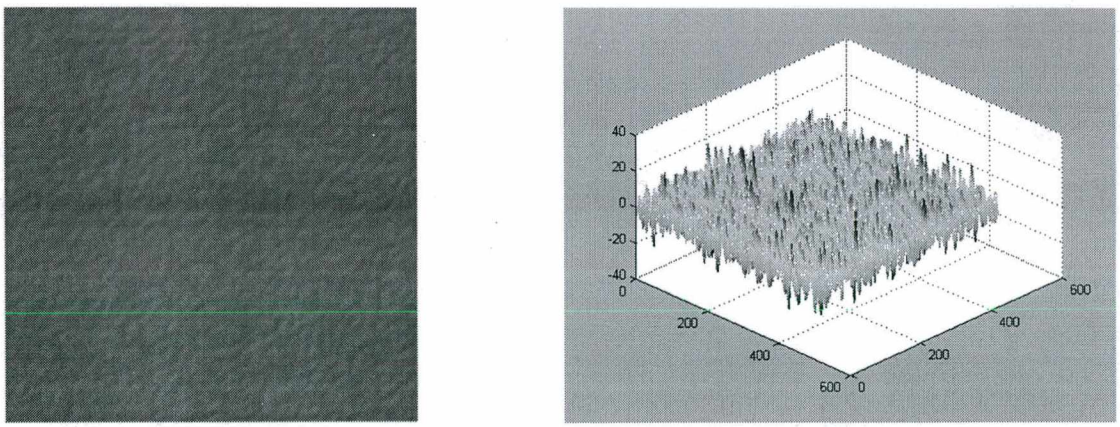

(a) **(b)**

Figure 4.2 (a) Map of phase error [gray level] + 128, (b) 3D plot of phase error [degree]

The histogram of the map of phase error is plotted in Figure 4.3 (a). The distribution may vary substantially with disturbances and the type of phase input. It does neither need to be symmetric nor to be centered around zero phase error. Therefore, if the modulus of phase error is considered instead, like in Figure 4.3 (b), its cumulative sum (c) may be used to define a maximum phase error for an established confidence, say, 99% of the image. Figure 4.3 gives an illustration. In the present simulation, the maximum phase error was defined for 99.98% of the image. That means that only 52 pixels out of a total of 262144 contain higher phase errors than defined above.

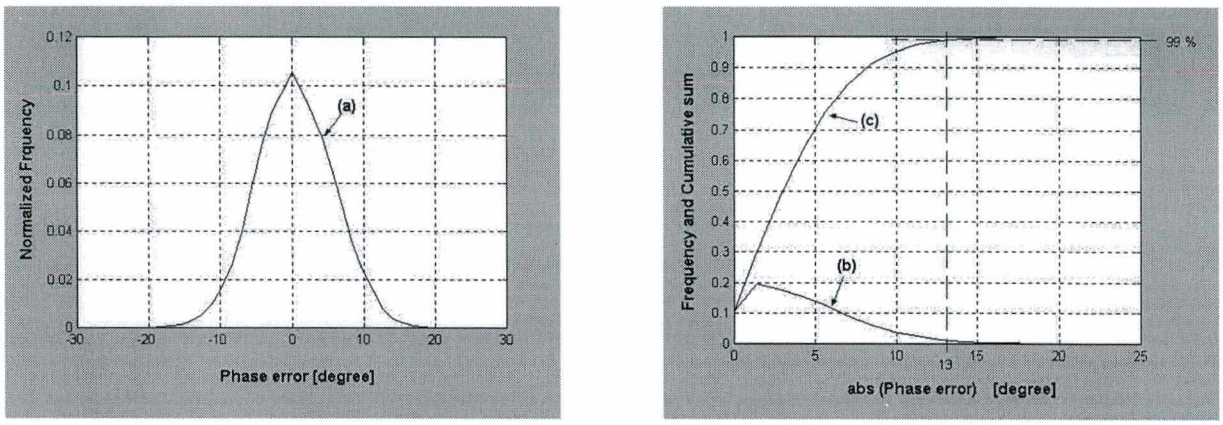

**Figure 4.3 (a) Distribution of phase error in the absence of disturbances,
(b) Distribution of the modulus of phase error of (a),
(c) Cumulative sum of (b)**

Even if all parameters are held constant, a spread of maximum phase error is observed for repeated simulation runs. This spread is due to the noisy speckle patterns in equation (4.8) that serve as input to a rather complex process of phase calculation, including low-pass filtering. However, for ≥ 20 simulation runs the maximum phase error shows an almost normal distribution and the upper limit of the maximum phase error, $E_{max}(\delta c)$, can be calculated with 95% confidence by the mean plus twice the standard deviation.

4.2.1 Quantization of the detector signal and poor intensity modulation

The detector signal I is usually digitized to 8 bit, thus, the interferograms in equation (4.8) may contain only $Q = 2^8 = 256$ discrete intensity levels, also denominated gray levels. This entire dynamic range is only used for pixels that show perfect intensity modulation $I_m V = Q/2$ implying intensity ratio $r = 1$ and $I_{sat}/I_R = 4$. Therefore, perfect intensity modulation means 128 gray levels for 8 bit quantization.

In chapter 2.3.2 it was discussed that perfect modulation can not be fulfilled for all pixels. In ESPI, intensity modulation will vary from pixel to pixel. Even in the best case, about 5% of the image will modulate above saturation level whereas other parts modulate very poorly or do not modulated at all. However, pixels that modulate at 128 gray levels are very rare in real ESPI experiments. Typically, mean modulation was found between 15 and 20 gray levels only, with varying distributions.

The distribution of intensity modulation is difficult to predict because it depends on many parameters of the particular optical set-up, mainly the number o speckles resolved on each pixel and decorrelation of speckles due to deformation. But, the smaller the intensity modulation of speckles the more quantization limits the measurement accuracy achievable with ESPI.

For simplicity, a rectangular distribution is adopted in this computer simulation. The values for $I_m V$, assigned to each pixel in equations (4.8), vary uniformly between zero and an upper limit.

Figure 4.4 shows the estimated maximum phase error as a function of the upper limit of intensity modulation, if a phase ramp of $32 \cdot 2\pi$ is input. Such a phase ramp will generate 32 diagonal fringes over a 512 x 512 imaging sensor, thus, causing a fringe density of 1 fringe / 32 pixels. The figure illustrates the exponential increase of the phase error with decreasing intensity modulation. In the absence of any other disturbance, a maximum phase measurement error around 21° (or 1/17 wave) may be expected.

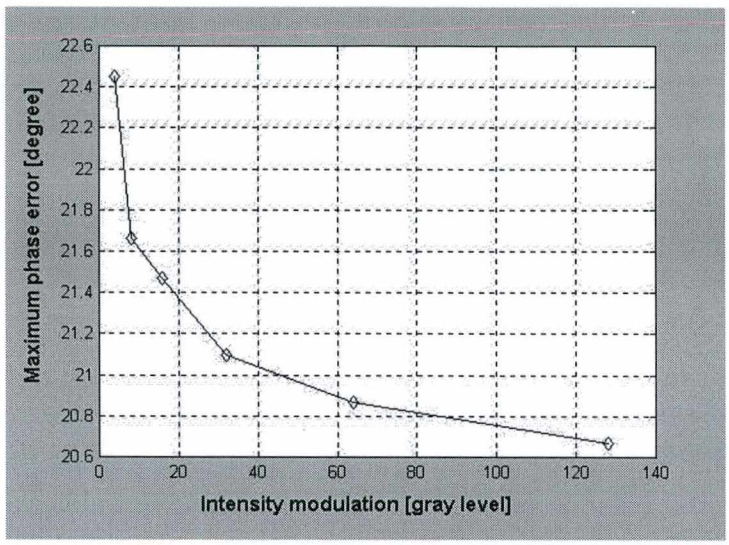

Figure 4.4 Maximum phase error as a function of maximum intensity modulation

4.2.2 Fringe density

The dependency of the phase error upon fringe density may be illustrated applying equation (4.6) to figures 4.1 a, b. The higher the fringe density the noisier the raw phase maps and, therefore, the smaller the modulation for the filtered sine and cosine components that can be obtained. Smaller modulations induce larger errors to the phase map, which is calculated by the arctan function of the smoothed components.

In order to quantify this influence, one can apply the following rule of thumb: If one wave occupies N pixels, then, the entire intensity variation, occupying half a fringe period, is digitized by N/2 pixels. That means that one wave is digitized with merely N/2 discrete intensity levels. The error in a digital system is at least ± LSB. Analogue to that rule, if one allows to occur an error of one discrete intensity level, the error propagates until the phase map which, obviously, can not be determined anymore with less than about $N/2 \cdot 360°$ phase uncertainty.

This rule of thumb was tested numerically for several fringe densities. According to experimental data, the upper limit of intensity modulation was adjusted to 32 gray levels. Figure 4.5 shows the results of the numerical simulation. As expected, the phase error increases with higher fringe density. An almost linear dependency can be detected even for poor modulation of only 4 gray levels. Poor intensity modulation will deteriorate the results, but the dominant influence of the fringe density upon the phase error can be clearly seen. The numerical data shows good accordance with the rule of thumb, plotted as a dotted line in figure 4.5.

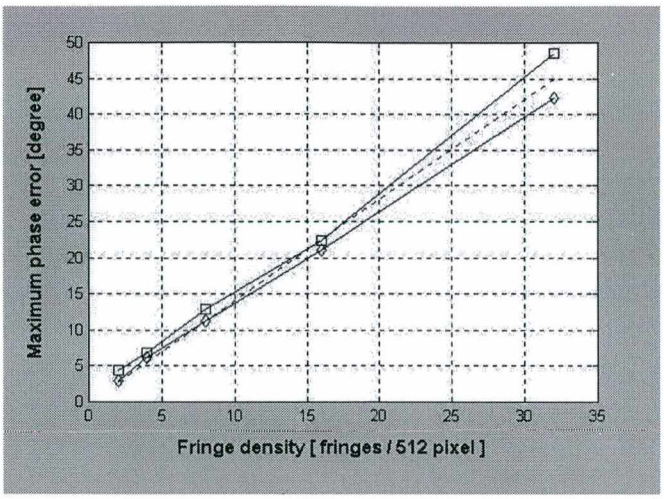

Figure 4.5 Maximum phase measurement error as a function of fringe density, Maximum intensity modulation [gray level] as parameter: (circles = 32, squares = 4)

4.2.3 Intensity noise

Intensity noise decreases further the performance of any phase measurement algorithm, since it shrinks the effective number of bits (ENOB's) for quantization of the interferograms. Noise adds to the intensity signal basically between the imaging device and the A/D converter. For example, if an analog camera is used and the A/D conversion occurs on the frame grabber, at least 1 digitizing bit is lost already over their interconnection of, usually, several meters of coax.

Intensity noise in form of white noise can be simulated by simply adding random numbers of uniform distribution to the pixel intensities. For each interferogram a new matrix of random numbers is generated. The random values range from zero to 2^n-1, n being the number of bits the noise is planned to occupy. For instance, 1 bit of noise adds {0, 1}, two bits of noise {0, 1, 2, 3} and so on.

The results of this simulation are shown in Figure 4.6. An increase of more than 30 % has to be expected for the maximum phase error if the intensity noise occupies 3 bit. Assuming that an analogue camera output, connected to the frame grabber over 5 meters of coax, introduces only 1 bit of noise to the intensity patterns and fringe density is not higher than about 1 fringe/ 30 pixel, the proposed algorithm still assures phase measurements with a maximum phase error $E_{max}(\delta) \leq 24^\circ$ (or 1/15 wave).

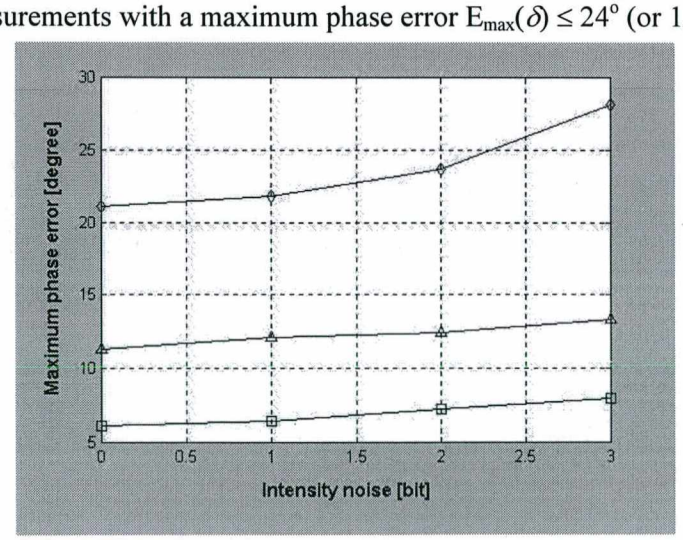

Figure 4.6 Influence of intensity noise upon maximum phase measurement error, Parameter: fringe density [fringes/pixel] (squares = 1/128, triangles = 1/64, diamonds = 1/32), maximum intensity modulation = 32 gray level

4.2.4 Linear phase-step error

For proper calculation of phase change δ, the phase step between the interferograms of channel B must be $\pi/2$. This has to be accomplished by calibration of the phase-shifting device. The remaining uncertainty of the phase step ε causes a phase error $E(\delta)$. It can be shown that this phase error depends on the phase-step error ε (only linear for a single phase step) and the phase change δ by

$$E(\delta) = \arctan\left[\frac{\sin(\delta+\varepsilon)}{\cos\delta}\right] - \delta \qquad (4.9).$$

Equation (4.4) states that the error oscillates at twice the frequency of δ and, for small values of ε, reaches maximum at approximately $\delta = k\pi$ (k = 0, 1, 2...). Figure 4.7 gives an illustration. It can be seen that the maximum error $E_{max}(\delta) = \varepsilon$.

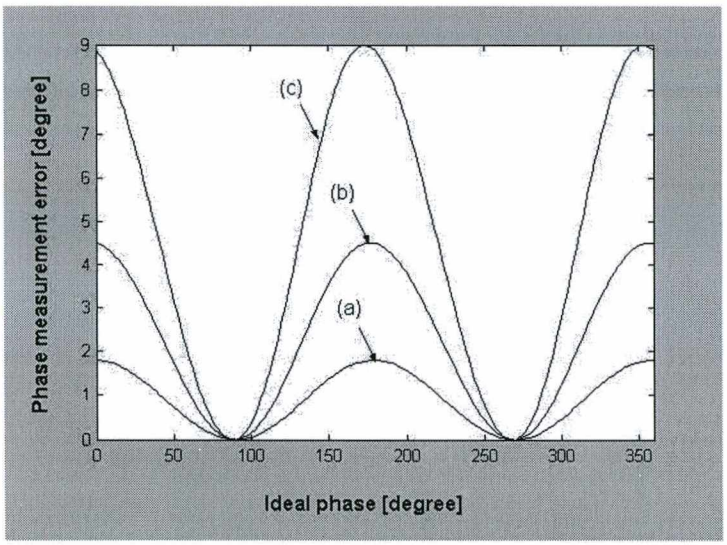

Figure 4.7 Phase measurement error as a function of linear phase-step error ε and phase change δ, (a) $\varepsilon = 1.8^0$ (2 % of $\pi/2$), (b) $\varepsilon = 4.5^0$ (5 % of $\pi/2$), (c) $\varepsilon = 9^0$ (10 % of $\pi/2$)

How phase-step errors can be detected in the measured phase map is illustrated in figure 4.8, (a) showing a convenient input in gray level: a rather small standard phase ramp of 1 fringe / 512 pixel in diagonal direction over a matrix of 512 x 512 pixels. In the measured phase (b) one can already notice the phase oscillation caused by the phase-step error. The difference in gray level (c) between the measured phase (b) and the standard phase ramp (a) clearly reveals a phase-step error of -10 %.

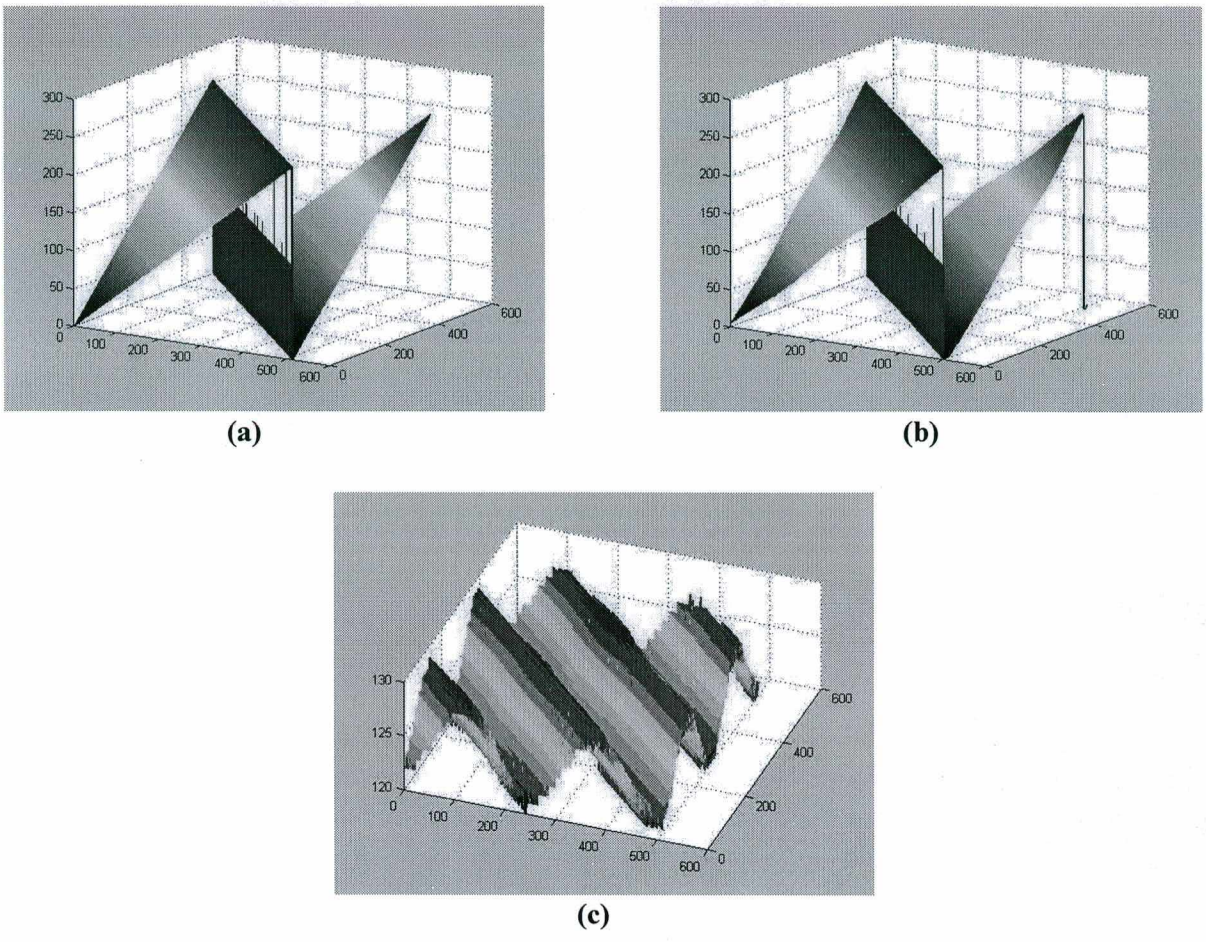

Figure 4.8 Detection of phase-step error ε (c) by comparison of the measured phase ramp δc (b) with the standard phase ramp δ (a), maximum intensity modulation = 32 gray level

4.3 Conclusions

The studied influences can be classified according to their contribution to the phase measurement error.

(1) The performance of the algorithm depends, like any other, most upon the fringe density. In multiple phase-step algorithms, this influence upon the phase measurement error is reduced due to the redundancy of information captured. However, the goal of the proposed algorithm is to cut that redundancy in order to reduce the necessary acquisition time. Obviously, this advantage has to be bought at the expense of increased phase error. A comparison of algorithms is given in figure 4.9 (a). It can be concluded that the proposed single phase-step algorithm is more sensitive to fringe density than the standard phase-stepping algorithm (see equation 3.20 in chapter 2.3.1). There is nothing that can be done to lower this major portion to the phase uncertainty.

(2) The proposed algorithm is as sensitive to linear phase-step errors as the standard phase-stepping algorithm, i.e. the phase-step error is passed without reduction to the phase map. Therefore, a lot of attention should be given to the phase-stepping device and its proper calibration.

This also implies care for proper alignment of cameras, since misalignment can be viewed as a corresponding phase-step error. If there is any misalignment between channels A and B (in % of the densest wave observed), this error is also passed without reduction to the phase map. For example, misalignment of 1 pixel between cameras observing 1 fringe / 32 pixels leads to phase errors of 1/32 of a wave.

(3) As can be concluded from figure 4.9 (b), the proposed algorithm is also more sensitive to intensity noise than is the standard phase-stepping algorithm. Although the phase error caused by noise is less critical than the previous influences, its amount can be diminished by digitizing the images as soon as possible. Certainly, the use of digital cameras would be the best solution to avoid problems with noise.

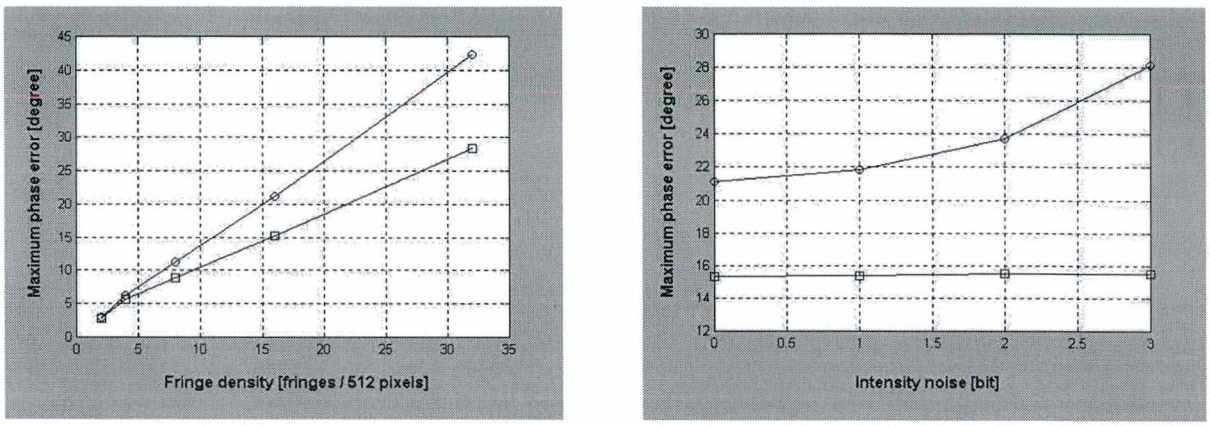

(a) **(b)**

Figure 4.9 Maximum phase error as a function of (a) fringe density and (b) intensity noise, Comparison of phase step-algorithms (circles: proposed algorithm, squares: 3-step algorithm)

Poor intensity modulation contributes far less to the phase measurement error than the other influences. The reason is found in the filter process where an optimal filter cut-off could be applied for equidistant fringes. Analyzing the filter result of several simulations with varying fringe density the optimal cut-off frequency was adjusted to

$$\begin{aligned} f_{x\,\mathrm{cut}} &= 768 \cdot \text{fringe density in x - direction} \\ f_{y\,\mathrm{cut}} &= 768 \cdot \text{fringe density in } y\text{ - direction} \end{aligned} \qquad (4.10).$$

The filter mask multiplied was that corresponding to a low-pass Butterworth filter of 2nd order.
If optimal filter cut-off is applied, even only a few discrete intensity levels in the raw phase components, caused by quite a poor modulation of speckles, are sufficient because smoothing can be viewed as an equalization of the image histogram between $\langle D \rangle_{\min}$ and $\langle D \rangle_{\max}$. Thus, discrete intensity levels are recovered that rested unoccupied before.

Finally, if only 1 out of 8 bits is lost due to intensity noise and the measurement system observes fringe densities ≤ 1 fringe / 32 pixels with phase-step errors of ≤ 2 %, a total phase measurement uncertainty of ≤ 24° (1/15 of a wave) is feasible with the proposed algorithm.

5 Interferometer configuration

5.1 Implementation of the single phase-step algorithm

The proposed algorithm was implemented in an out-of plane sensitive interferometer with smooth in-line reference. The basic configuration is shown in Figure 5.1 (a) for testing the proposed algorithm and (b) the measurement of radial displacements in inner cylindrical surfaces. The optical configuration of the interferometer is based on polarization phase-stepping where the object beam and reference beam are polarized perpendicular to each other.

The light of an Ar^+ laser (λ = 514 nm), is coupled into a monomode fiber. The fiber serves as a light guide and a spatial filter simultaneously. The laser light is coupled out at the interferometer head, where it propagates, first, through a glass window to illuminate the object under investigation. A minor portion of light, approximately 3 % of the object beam intensity, is reflected at the window and used as a smooth reference.

In order to measure only radial displacements, the object beam is collimated and, then, directed to the conical mirror within the cylinder. In front of the conical mirror, a plane mirror is placed such that radial only illumination of the cylinder surface is obtained. For radial panoramic observation, a small hole is drilled at the center of the plane mirror which is positioned in the front-focal point of the imaging lens. In that position, the size of the hole represents the entrance pupil of the imaging system, i.e. defines also the speckle size in the image plane. The advantage of this set-up to an additional beam splitter is a better use of precious laser power.

The object is imaged by an imaging lens onto two CCD sensors simultaneously. Before recombination, object beam and reference beam are passed through a polarizer. If these polarizers are oriented orthogonal to each other, the detected beams contain light from the object and reference with linear orthogonal polarizations. Consequently, the intensity ratio can be adjusted for each channel individually by rotating a polarizer.

In order to introduce the 90° phase step between object beam and reference beam during the loading process, a wave plate of $\lambda/8$ retardation is rotated in front of the analyzer and CCD sensor of the second channel. First, the fast axis of the wave plate is aligned to the polarization of the reference beam. During the loading process, fast and slow axes are interchanged, resulting in a 90° phase step for orthogonal polarizations.

The mean intensities are obtained for each channel by very fast movement of the reference mirror over several waves during the CCD integration time or by separate acquisition of the reference and object intensities.

Two progressive scan cameras serve as imaging sensors. Each camera is connected to the frame grabber board from which they are simultaneously shuttered. The captured intensities are digitized by the proper cameras and their outputs are sequentially read by one frame grabber on a host computer. A software on the host computer controls the measurement process, including tools for image processing. The phase change δ is recovered applying equations (4.2) to (4.7), the phase is unwrapped by a phase-unwrapping algorithm and, finally, radial displacements are calculated from equation (2.7).

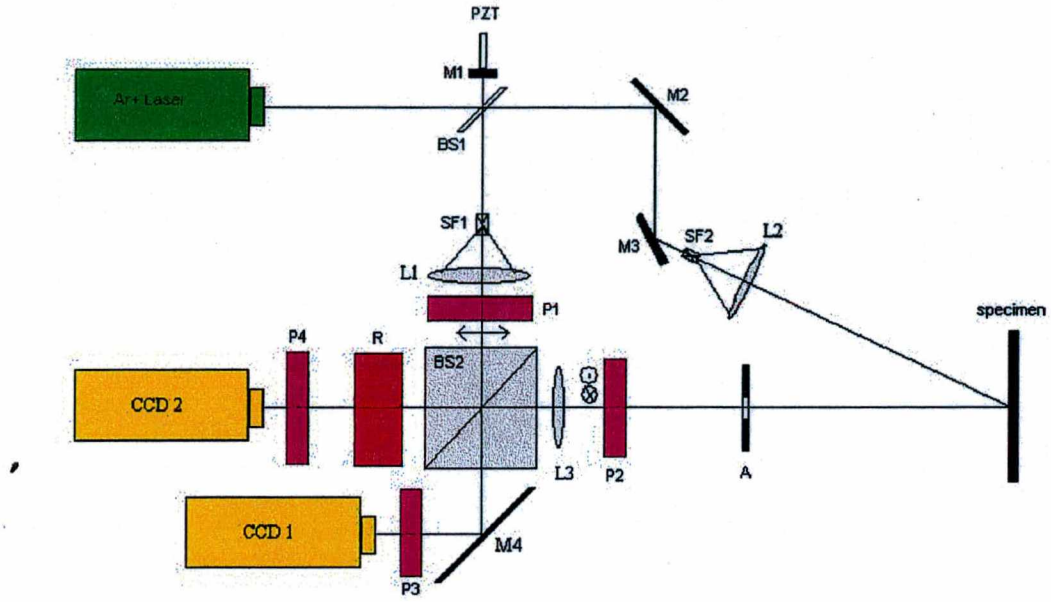

(a)

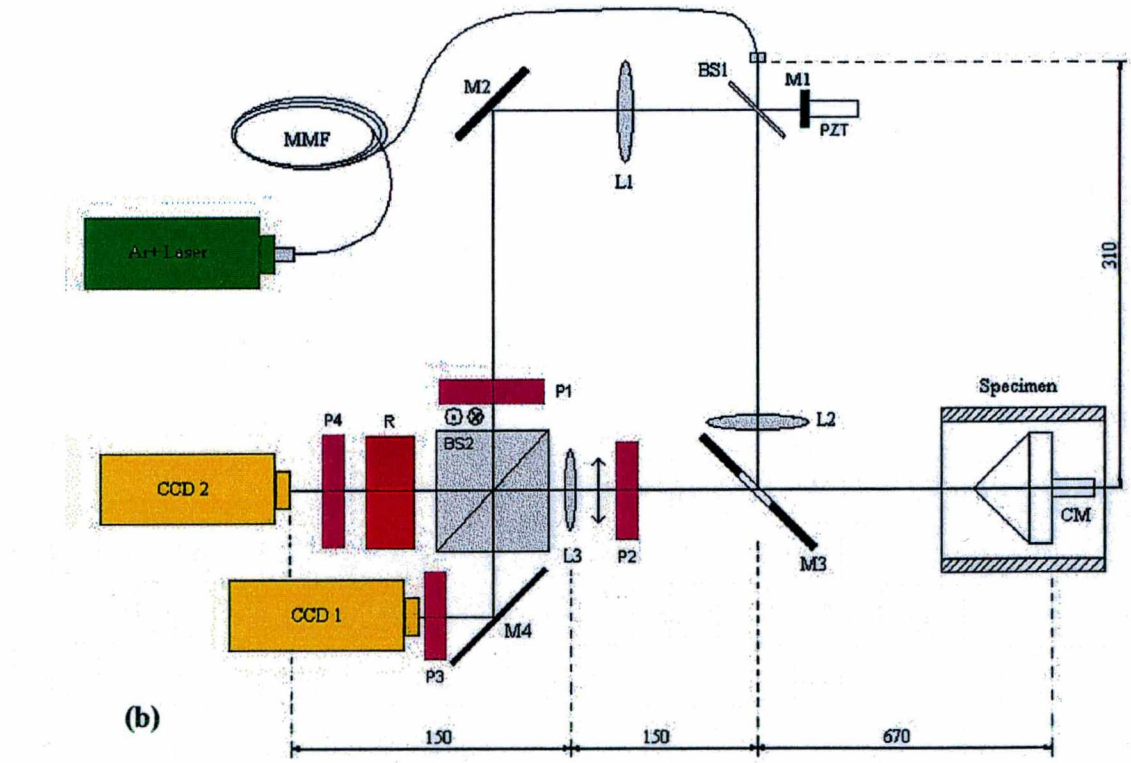

(b)

Figure 5.1 Interferometer configuration (a) out-of plane sensitive ESPI (b) radial sensitive ESPI, BS: beam splitter, M: mirror, CM: conical mirror, L: lens, P: polarizer, R: $\lambda/8$ retardation plate, SF: spatial filter, PZT: piezo translator, MMF: monomode fiber

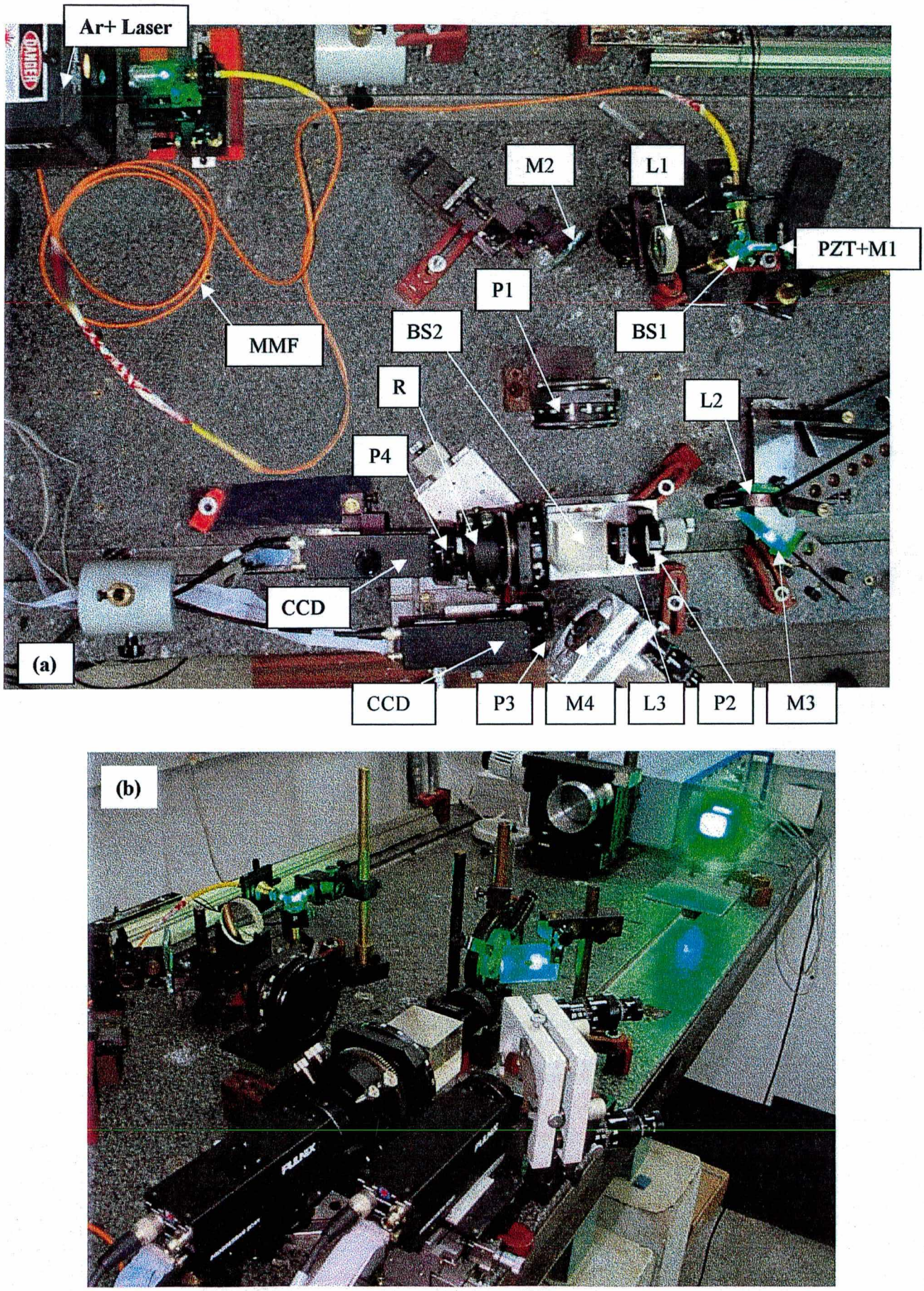

Figure 5.2 Interferometer configuration (a) interferometer head and (b) specimen on optical bench

5.2 Construction and alignment

The following section gives a closer view to each module, its specifications and alignment.

5.2.1 The light source

Because a pulsed laser source was not available with output energy/pulse of the order of 1 mJ, an Ar+ laser from Coherent™ was used instead in the experiments. Its basic properties can be summarized as follows:

- Wavelength in the visible spectrum: $\lambda = 514.5$ nm
- Continuous wave
- High power TEM_{00} output (> 1.5 W achievable)
- Single mode output with Fabry Perot Etalon (coherence length > 40 m)

In order to guarantee enough autonomy for the interferometer, independent of the choice of laser source, the laser light was coupled into a fiber. Its major performance factor is the normalized frequency:

$$F = \frac{\pi \cdot NA \cdot a}{\lambda} \quad \text{with} \quad NA = \sqrt{n_{Core}^2 - n_{cladding}^2} \approx 0.1 \tag{5.1}$$

where NA denotes the numerical aperture of the fiber and a is its core diameter. To transmit exclusively the fundamental mode, the normalized frequency has to be smaller than 2.405. With a cut-off wavelength of 5...10 % shorter than their operating wavelength (here 514.5 nm) equation 5.1 results in a core diameter of < 3.5 µm. Only then, the fiber preserves the spatial coherence of the laser beam and acts as an effective spatial filter. However, due to the dependency of the refractive index n upon ambient conditions, principally temperature and bending stress, the fiber will rotate the polarization of the exiting beam as ambient conditions change.

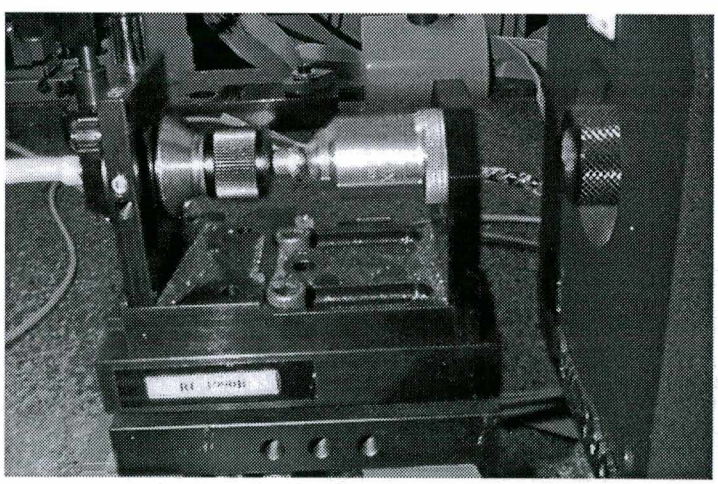

Figure 5.3 Precision fiber coupler

Efficient coupling of the Gaussian laser beam to the fiber was achieved by a precision fiber coupler, shown in Figure 5.3 It pivots the beam to the fiber core with a lateral resolution < 0.1 µm.

Maximal coupling efficiency obtained was ≤ 36 %, measured by a power meter with measurement range from 0...35 mW. Due to the high power densities involved, the exact output power delivered by the fiber in most experiments remains unknown.

The power was estimated by extrapolation like shown in Figure 5.4.

		Measurement of Laser power [mW]				
		I	**II**	**III**	**IV**	**V (maximum)**
Indication for	**Ar + Laser**	20	40	60	120	1200
	I_O	7	13	21	35 (saturated)	≈ 420 (extrapolated)
	I_R	0.19	0.37	0.54	1.00	9,50

Figure 5.4 Measurement of Laser power

Special care had to be taken in order to guarantee a constant illumination which is crucial for the success of the proposed algorithm. The output power at the Ar+ Laser could be adjusted up to 1.2 W which yielded about 400 mW to illuminate the object. For higher outputs the fiber end, suspended in air within the precision fiber coupler, began to vibrate due to thermal effects caused by the large power density.

5.2.2 The interferometer head

The interferometer head is based on a polarizing Mach-Zehnder interferometer where the beams are polarized perpendicular to each other. It uses only standard optical components like a glass window, a beam splitter, collimating lenses and polarization filter.

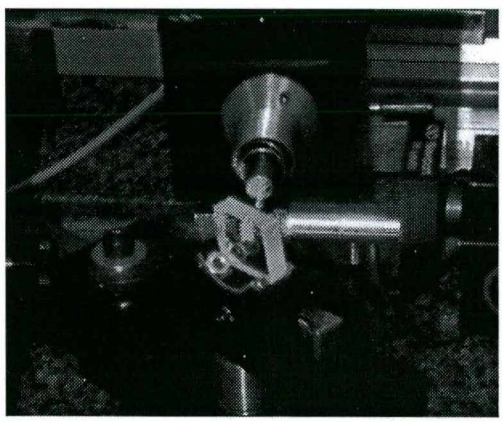

Figure 5.5 Fiber output, glass window BS1 and mirror M1 on piezo translator

The glass window BS1 (17 mm x 14 mm x 5mm) is used for initial beam division. A minor portion of the incident light from the fiber is reflected to the small mirror M1 attached to the piezo translator PZT and passed back through the window. Figure 5.5 shows the experimental set-up. The piezo translator and mirror were introduced in order to implement the capability to measure phase also by temporal phase-stepping for comparison of algorithms. This set-up makes it also feasible to measure the intensity mean for each channel by rapidly moving the mirror over several waves during the integration time of the camera.

The reflected beam is collimated to ∅ 20 mm by L1 (f = 100 mm) and serves as a smooth reference. Mirror M3 is used to stir the major portion of light, which passes through the glass window, to the object. For measurements of radial displacements, the object beam is, first, collimated to ∅ 50 mm by lens L2 (f = 250 mm).

Mirror M3 (80 mm x 60 mm x 4 mm) is located such to allow radial illumination and observation of the specimen, simultaneously. For observation, a 10 mm hole, was drilled at 45°. Figure 5.6 shows mirror M3 in the experimental set-up.

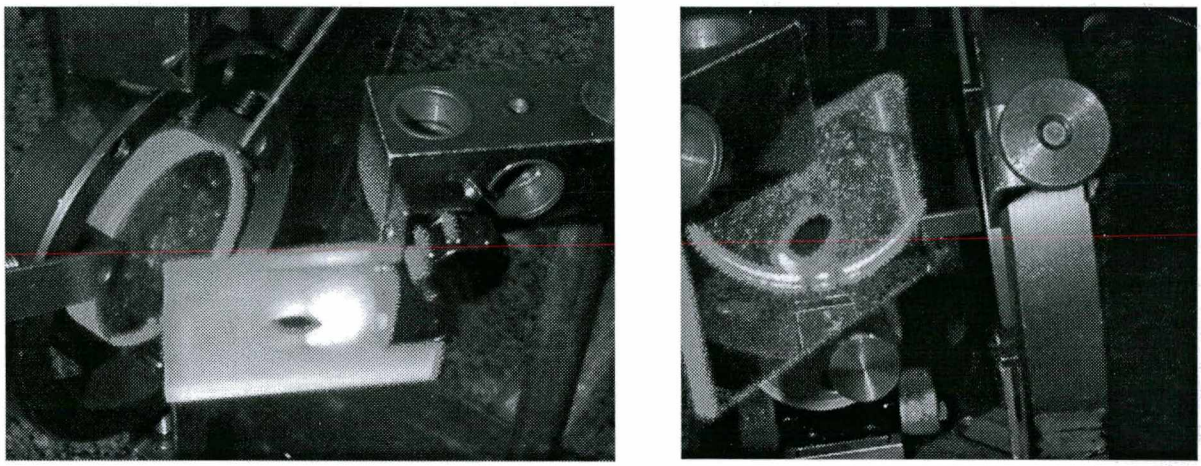

Figure 5.6 Collimator L2 in front of mirror M3 with 10 mm hole, drilled at 45° for observation

The hole was placed in the front focal point of imaging lens L3 (f = 150 mm). In that position, it defines the amount of light that passes from the object and the size of the imaged speckles. The hole diameter was chosen to compromise between these two parameters. All lenses are positive achromats for minimal spherical aberrations and wavefront distortion.

Object and reference beams are recombined and split into two channels by BS2 (50 x 50 x 50 mm) for observation. In front of the beam splitter, sheet polarizer filter out the s-component of the object beam and the p-component of the reference beam. Only in that condition, beam splitter with hybrid film coatings, like used as BS2, will still assure perpendicular polarization states of object and reference beams after recombination. Therefore, careful adjustment of the orientation of polarizers is necessary. This was achieved by means of rugged rotational stages. The uncertainty for orientation of the polarizer was estimated $\leq 0.5°$, which results in an estimated maximum deviation from perpendicularity of the two polarizations of $\leq 1°$.

5.2.3 The specimen fixation

As mentioned in chapter 2, the interferometer is very sensitive to movements of the conical mirror relative to the cylinder. A stiff attachment of the conical mirror to the specimen is important to prevent large vibrations between them. Therefore, the conical mirror (∅ 50 mm x 40 mm) shown in figure 5.7 (b) was mounted on a heavy steel base together with the cylinder. Figure 5.7 (a) gives an illustration of the construction. The mirror was fixed from behind, like shown in figure 5.7 (a) and (c), allowing height adjustments. The specimen (∅ 70 mm x 150 mm x 5 mm aluminum) rested on a adjustable magnetic base allowing lateral alignment. Deformation of the cylinder was obtained by loading weights.

Two additional specimen were prepared for testing purposes. One is a centrally loaded aluminum plate of 5 mm thickness and the other is a lightweight aluminum plate (50 mm x 40 mm x 1 mm) attached to a PZT. Both specimen are shown in Figure 5.8.

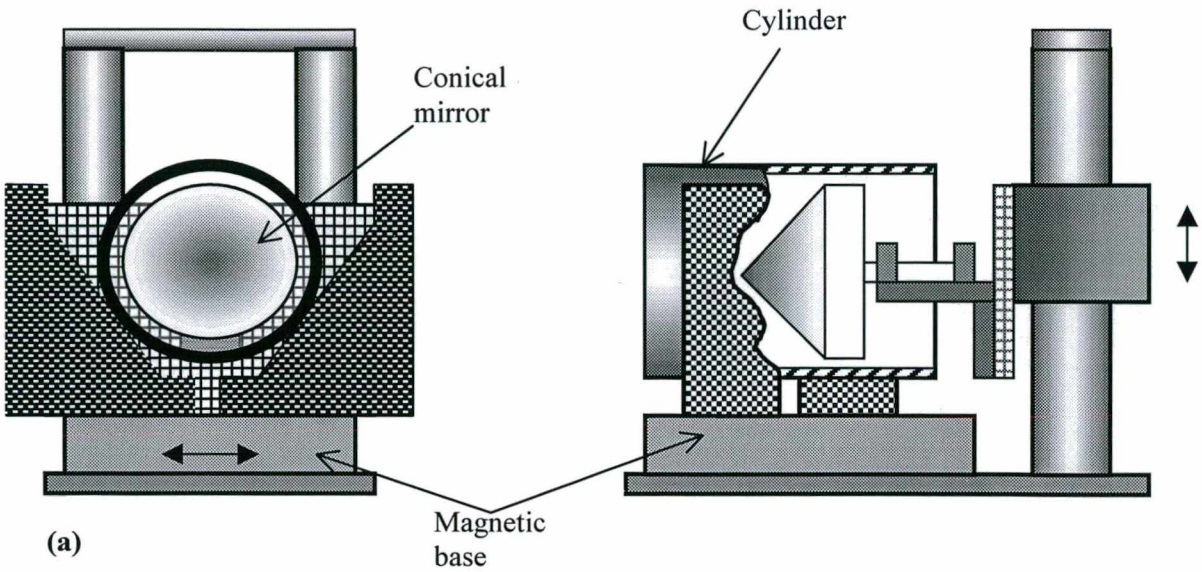

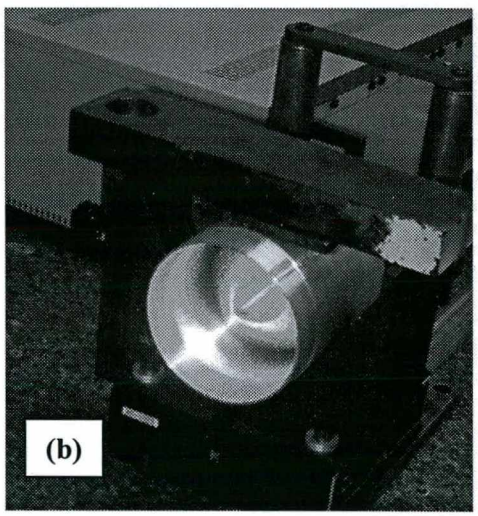

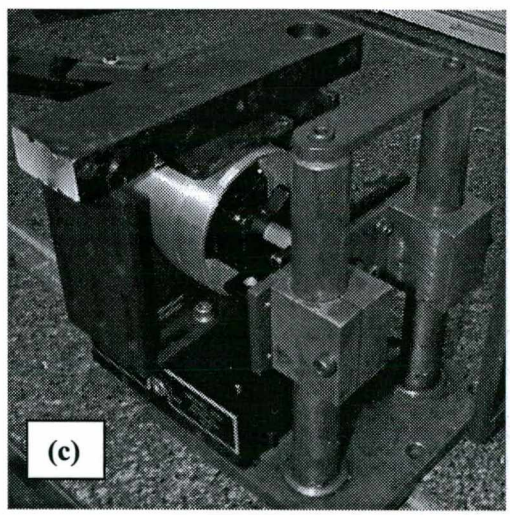

Figure 5.7 (a) Construction of specimen fixation, (b) Conical mirror illuminating the test cylinder, (c) Fixation of conical mirror from behind

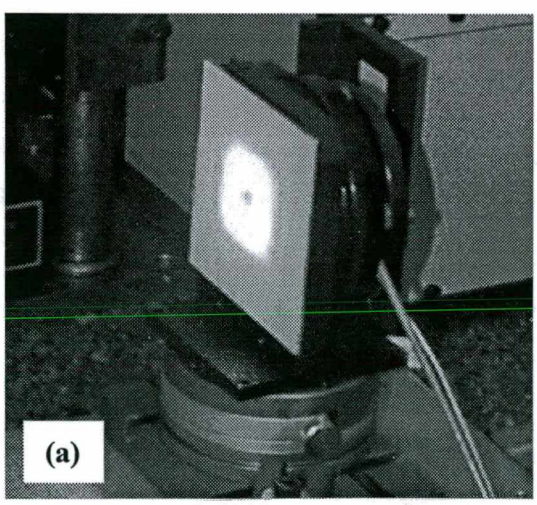

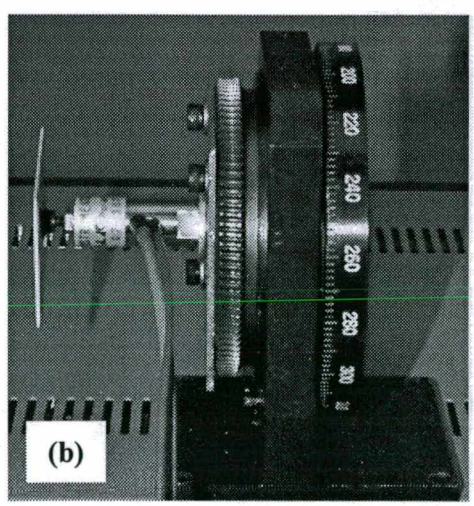

Figure 5.8 (a) centrally loaded aluminum plate, (b) small aluminum plate mounted on a PZT

5.2.4 The phase shifter

As phase shifter served a retardation plate from Meadowlark Optics™ with the following specifications[43]:

- Retarder material: birefringent polymer
- Substrate material: BK 7
- Wavelength: $\lambda = 514.5$ nm
- Nominal retardance: $\lambda/8$ or 0.125 waves
- Retardance calibration: 0.1251 waves
- Transmitted wavefront distortion: $\lambda/5$
- Beam deviation: 1 arc min
- Temperature sensitivity: -0.03 %/K
- Reflectance per surface: 0.5 %
- Clear aperture: 17.8 mm
- Temperature range: -20 °C to +50 °C
- Safe operating limit: 500 W/cm^2 CW

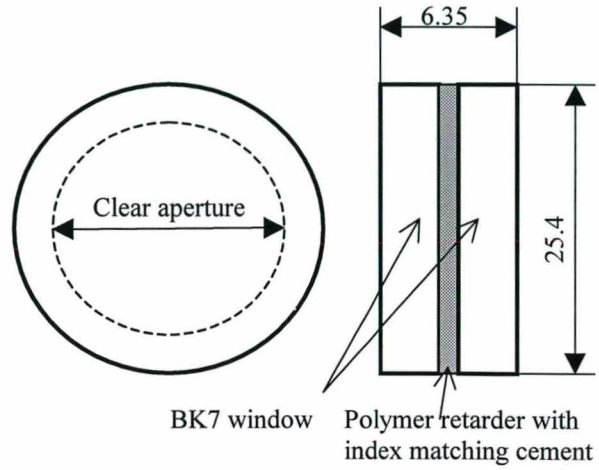

Figure 5.9 Precision polymer retarder

The polymer retarder assembly consists of birefringent polymer material laminated between two precision polished, optically flat BK7 windows. Antireflection coatings and index matching optical cement help to maximize transmission. The construction, shown in figure 5.9 ensures very good transmitted wavefront quality, while minimizing beam deviation and surface reflection losses.

A polymer retarder was chosen since it is a true zero-order retarder, thus, offering a large angular field-of-view. It changes by less than 1 % over a ± 10° incidence angle. With f = 150 mm for L3 and an aperture of D = 10 mm, defined by the hole diameter of mirror M3, the incidence angle is limited for the present interferometer to 1.9°. This leads to about 0.2 % uncertainty for retardation and, thus, 0.2 % uncertainty for the introduced phase step which is negligible compared to the other influences studied in chapter 4.

The temperature sensitivity of polymer retarders is about –0.03 %/K, allowing operation of the interferometer over a rather wide temperature range without significantly degrading the accuracy of the applied phase step.

Due to the lamination, the optical flats can not be cemented without small errors that lead to a slight wedge form of the assembly. The consequence is a small beam deviation that is critical for the proposed set-up, where the retarder was rotated 35 mm in front of the second CCD target. For example, if the retarder is rotated 90°, a beam deviation of 1 arc min already introduces an image shift of about 14 μm. With a speckle size adjusted to about 10 μm, that means the complete loss of speckle correlation which turns measurement impossible.

However, small beam deviations can be partially corrected by tilting the retarder. Figure 5.10 gives an illustration. Assuming, first, that fast or slow axis of the retarder are parallel to the plane formed by the wedge angle, see (a) in figure 5.10. Then, an incoming beam that is parallel to the optical axis will be deviated about $\Delta = 10$ μm in y-direction (or x-direction) from its ideal position, i.e. without a wedge. This would not be such of a problem, but if rotated 90°, each speckle is displaced between deformation states by $\sqrt{2}$ times the deviation Δ. It can be shown that the deviation Δ is compensated for beams that are parallel to the optical axis if the retarder is rotated 16.5 arc min around φ_x (or φ_y), like shown in figure 5.10 (b).

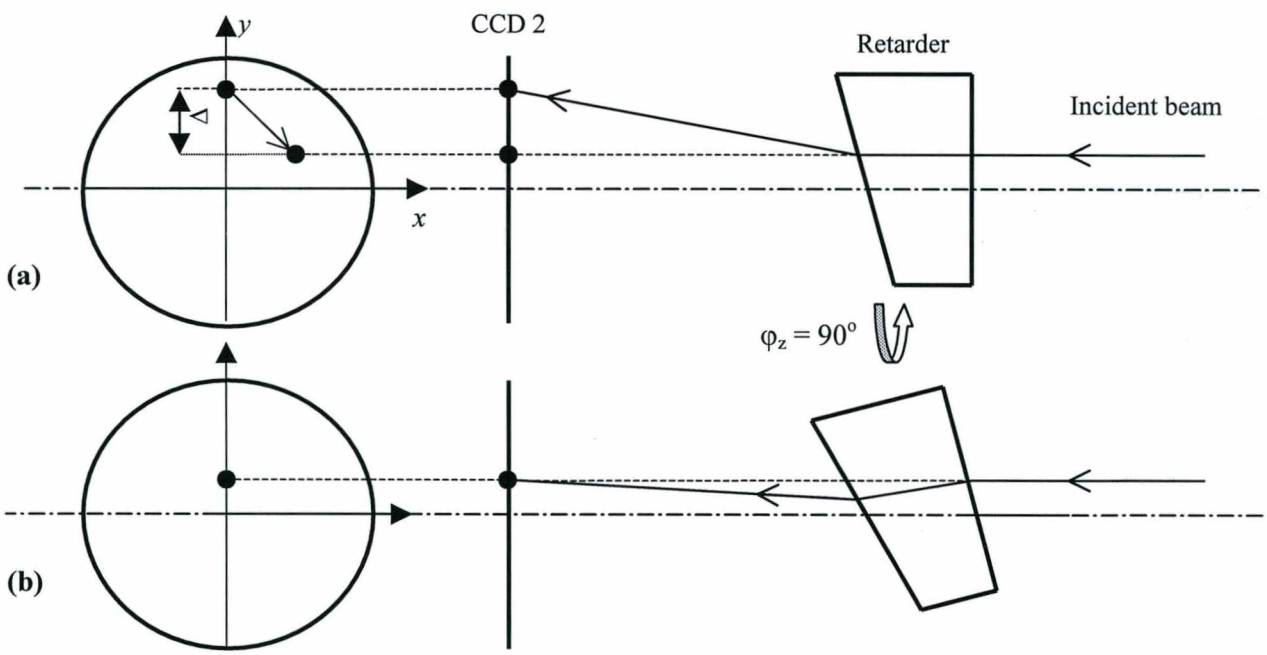

Figure 5.10 (a) Image movement due to rotation of the retarder, (b) Compensation of image movement by tilting the retarder

Usually, the wedge angle does not come aligned with either fast or slow axis. Therefore, in order to compensate an arbitrary wedge orientation, the retarder has to be rotated around both, φ_x and $\varphi_{y,}$.

Compensation can not be achieved for non-parallel rays and wavefront distortion is expected to further degrade correlation of speckles that are situated farther away from φ_z. After alignment, the image movement should not surpass 1/10 of a speckle size to assure sufficient speckle correlation. As a consequence, an alignment resolution of, at least, 1 arc min is needed since expected image movements are of the order of the speckle size.

The retarder was mounted on a rugged φ_z - rotational stage which allowed its alignment in φ_x and φ_y with described resolution. Figure 5.11 shows this rotational stage within the second channel of the interferometer. In addition to that, the retarder could be adjusted in x and y –directions.

Alignment was achieved by judging the correlation of real time correlation fringe maps on the computer screen while the retarder was rotated 90°. The retarder was adjusted until a reasonable good correlation was obtained.

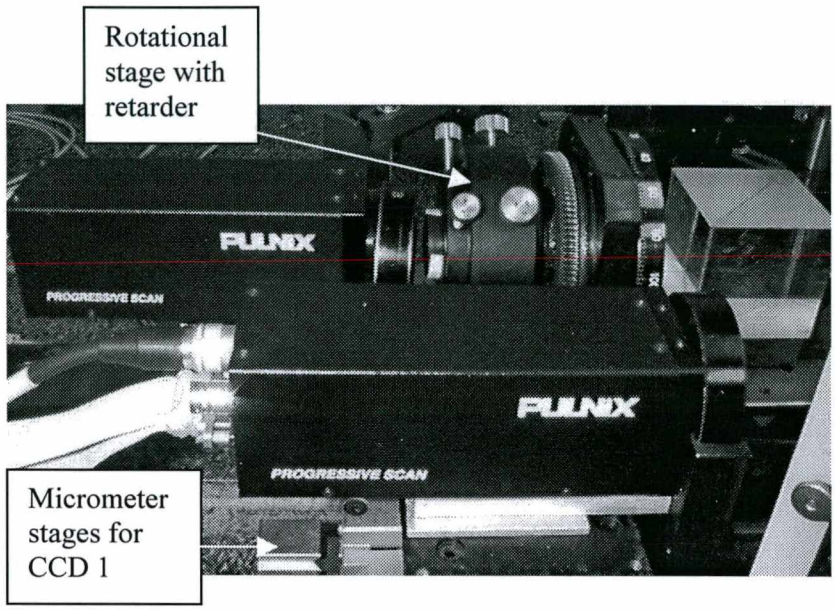

Figure 5.11 View of the two observation channels

5.2.5 The sensor

Two Pulnix TM-9701™ black and white CCD cameras, shown in Figure 5.11 were used as imaging sensor. Their specifications are:

- Imager: 2/3'' progressive scanning CCD
- Pixels: 768 (H) x 484 (V)
- Cell size: 11.6 (H) x 13.6 (V) μm progressive scan
- Imager size: 8.9 (H) x 6.6 (V) mm
- Scanning: 525 lines at 30 Hz
- Video output: analogue: RS-170 composite video or digital: 8 bit RS-422
- *SNR*: 50 dB minimal
- Minimum illumination: 1 lux at $f^{\#} = 1.4$
- Operating temperature: -10 °C to +50 °C
- Dimensions: 44 mm x 48.5 mm x 136 mm

These cameras were chosen because of their special features. They include a full frame shutter adjustable within (1/60 to 1/16000 s), externally controllable and with asynchronous reset capability, as well as a built-in frame memory for asynchronous image capturing.

The full frame shutter is necessary to hold one field of charge with full vertical resolution at each exposure, which is not possible with ordinary interlaced scan cameras. The externally controllable asynchronous shutter is needed to synchronize the exposure of two CCD cameras. Sequential read-out of the images is feasible due to the built-in frame memory, so that a single Matrox PULSAR™ frame grabber can capture the images.

This frame grabber includes a 4:1 multiplexer for analog data but only one digital input. Therefore, a 2:1 multiplexer was built in order to exploit the advantage of digital camera output for the implementation of the proposed algorithm. Figure 5.12 (a) shows the signal plan between the two cameras and the frame grabber and (b) the multiplexer board (see Appendix B).

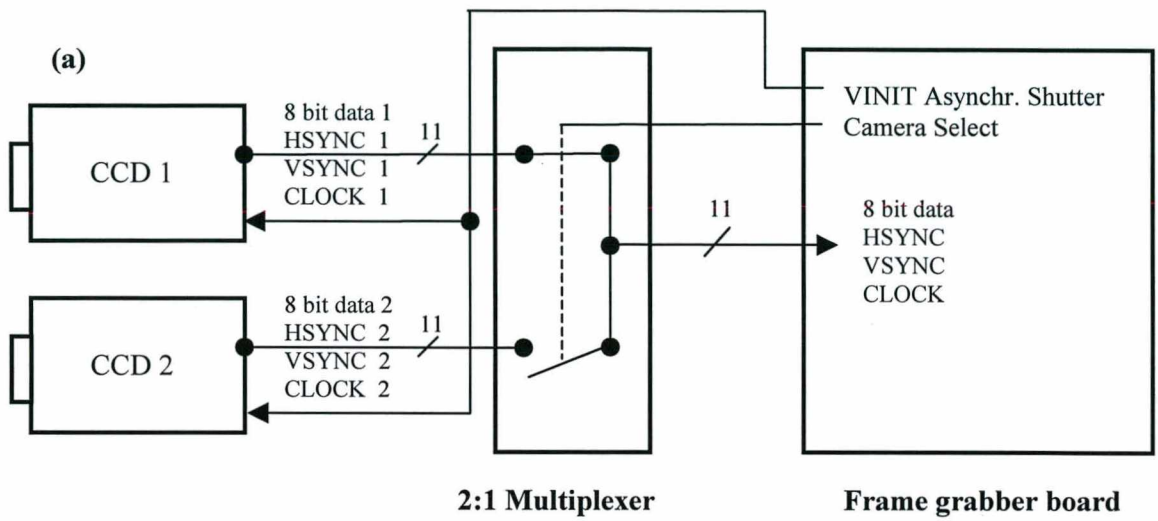

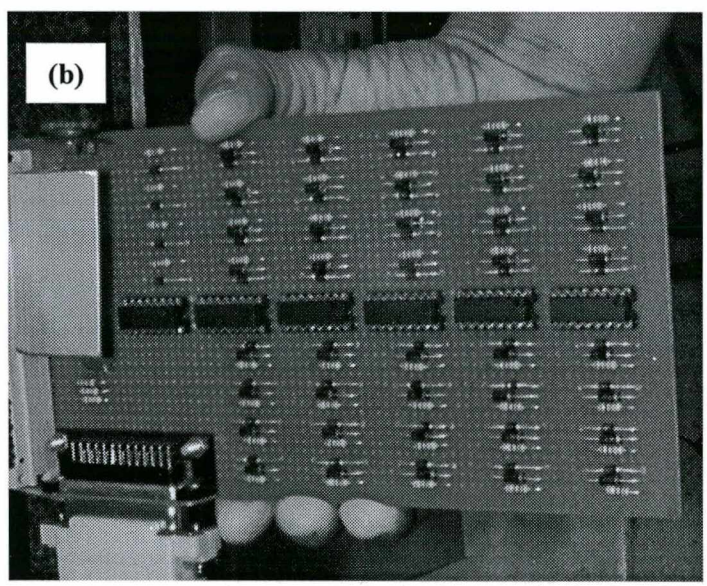

Figure 5.12 (a) Signal plan, (b) Multiplexer

The frame grabber needs 11 lines from each camera (8 data lines and 3 lines for synchronization) in order to be capable to read the images stored in their memory. Further, two user bits of the frame grabber were used for control, one for simultaneous shutter and one for selecting the camera output to be read.

The observed size of speckles was optimized by positioning the two cameras slightly out of focus. This procedure is possible because of image-side telecentrical rays. CCD 1 was aligned with respect to CCD 2 by mounting it on micrometer stages (see also figure 5.11) so that both cameras viewed the same scene. This scene corresponds to about 40 mm x 30 mm on the specimen for the set-up shown in figure 5.1. The optimal intensity ratio was adjusted for each channel independently by rotating polarizers P3 and P4. Polarizers P1...P4 (plate construction equivalent to figure 5.9: ∅ 55 mm x 4 mm) are sheet polarizers with 30 % transmission for unpolarized light and an extinction ratio to unwanted polarizations of 10^{-4}.

5.2.6 The software

A software was developed including several modules that control data acquisition and processing. These are:

- Control of the frame grabber
- Control of the PZT driver
- Data processing

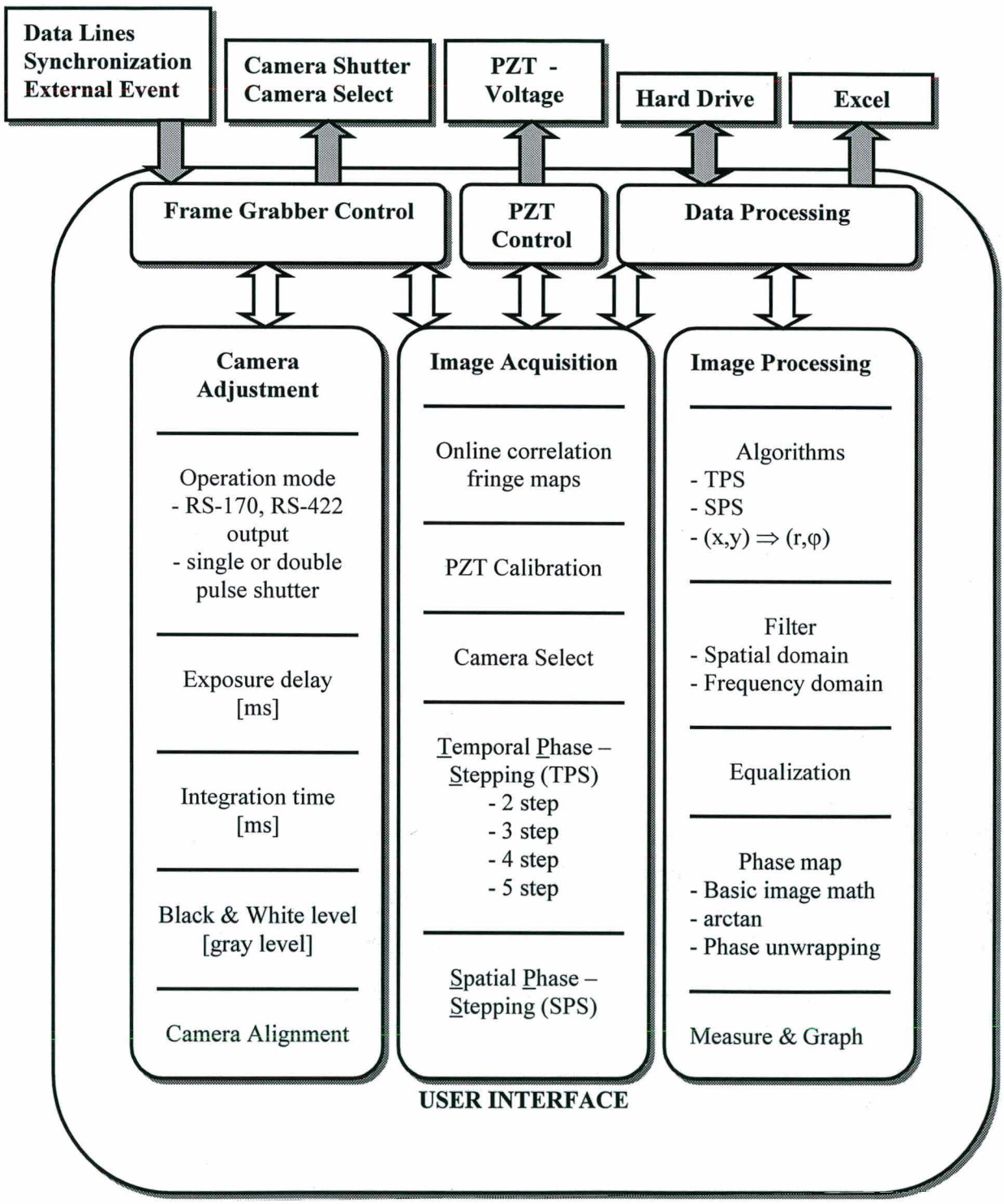

Figure 5.13 Functional blocks of software for control and data processing

Control of the frame grabber board includes camera shutter, camera multiplexer and synchronization between camera, frame grabber and external events for image acquisition. The PZT driver is a controllable voltage source which can be controlled by software via the parallel port of the host computer. Data processing is, basically, done on the host computer offering the possibility to import data or to export it for further processing.

The frame of the software was programmed in VISUAL BASIC™. The frame grabber was controlled using MATROX Imaging Library™. Processing intensive functions that are not included in that library were programmed in C++ and compiled in form of an additional Dynamic Link Library. Figure 5.13 gives an overview of the developed software in form of functional blocks.

Figure 5.14 illustrates the realization of some of the modules cited above.

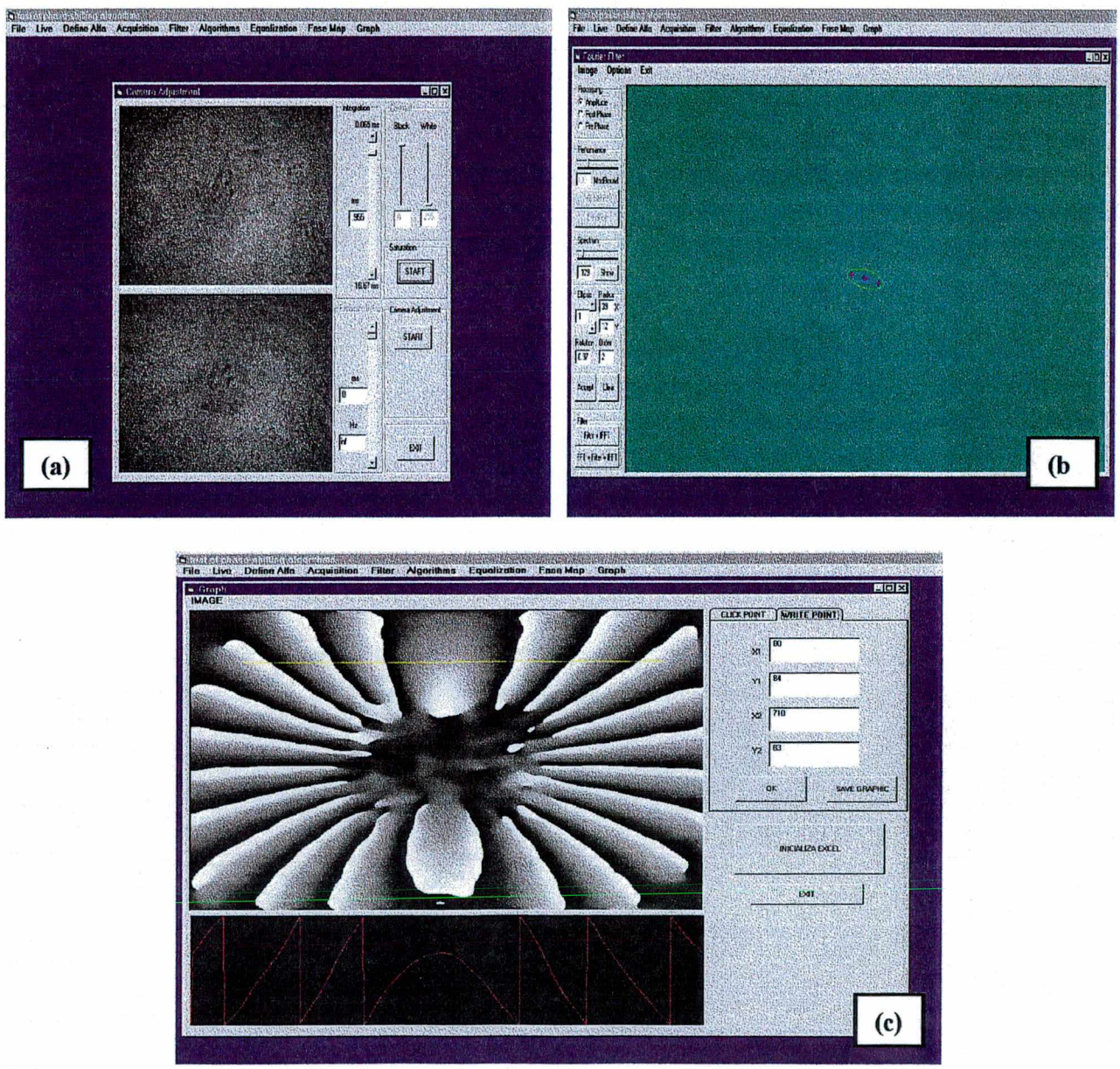

Figure 5.13 Modules for (a) Camera Adjustment (b) Frequency Domain Filter (c) Graphing

6 Experimental evaluation

6.1 Calibration of phase shifter

For proper calculation of the phase change δ the value of phase step due to retardation must be 90°. The retardation uncertainty of the waveplate stated by the manufacturer is expected to be ≤ 0.2 % for the optical setup described in chapter 5. Therefore, phase-step miscalibrations are introduced basically by non-orthogonal polarization between object and reference beam and errors for the position of rotation of the waveplate. These influences have to be minimized by calibration of the phase-shifting device.

Calibration can be accomplished by measuring a view straight carrier fringes that should result in a smooth phase ramp. Figure 6.1 shows a measurement example for the case of a large miscalibration of the phase shifter. An effective phase step of approximately 120° was applied which resulted, as expected, in a negative phase error oscillating at twice the fringe frequency. As expected too, the phase error reached maximum at the phase jumps and in the middle of the fringe. If the phase-step error ε were unknown, its size and sign could be estimated, like illustrated in figure 6.1b.

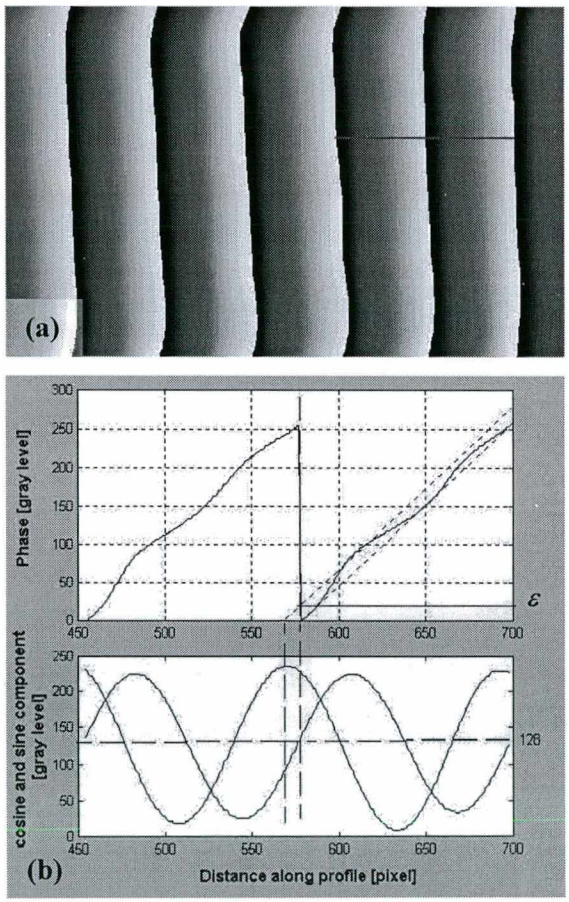

Figure 6.1 Phase measurement with miscalibrated phase-shifter
(a) Position of the phase profile in the phase map,
(b) Estimation of sign and size of the phase-step error from the phase profile

Since the exact orientation of the retarder's fast axis relative to the polarizations of object and reference beam is unknown, calbration is only achieved by an iterative process where it is tried to diminish, step by step, the amplitude of the oscillating phase error. Figure 6.2 shows an advanced state of this process where the phase-step error could already be diminished considerably. However, some residual phase oscillation still remains in the phase map.

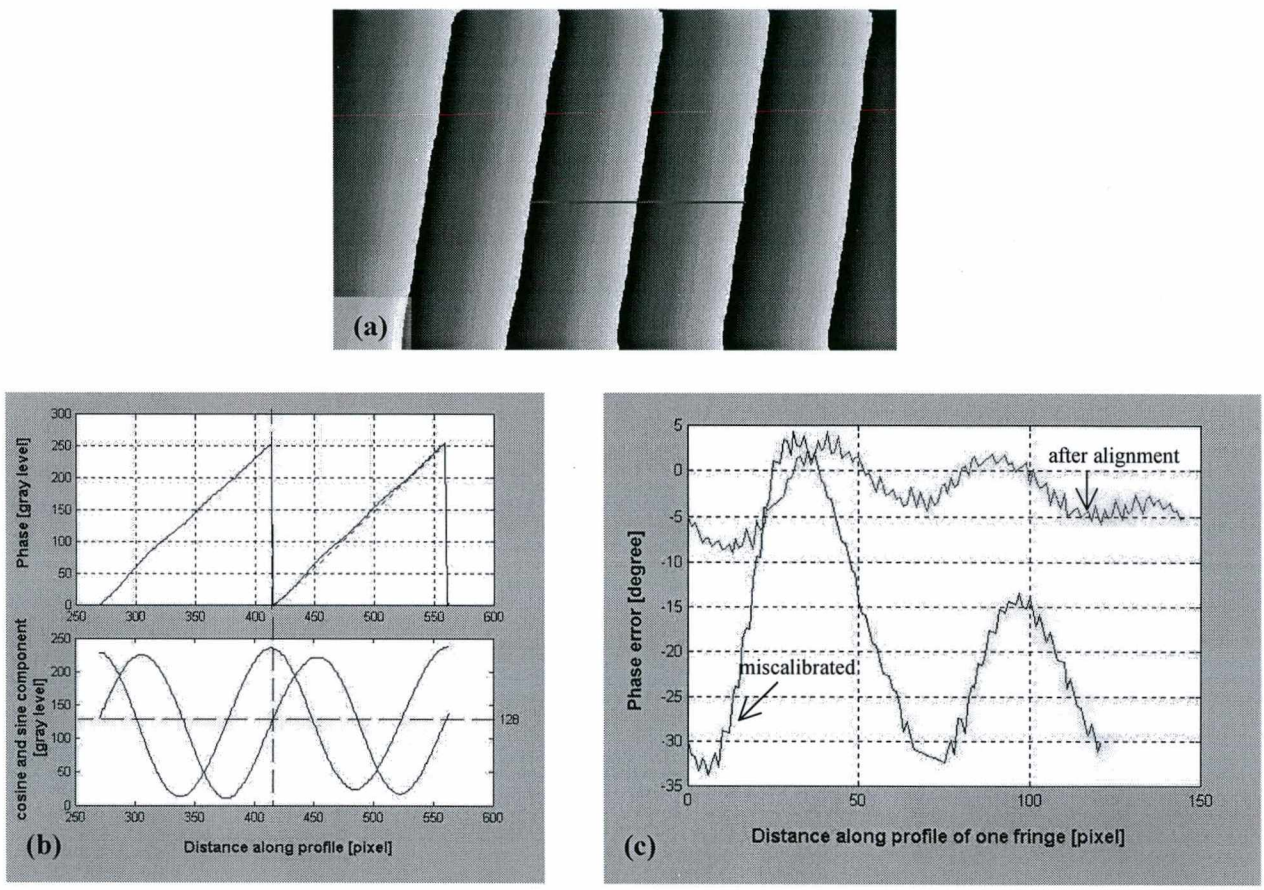

Figure 6.2 Phase measurement after a few iterations of alignment
(a) Position of phase profile in the phase map, (b) Phase profile,
(c) Estimation of sign and size of phase-step error

The mean intensity of each channel is obtained by very fast movement of the reference mirror over several waves during CCD integration time. However, the smaller this integration time the more difficult it is to assure a movement of the mirror, mounted on a PZT, over a sufficient large number of waves. This technique was found applicable for CCD integration times down to 1 ms. For smaller integration times it has been more practical to capture object and reference intensities separately.

6.2 Results for controlled environments

6.2.1 Phase measurement under laboratory condition

The phase measurement uncertainty found by simulation was verified experimentally. An aluminum plate was rotated out-of-plane to generate a linear phase ramp until a fringe density of 1 fringe / 32 pixels was formed. A standard phase ramp like in the simulation is not available in the experiment. However, the linear phase ramp between two sufficiently distant phase jumps (say 20 fringes) can be taken as an approximation for the standard phase ramp.

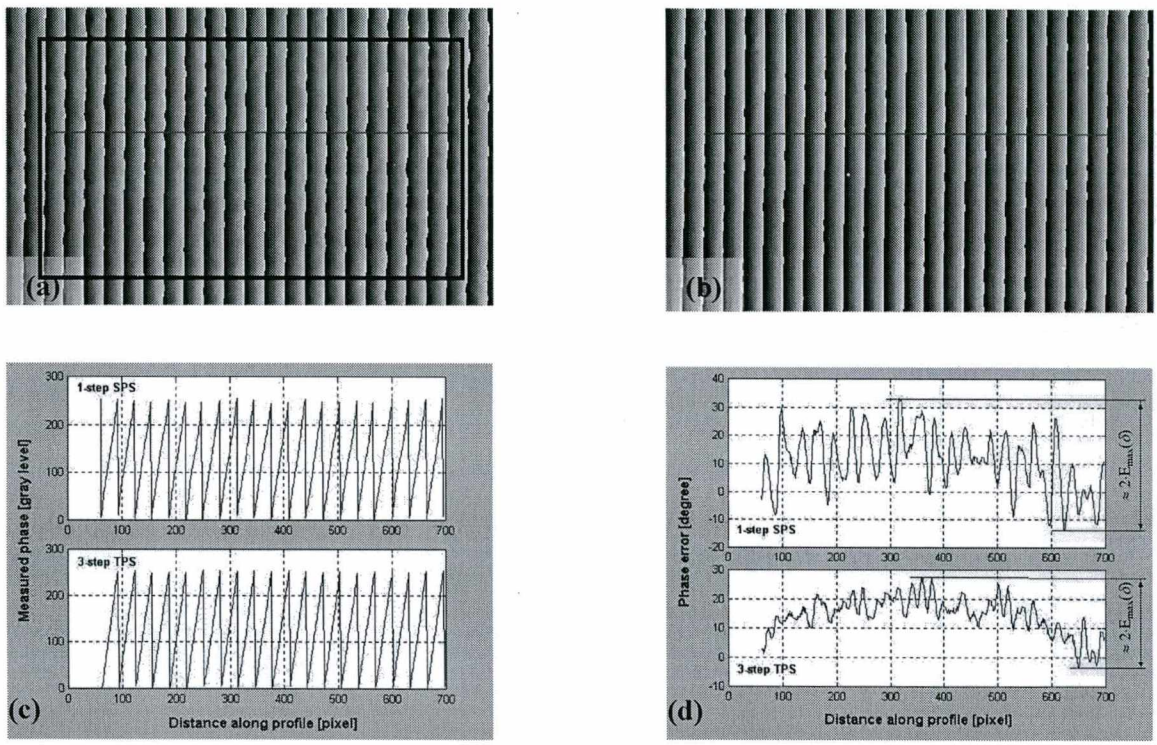

Figure 6.3 Comparison of phase measurement (a) 1-step SPS, (b) 3-step TPS, (b) measured phase profile (c) phase error relative to a linear phase ramp

Under laboratory conditions, the phase was measured with an optical set-up corresponding to that shown in Figure 5.1a. Two phase maps were obtained, one by applying the proposed 1-step Spatial Phase-Shifting algorithm (figure 6.3a) and another using the standard 3-step Temporal Phase-Shifting algorithm. (figure 6.3b). The phase profiles obtained along the dark line are shown in Figure 6.3c. The end points of the phase profile from the standard algorithm were used to generate a linear phase ramp for comparison. The phase difference of the measured profiles relative to this linear phase ramp is plotted in figure 6.3d.

A slight non-linearity in the measured phase can be detected in figure 6.3d. Since both profiles exhibit almost the same tendency, it seems more reasonable to believe that a slightly concave phase ramp was observed instead of an exact linear one. This non-linearity could have been introduced, for example, by the residual sensitivity of the interferometer to in-plane displacements and spherical aberrations of the imaging optics. Therefore, the approximated standard phase ramp serves basically for illustration of the qualitative behavior of the algorithm, but can not be used to quantify the maximum phase error, introduced by each algorithm, as done in the simulation.

Nevertheless, in the absence of a standard phase, one can approximate the maximum phase error caused by the algorithm to half the peak to valley phase difference. The maximum phase errors obtained from the experiment are consistent with those found by the computer simulation.

The measured phase within the dark rectangle in figure 6.3.a was directly compared between the proposed 1-step SPS algorithm and the standard 3-step TPS algorithm. The map of phase difference, obtained by subtraction, is sketched in figure 6.4a in form of a gray level image and in figure 6.4b as a surface plot. Figure 6.4c and 6.4d show its normalized frequency and its cumulative sum from which a maximum phase difference between algorithms was determined for 99.98 % of the image to ± 36°. This value is also consistent with such found by computer simulation.

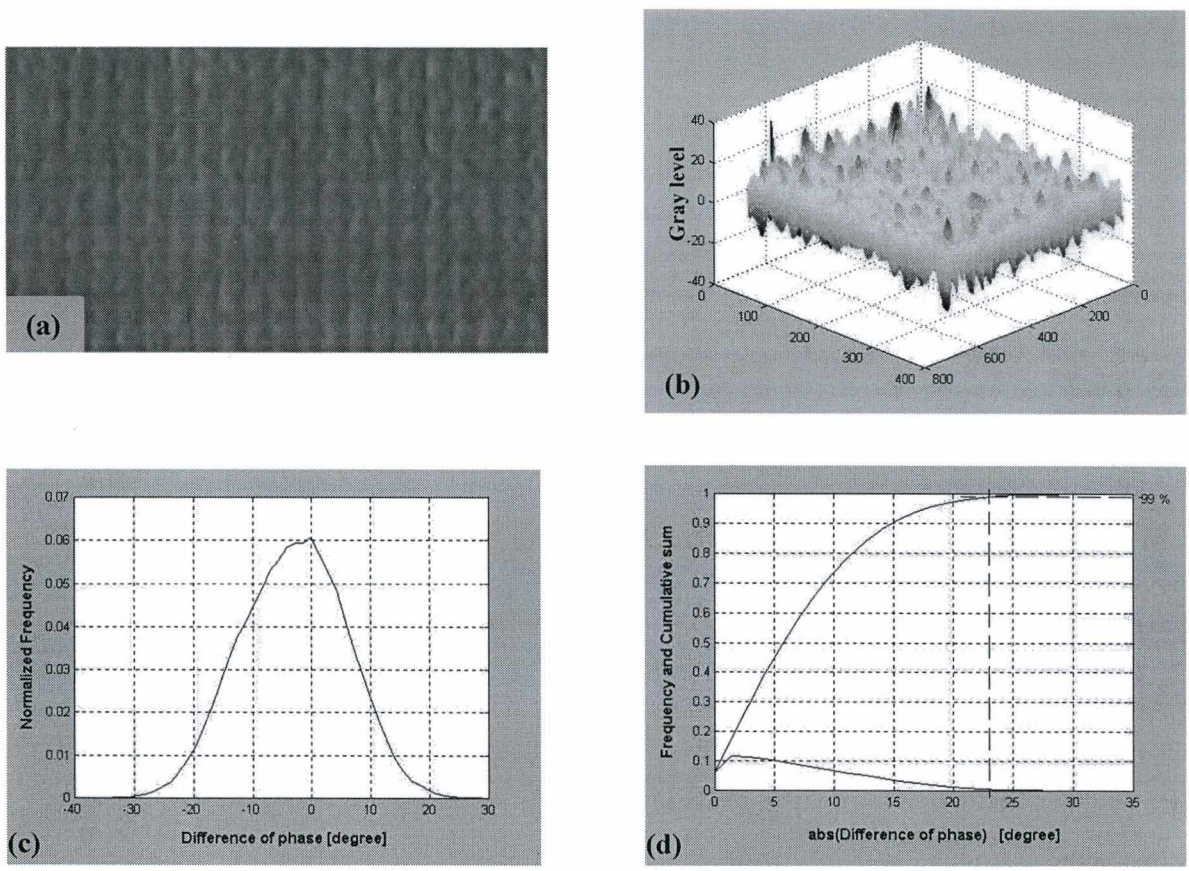

Figure 6.4 Difference of phase detected between the proposed algorithm and the standard algorithm as: (a) gray level image, (b) surface plot, (c) normalized frequency, (d) cumulative sum

6.2.2 Phase measurement in the presence of mechanical vibration

The specimen shown in figure 5.8b was used to simulate phase measurements in the presence of out-of plane mechanical vibration. The light-weight aluminum plate mounted onto a PZT was set into harmonic vibration by modulating the PZT-driver with the output voltage of a HP 8165A programmable signal generator. The entire vibration simulator was calibrated using very low frequency triangle signals from the signal generator. Speckle pattern correlation at video rates was used to count the number of waves introduced as a function of programmed signal voltage. Figure 6.5 shows the peak to valley phase vibration measured as a function of the peak to valley output voltage of the signal generator. The curve exhibits a small non-linearity of the PZT since feedback between PZT and driver had to be turned off.

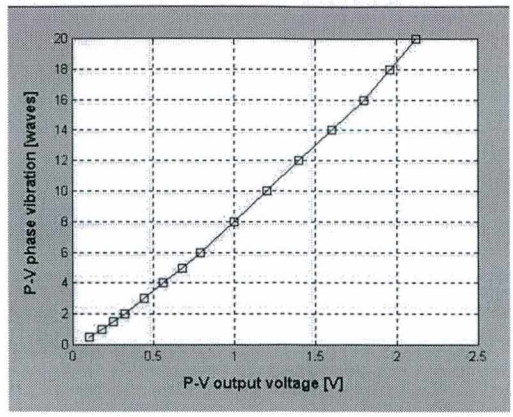

Figure 6.5 Calibration of the specimen vibration: observed P-V phase vibration [waves] versus P-V output voltage [V] of the programmable signal generator

Between deformation states, the plate was rotated slightly out-of plane to generate several fringes over the field of view. A harmonically vibrating plate introduces an additional phase term

$$\Phi_V(t) = \frac{4\pi}{\lambda} \cdot A_V \cdot \sin(2\pi f_V t) \tag{6.1}$$

where A_V is the vibration amplitude and f_V denotes the vibration frequency. The intensity distribution detected by the CCD then becomes a time varying video signal

$$I(t) = I_m + I_m V \cos\left(\Phi + \Phi_V(t)\right) \tag{6.2}.$$

For exposure times much longer than the vibration period $T = 1/f_V$ it has been shown that the resultant time averaging is equivalent to integration over one vibration period which yields [12]

$$I = \frac{1}{T}\int_0^T I(t)\,dt = I_m + I_m V \cdot J_0\left(\frac{4\pi}{\lambda} \cdot A_V\right)\cos(\Phi) \tag{6.3}$$

where J_0 is the zeroth-order Bessel function that modulates the speckle pattern. If $A_V = 0$ then $J_0(0) = 1$ and equation (6.3) is equivalent to equation (2.1). If $A_V \neq 0$ then $J_0(0) < 1$ and the intensity modulation deteriorates until the limit for secure phase measurement is reached.

Maximum vibration amplitudes can be deduced consulting the table of the Bessel function which gives, for example, $J_0(1.0) = 0.765$. In other words, if one considers as such limit a decrease of intensity modulation to 76.5 %, time averaging can be successfully applied in environments where vibration amplitudes do not surpass 1/6 of a fringe, i.e. ≈ 40 nm for a laser wavelength of $\lambda = 514.5$ nm. See also figure 6.6b for illustration. As long as the exposure time is much longer than the vibration period, the maximum allowable vibration amplitude is independent of vibration frequency and serves for comparison of methods.

Measurements in the presence of larger vibration amplitudes become feasible, if the exposure time is reduced to a small fraction of the vibration period $1/f_V$. Then, the amount of phase change introduced during integration can be limited to a fraction of a wave in order to avoid too much loss of intensity modulation due to averaging of intensities (figure 6.6c and d).

Hence, the maximum amplitude of mechanical vibration that still allows secure phase measurement becomes a function of vibration frequency and CCD integration time t_I (figure 6.6a).

How much phase change Φmax may be tolerated during integration is a constant to be determined experimentally. The worst case obviously occurs if the camera is shuttered at maximum vibration velocity. Therefore, the camera was shuttered in the experiment while the output voltage from the signal generator passed through zero.

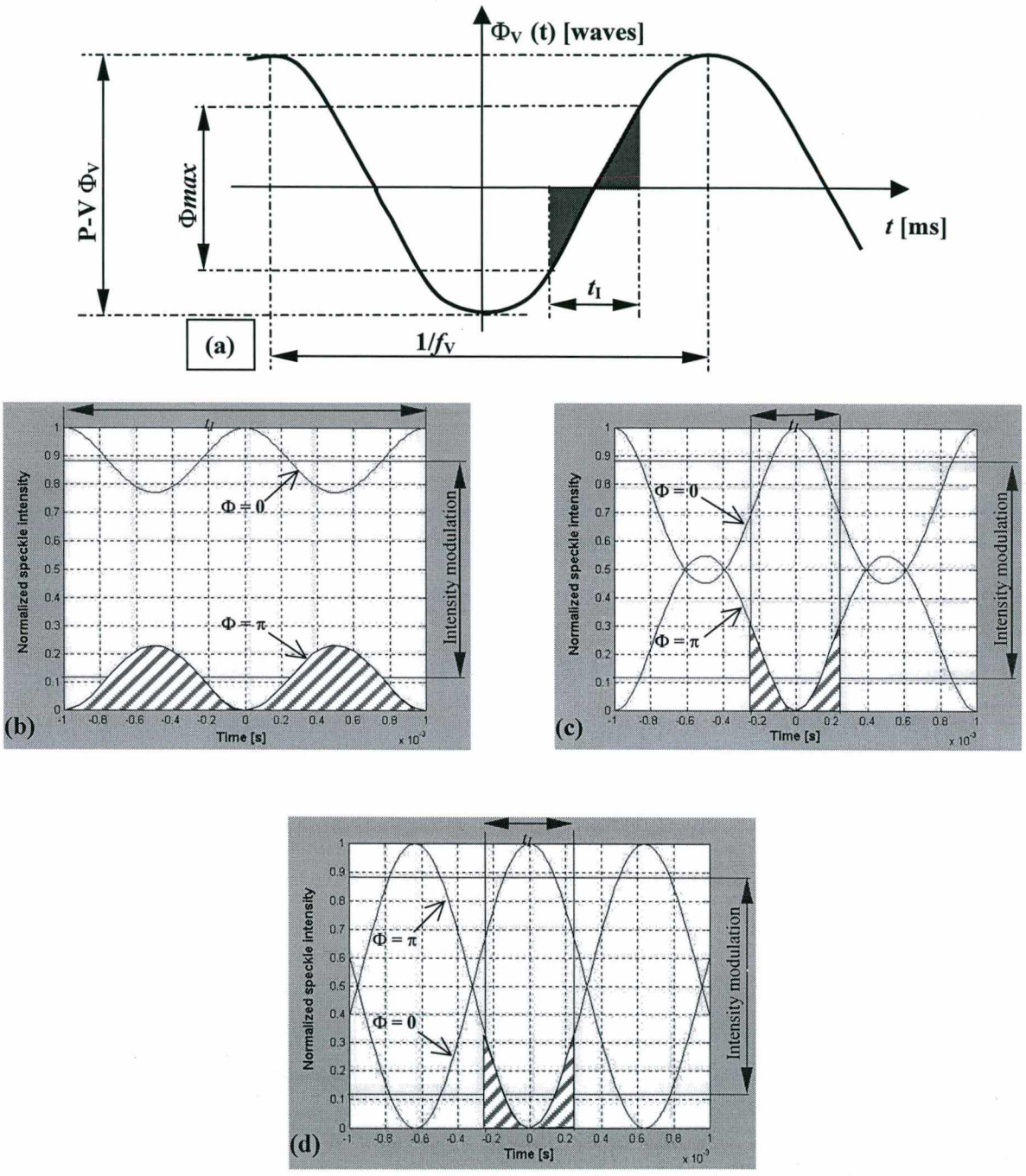

Figure 6.6 (a) Peak to valley phase vibration and instant of camera shutter, (b) Averaging intensity for f_V= 500 Hz, t_I = 2 ms and $\hat{\Phi}_V$ = 0.32 waves, (c) Averaging intensity for f_V= 500 Hz, t_I = 0.5 ms and $\hat{\Phi}_V$ = 0.52 waves, (d) Averaging intensity for f_V= 25 Hz, t_I = 0.5 ms and $\hat{\Phi}_V$ = 10 waves, Φ = 0, π: initial phase of speckle

The necessary synchronization between camera shutter and the signal generator was achieved by using the external event input of the frame grabber board. Figure 6.7 shows the signal plan of the experiment.

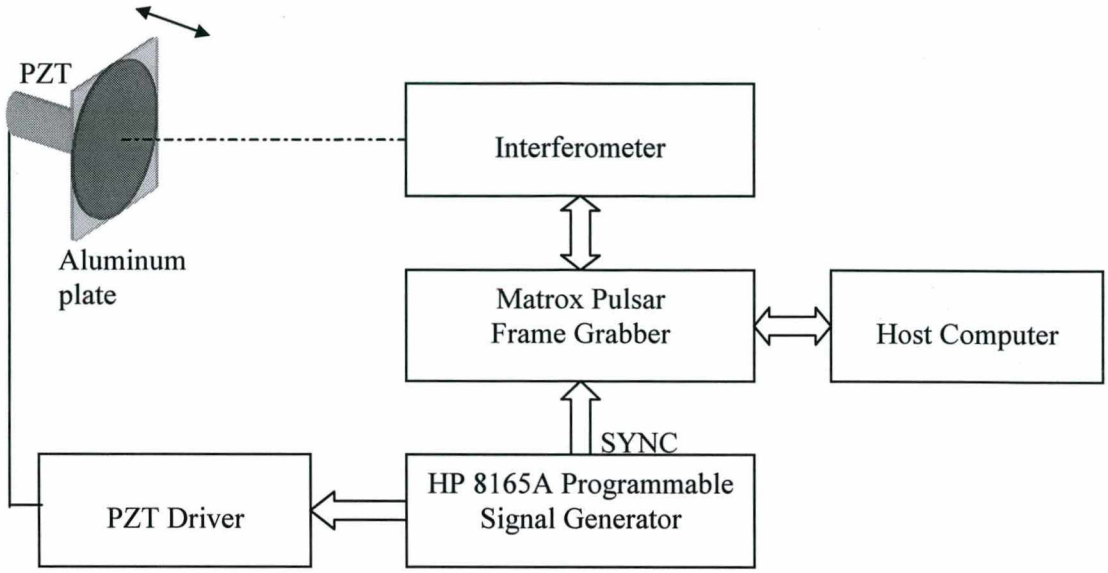

Figure 6.7 Signal plan for testing the interferometer in the presence of vibration

The performance of the interferometer was, first, studied at an integration time of t_I = 0.5 ms and a vibration frequency of f_V = 25 Hz. While increasing step by step the signal voltage of the signal generator, the fringe contrast of correlation fringe patterns was observed at video rates. As soon as the fringe contrast decreased visibly, the signal voltage was read and its corresponding vibration amplitude determined from the calibration curve. Now, with the object vibrating at a constant amplitude, the cameras were shuttered in synchronization with the signal generator. Before and after deformation samples of speckle patterns corresponding to the 1-step SPS and 3-step TPS algorithm were captured at maximum vibration velocity. Between deformation states the plate was rotated out-of plane to form straight fringes of approximately 1 fringe / 32 pixel density. The procedure was repeated for several vibration amplitudes with increments of 0.5 waves.

The phase maps obtained from these samples were analyzed analogous to those without vibration described in 6.2.1. The limit for secure phase measurement was reached when, visibly, additional phase errors started to be introduced due to averaging of intensities over the integration time.
This limit was found at $\hat{\Phi}_V = 10.0 \pm 0.5$ waves, which results in a constant tolerable phase change during exposure of $\Phi max = 0.39 \pm 0.02$ waves.

Theoretically, averaging of intensities in equation (6.2) over t_I = 0.5 ms due to $\Phi max = 0.39 \pm 0.02$ waves (25 Hz) causes the intensity modulation $I_m V$ to drop down to 76.5 ± 2.2 % (see figure 6.6d). This decrease was verified experimentally using the four 90° phase–stepped speckle patterns in the relation

$$I_m V = \frac{1}{2}\sqrt{(I_4 - I_2)^2 + (I_1 - I_3)^2} \qquad (6.4),$$

where the index of the intensity patterns denotes the i-th phase step α_i = 0, π/2, π, 3π/2 like in equation 2.19. At $\hat{\Phi}_V = 10.0$ waves the mean intensity modulation of a speckle pattern was found to decrease from 16.25 to 12.20 gray levels, thus 24.9 % which is consistent with the calculated value.

Since Φmax should be constant, the decrease of intensity modulation served as an efficient parameter to experimentally determine the maximum vibration amplitude for other combinations of vibration frequency and integration time. At each combination the vibration amplitude was increased in steps of 0.1 wave until the mean intensity modulation of the speckle pattern dropped to ≤ 75 % applying equation (6.4). The sample that came closest to 76.5 % indicated the maximum vibration amplitude $\hat{\Phi}_V$. In addition, the feasibility of secure phase measurement was verified for the maximum amplitude found using the proposed 1-step SPS algorithm.

The tolerable phase change during exposure Φmax can also be used to analytically estimate the maximum peak to valley phase vibration $\hat{\Phi}_V$ for several combinations of vibration frequency and integration time using the relation

$$\hat{\Phi}_V = \frac{\Phi max}{\sin(\pi f_V t_I)} \quad , \qquad t_I << \frac{1}{f_V} \tag{6.5}.$$

Equation (6.5) causes significant errors for $f_V \cdot t_I > 0.3$. A more accurate estimate for $\hat{\Phi}_V$ can be obtained using the relation

$$\frac{\frac{1}{t_I}\left\{\int_{-0.5t_I}^{+0.5t_I} I(\hat{\Phi}_V, \Phi = 0, t)\,dt - \int_{-0.5t_I}^{+0.5t_I} I(\hat{\Phi}_V, \Phi = \pi, t)\,dt\right\}}{I(\hat{\Phi}_V = 0, \Phi = 0) - I(\hat{\Phi}_V = 0, \Phi = \pi)} = 0.765 \tag{6.6}$$

where the intensity modulation of an ideal speckle subject to vibration is compared to its modulation without vibration. $\hat{\Phi}_V$ is reached if the intensity modulation of the speckle decreased to 76.5 %. The integrals in equation (6.6) were evaluated numerically within the limits of $-0.5t_I$ and $+0.5t_I$ using an adaptive recursive Simpson's rule.

For comparison the table shown in figure 6.8 includes experimental results obtained using equation (6.4) together with analytical results determined by means of equations (6.5) and (6.6). The experiment used the interferometer configuration shown in figure 5.1b.

f_V [Hz]	**Maximum allowable peak to valley phase vibration $\hat{\Phi}_V$ [waves]**											
	t_I = 0.25 ms			t_I = 0.5 ms			t_I = 1 ms			t_I = 2 ms		
	Eq.6.6	*Eq.6.5*	*Exper.*	*Eq6.6*	*Eq.6.5*	*Exper.*	*Eq.6.6*	*Eq.6.5*	*Exper.*	*Eq.6.6*	*Eq.6.5*	*Exper.*
500	1.015	1.026	0.9	0.531	0.555	0.5	0.318	0.393	0.3	0.318	∞	0.3
400	1.262	1.270	1.2	0.649	0.668	0.6	0.365	0.413	0.3	0.291	0.668	0.3
300	1.676	1.682	1.5	0.851	0.865	0.8	0.454	0.485	0.4	0.296	0.413	0.3
200	2.506	2.509	2.4	1.262	1.270	1.2	0.649	0.668	0.6	0.365	0.413	0.4
100	5.002	5.004	4.7	2.506	2.509	2.4	1.262	1.270	1.2	0.649	0.668	0.6
50	10.000	10.000	9.5	5.002	5.004	4.8	2.506	2.509	2.4	1.261	1.270	1.2
25	19.999	19.996	20.0	10.000	10.000	10.0 (± 0.5)	5.002	5.004	4.9	2.506	2.509	2.5
10	49.995	49.988		24.998	24.995	22.8	12.500	12.499	11.5	6.252	6.253	5.8
5				49.995	49.988		24.998	24.995	24.3	12.500	12.499	12.1

Figure 6.8 Maximum allowable phase vibration as a function of integration time t_I and vibration frequency f_V determined by experiment and equations (6.5) and (6.6)

The table exhibits good accordance between analytical and experimental results. Figure 6.9 illustrates that graphically. It also demonstrates the amplitude range and frequency range where freezing of vibration is to be used, i.e. above the limit for conventional averaging techniques and below speckle decorrelation due to in-plane rigid body motions, from 0 to 800 Hz.
With doubling integration time as a parameter, straight equidistant lines of identical slope are formed on a logarithmic scale. For increasing frequency they become non-linear and converge toward the limit corresponding to integration over one vibration period, i.e. where conventional averaging techniques like equation (6.3) may still be applied.

The shorter the exposure time the higher the frequency at which convergence is reached. Yet, reducing the exposure time needs more laser power for illumination. There are obviously practical limits set by the security standards of vibration allowed on the shop floor. It is clearly not practical trying to freeze higher vibration frequencies than 800 Hz since its vibration amplitude is not allowed to surpass the limit that can be tolerated, with much less effort, by simply averaging intensities over many vibration periods.

An exposure time of t_I = 0.25 ms, which represents the present limit for the set-up shown in figure 5.1b, freezes practically all harmonic vibration above 400 Hz. However, this exposure time is still too long in order to freeze maximum allowed vibration amplitudes at smaller vibration frequencies. As can be concluded from figure 6.9, an exposure time of t_I = 0.1 ms would do the job.

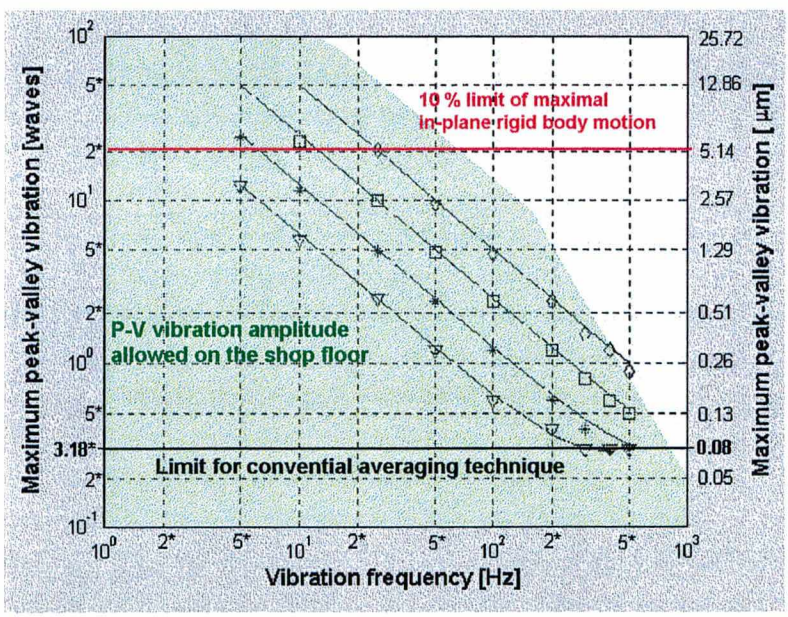

Figure 6.9 Maximum P-V vibration as a function of vibration frequency and CCD integration time (diamonds = 0.25 ms, squares = 0.5 ms, stars = 1 ms, triangles = 2 ms, dashed lines = equation (6.6))

Decorrelation of speckles limits the maximum vibration amplitude that could be, theoretically, frozen at low vibration frequencies. The 10 % limit of acceptable out-of plane and in-plane rigid body motions can be calculated using equations (2.14) and (2.15) respectively, which yield w = 92 µm and u = 5.2 µm.

Transversal vibration of the cylinder relative to the conical mirror introduces out-of plane and in-plane rigid body motions simultaneously. Therefore, in the presence of vibration frequencies below 60 Hz, the maximum vibration amplitude that can still be tolerated for the given set-up during measurement of radial displacements in cylinders is limited by the in-plane rigid body motion. Yet, the fact that transversal motions between the cylinder and the conical mirror introduce additional fringes into the phase map certainly decreases this limit to 5...10 waves (1.3 ...2.6 µm). The occurrence of larger motions need to be avoided by vibration damping and stiff attachment between cylinder and interferometer.

6.3 Measurement application

The feasibility of radial displacement measurements inside cylinders in adverse conditions like found for light manufacturing was investigated by using the interferometer configuration of figure 5.1b without vibration damping. Ground vibrations were allowed to reach the entire interferometer including the specimen cylinder by simply removing the air from the air cushions of the optical bench. Between deformation states a load of approximately 10 N was applied on top of the cylinder. This load caused both, a slight deformation of the cylinder and some portion of rigid body motion between the cylinder and the conical mirror. The measurement example also demonstrates the operation through generic processing blocks of this particular measurement system.

For the purpose of comparison, standard temporal phase-stepping was applied at an integration time of 1/60 s. The obtained phase map is shown in figure 6.10d. Obviously, the phase vibration during exposure was beyond the limit for standard averaging techniques, making measurements impossible. Contrary to that, the proposed interferometer still allowed to capture phase maps with reasonable fringe contrast. With exposure times set to 1 ms, practically all phase vibration was frozen into the phase map. About 200 mW of laser light were needed for sufficient illumination. Figure 6.10a and b show the raw cosine and sine component of the phase that were calculated from the interferograms captured by the two parallel channels. These components were smoothed to yield the wrapped phase map in figure 6.10c.

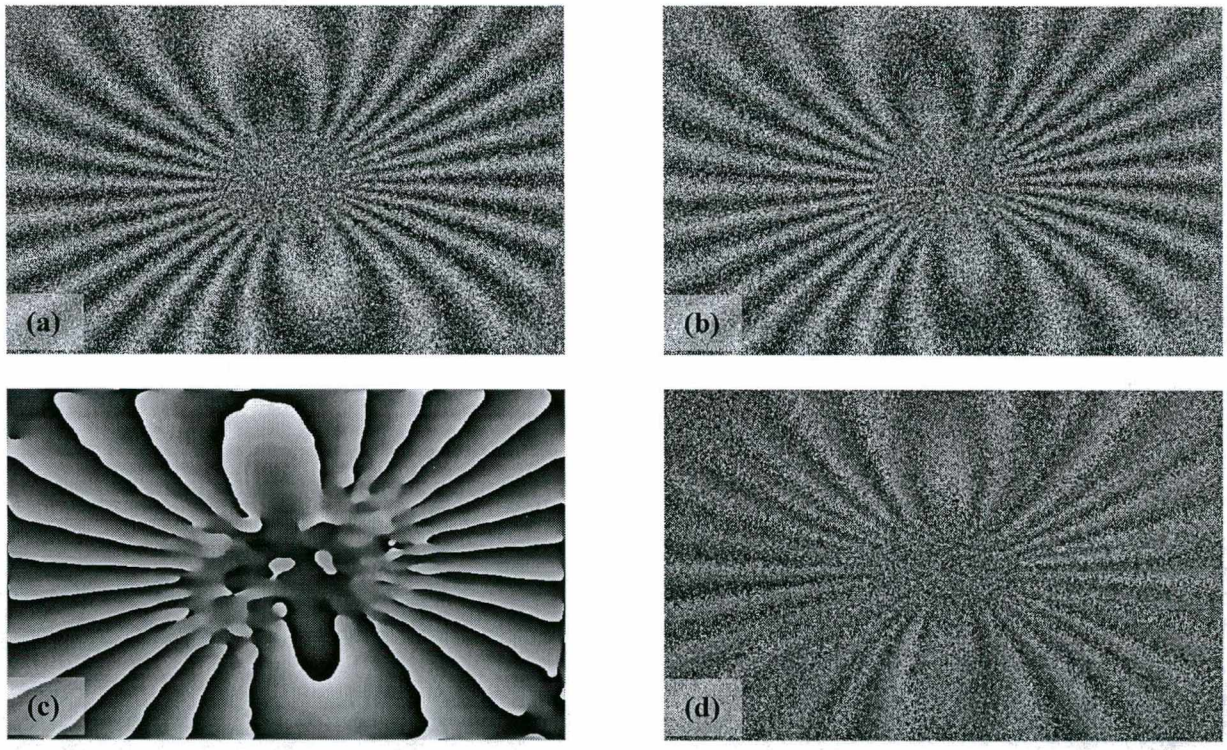

Figure 6.10 Measurement example without vibration damping, (a) channel 1: cosine component, (b) channel 2: sine component (c) phase map obtained from (a) and (b) with 1-step SPS algorithm (d) phase map obtained with 3-step TPS algorithm

Figure 6.11 illustrates the sequence of image processing applied to radial displacement measurements using conical mirrors. For this particular measurement system it is useful to introduce a polar to cartesian transformation [16] of the raw phase components prior to the smoothing process (figure 6.11c,d). Then, in the frequency spectrum the energy of the signal corresponding to rigid body motions (vibrations) is concentrated only in x-direction (figure 6.11e) which makes application of more optimal filter masks possible (figure 6.11f), hence improving the overall filter result (figure 6.11g,h).

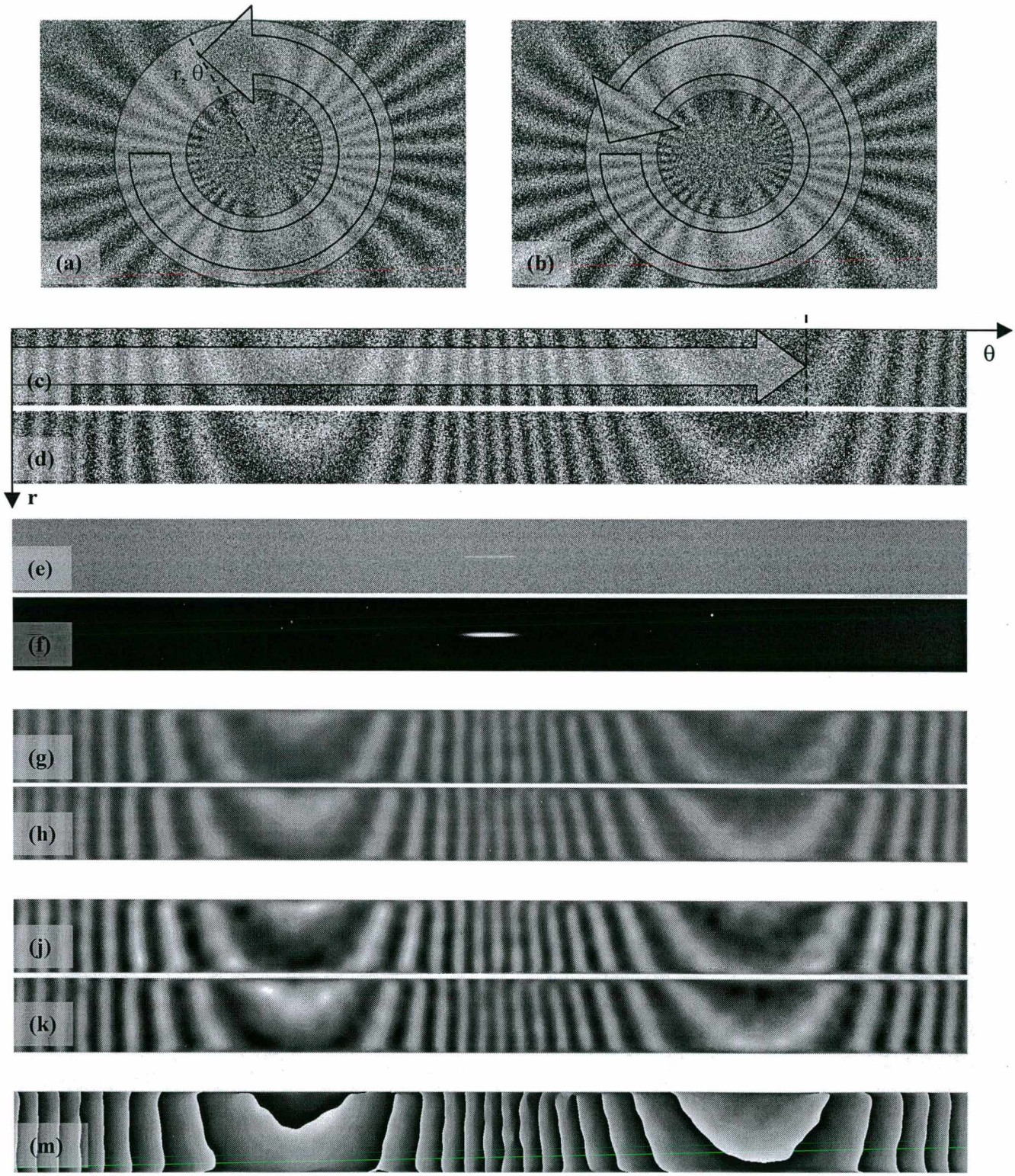

Figure 6.11 Generic blocks of image processing: (a), (b) raw sine and cosine component of phase, (c), (d) polar to cartesian transformation, (e) frequency spectrum, (f) filter mask (Butterworth), (g), (h) low-pass filtered sine and cosine component (j), (k) equalized sine and cosine component, (m) wrapped phase map

Due to decorrelation introduced by rotating the wave plate the modulation obtainable for the sine component is smaller than that of the cosine component. This effect could partly be reduced by equalizing the phase components. The algorithm of equalization looks for the minimum and maximum gray level in each image, sets them to 0 and 255 respectively and linearly scales gray levels which are in between. After equalization the phase components (figure 6.11j,k) are input to the four quadrant inverse tangent function which yields the wrapped phase map (figure 6.11m).

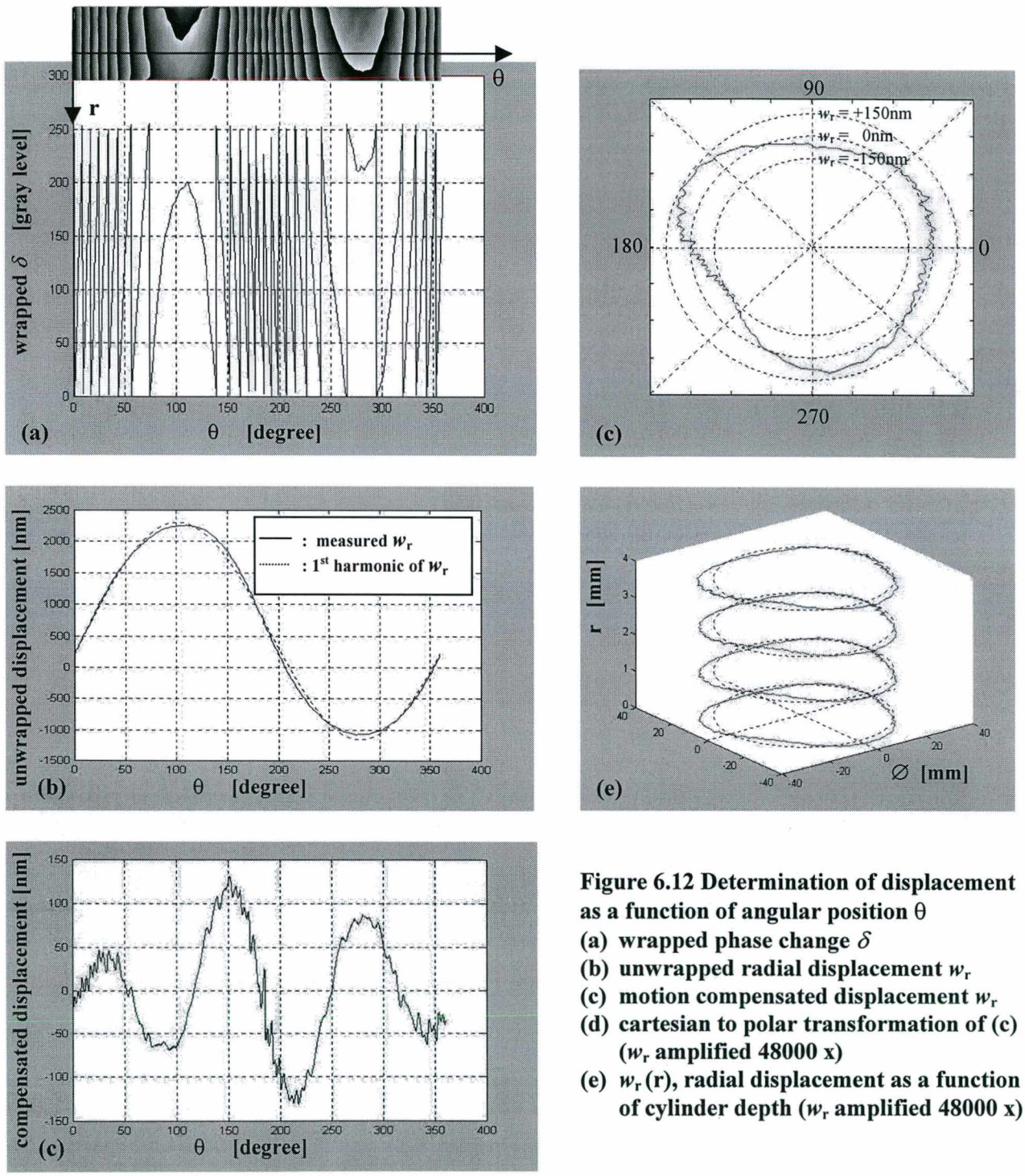

Figure 6.12 Determination of displacement as a function of angular position θ
(a) wrapped phase change δ
(b) unwrapped radial displacement w_r
(c) motion compensated displacement w_r
(d) cartesian to polar transformation of (c) (w_r amplified 48000 x)
(e) w_r (r), radial displacement as a function of cylinder depth (w_r amplified 48000 x)

Now, the radial displacements encoded in the phase map need to be extracted. This was done at several measurement depths r of the cylinder. First, the 2π-phase jumps in the wrapped phase map (figure 6.12a) have to be removed, a process also denominated as phase unwrapping. Figure 6.12b shows the result of that process as a displacement profile.

What really interests is the measure of shape modifications of the inner cylindrical surface. Unfortunately, a large amount of motion between the cylinder and the conical mirror was superposed to the signal of interest. A minor portion of it was introduced during the loading process but the major portion is due to mechanical vibration that was frozen into the phase map. If this motion does not surpass the limits established in the previous section it can be compensated by software [16].

The compensation algorithm exploits the fact that small lateral translations in a circle centered at the origin of a polar coordinate system can be expressed as

$$w_r(r,\theta) = \Delta x(r)\cdot\cos(\theta) + \Delta y(r)\cdot\sin(\theta) \qquad (6.7),$$

where Δx and Δy are the x- and y-components of the lateral translation respectively and w_r is the radial displacement that can be extracted from the phase map at cylinder depth r and polar angle θ .
Equation (6.7) states that small lateral displacements represent the first harmonic of the radial displacement signal, whereas shape changes are expected higher harmonics. Hence, the algorithm has to compute the Fourier coefficients of the first harmonic

$$\Delta x(r) = \int_{0^o}^{360^o} w_r(r,\theta)\cdot\cos(\theta)\,d\theta\,, \qquad \Delta y(r) = \int_{0^o}^{360^o} w_r(r,\theta)\cdot\sin(\theta)\,d\theta \qquad (6.8)$$

as a function of cylinder depth. Constant coefficients along the cylinder depth represent rigid body only translation between the cylinder and the conical mirror. If interconnecting the end points of different rigid body translation vectors allows to form a straight line along the cylinder depth, then, rotation between the cylinder and the conical mirror is present. The slopes of that line in space can be estimated by linear regression, one for the $\Delta x(r)$ and another for the $\Delta y(r)$, representing the amount of rotation in the *xz*- and *yz*-plane respectively.

The dotted line in figure 6.12b represents the dc term + first harmonic that was extracted from the displacement signal w_r. If subtracted from the displacement signal w_r only a small amount of radial displacement remains (figure 6.12c), causing a minor shape modification (figure 6.12d).

Computation of the Fourier coefficients at several rings revealed an additional small rotation in the *yz*-plane ($\approx 25\cdot10^{-6}$ rad). Lateral translation becomes larger the closer one gets to the center of the cone. From this data the pivot was calculated at 70 mm behind the center of the cone which coincides with the mirror fixation. Apparently, the ground vibrations induced the heavy conical mirror to rotate around the mirror fixation behind. Knowing the amount and direction of rigid body motion/rotation, they can be compensated. Figure 6.12e illustrates the resulting shape modification along the cylinder.

6.4 Conclusions/Problems

Based on the measurement results and practical experiences collected with the present interferometer some of its limitations can be named and important conclusions drawn for the construction of a compact and robust interferometer.

(1) Limited laser power:

For measurements of radial displacements in cylinders using ESPI in the laboratory one usually counts on a 20 mW cw-He-Ne laser. Assuming standard exposure times of 1/60 s, that means an energy of about 0.3 mJ for illumination. As was pointed out previously, exposure times around 0.1 ms are needed in order to freeze any harmonic vibration >100 Hz allowed on the shop floor. Thus, about 3 W of laser power would be required to achieve this merit.

The Ar+ laser used does not offer that much power. Nevertheless, it was sufficient to enable satisfactory illumination of cylinders at exposure times down to around 1 ms. In many cases such exposure times proved already short enough to completely freeze mechanical vibrations that prevented measurements with standard temporal phase-shifting techniques. Certainly, the available laser power would have been sufficient for smaller exposure times if, for example, fiber coupling were unnecessary and/or all optical components of the interferometer had been provided with anti-reflection coatings.

The Ar+ laser was used in the experiments due to the unavailability of an obviously more economic pulsed source. Yet, problems that do not depend upon whether the laser is pulsed or cw became already evident.

(2) Intensity instabilities

The most serious problem encountered was heating at the fiber coupler due to the high energy densities involved. Apart from limiting the maximum power transmittable through the fiber it caused observable intensity fluctuations during the loading process, especially at exposure times of < 1 ms. Not very seldom, intensity fluctuations were large enough to make measurements impossible because time constancy of object and reference intensities is one of the key presumptions for the working of ESPI (see also chapter 2).

Certainly the best solution would be to avoid fiber coupling at all by incorporating a rugged pulsed solid state laser into a compact interferometer head. If a fiber is to couple laser light from an external source into the interferometer head, a polarization maintaining single mode fiber with large damage threshold should be chosen.

(3) Decorrelation of speckles

Unfortunately, the retarder plate could not be aligned sufficiently. As a result, the 90° rotation of the retarder added a significant amount of decorrelation to the sine component of the phase which led to a reduction of its modulation m_B after the filter process (see equation (4.6)).

With $m_A \neq m_B$ equation (4.7) causes additional errors that have not been considered yet. The phase measurement error introduced by this modulation unbalance can be described by

$$E(\delta) = \arctan\left[\frac{m_B \cdot \sin(\delta)}{m_A \cdot \cos\delta}\right] - \delta \tag{6.9}$$

Equation (6.9) states that the error oscillates at twice the fringe frequency. If the first derivative of equation (6.9) is set to zero one obtains the phase

$$\delta(E_{\max}) = \arctan\left[\pm\sqrt{\frac{m_A}{m_B}}\right] \pm k \cdot \pi \quad , \quad k = 0,1,2... \tag{6.10}$$

at which maximum phase error is reached. From equation (6.9) and equation (6.10) on can estimate the maximum phase error due to modulation unbalance to

$$E_{\max} = \left|\arctan\left[\frac{m_B}{m_A} \cdot \tan(\delta(E_{\max}))\right] - \delta(E_{\max})\right| = \left|\arctan\sqrt{\frac{m_B}{m_A}} - \arctan\sqrt{\frac{m_A}{m_B}}\right| \tag{6.11}$$

where $E_{\max}$ is the phase error in radians. As a rule of thumb one can estimate the phase error as a linear approximation of (6.11)

$$E_{\max}\,[\text{degree}] \approx 100 \cdot \left(1 - \frac{m_B}{m_A}\right) \Big/ 3 \quad , \quad m_B < m_A \tag{6.12),}$$

causing, in most cases, errors of ≤ 10 % for the estimate. Figure 6.13 shows the maximum phase error as a function of modulation unbalance m_B / m_A.

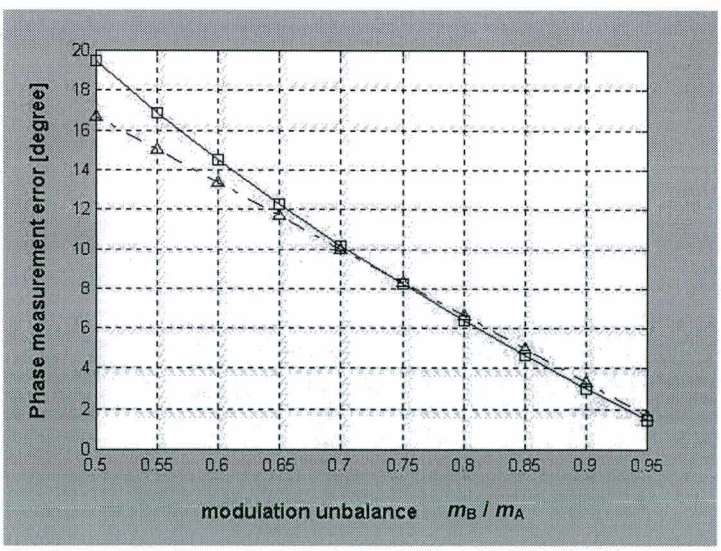

Figure 6.13 Maximum phase error as a function of modulation unbalance m_B / m_A , squares = equation (6.11), triangles = equation(6.12)

With the present interferometer, a modulation unbalance of m_B / m_A = 0.7...0.9 was frequently observed which introduced phase errors of 3...10 degrees. This effect, which is due to rotation of the retarder, can only partly be reduced by equalization of the phase components or more sophisticated image processing.

Therefore, a compact and robust interferometer should avoid such rotation of optical components at all. Like demonstrated, it brings numerous problems, from time consuming alignment to significant increase of phase measurement errors.

(4) Inhomogeneous illumination

The illumination beam that reached the conical mirror was slightly elliptically polarized. Reflection at the metal cone in a plane of incidence that is a function of polar angle θ introduces retardation between p and s component of polarization that is also a function of θ. As a result, after passing through polarizer P2, only an inhomogeneous intensity pattern may be observed.

The inner side of the cylinder could be painted white in order to depolarize the laser light, although this is an unsatisfactory solution because it takes away part of the attractive feature of ESPI which is "non-destructive".

(5) Measurement uncertainty

The performance of the interferometer in stable ambient conditions confirmed measurement uncertainties of ±1/15 wave predicted by the analysis of the proposed algorithm in chapter 4. However, the measurement of radial displacements in adverse conditions introduced additional error sources. These are mainly instability of laser illumination and faster speckle decorrelation due to in-plane motion that happens to be maximum exactly where all the fringes of frozen motion accumulate. The first source is an imperfection of the present interferometer and can be avoided. The latter source is a particularity of radial displacement measurements and can hardly be diminished (even worse for smaller cylinder diameters). Together, they certainly increased the obtainable measurement uncertainty to ±1/10 wave.

(6) Economy of the interferometer

Another problem is the light energy wasted by the present interferometer. Most energy is wasted due to the fiber coupling but also inside the interferometer head several improvements can be made.

For example, in measurements of radial displacements exactly the central part of the beam, which has highest intensity due to the Gaussian beam profile, is cut by the 10 mm hole of the illuminating mirror M3. For these measurements, it would be interesting to concentrate all light energy delivered by the laser into a ring corresponding the size from which confident measurement data can actually be extracted.

(7) Attachment between cylinder and specimen

The present interferometer allowed measurement of radial displacements only in open cylinders due to the mirror fixation from behind. It would be useful to extend the possible applications to blind holes.

7 Concepts of a portable ESPI system

7.1 Alternatives

Considering the conclusions drawn from the experimental evaluation of the present interferometer the following solutions are proposed to overcome its problems in a portable ESPI system

(1) Limited laser power

The cumbersome water cooled cw Ar^+ laser, that served to show the feasibility of the proposed interferometer, should be replaced by a pulsed Nd-YAG laser. There are several branches commercially available which consist of a Q-switched cavity whose output is frequency-doubled (λ=532 nm). They offer output energies > 0.3 mJ with pulse lengths of < 100 ns.

(2) Intensity instability

Then the laser pulse involves power densities of > 3 kW/mm^2. If one considers a very good coupling efficiency of 70 %, almost 1 kW still need to be dissipated. Although specially designed fiber couplers with air spaced optics and polarization maintaining single mode fibers with extremely high damage threshold are commercially available [41], the pulsed solid state laser should be incorporated into the interferometer head. Apart from economizing laser power in the object beam it will certainly avoid problems with intensity instabilities due to heating.

(3) Speckle decorrelation

Speckle decorrelation in the sine component of the phase due to rotation of the retarder plate can be avoided if a voltage controlled liquid crystal variable retarder is applied. It provides convenient retardance tunability without bulky mechanical parts.

The basic construction, illustrated in figure 7.1, is identical to a traditional fixed retarder. Here, the birefringent material, sandwiched between two glass substrates, is a nematic liquid crystal that changes effective birefringence with applied voltage.

Retardance is dependent upon thickness and birefringence. For the liquid crystal, birefringence depends on operating wavelength, drive voltage and temperature. Retardance changes with approximately –0.4 % / C°. Response time is dependent upon the amount and direction of retardance change. A quarter wave retardance (90° phase shift) usually takes a few milliseconds.

The rms-retardance uniformity is about 2 % over the clear aperture which introduces phase-step errors of the same order as were obtainable with an excellent fixed retarder and its inherent alignment problems due to its rotation. Safe operation is limited to 500 W/cm^2 cw or 300 mJ/cm^2 at 10 ns pulse length.

Commercially available systems come along with driver, digital interface and software for computer control [27, 43].

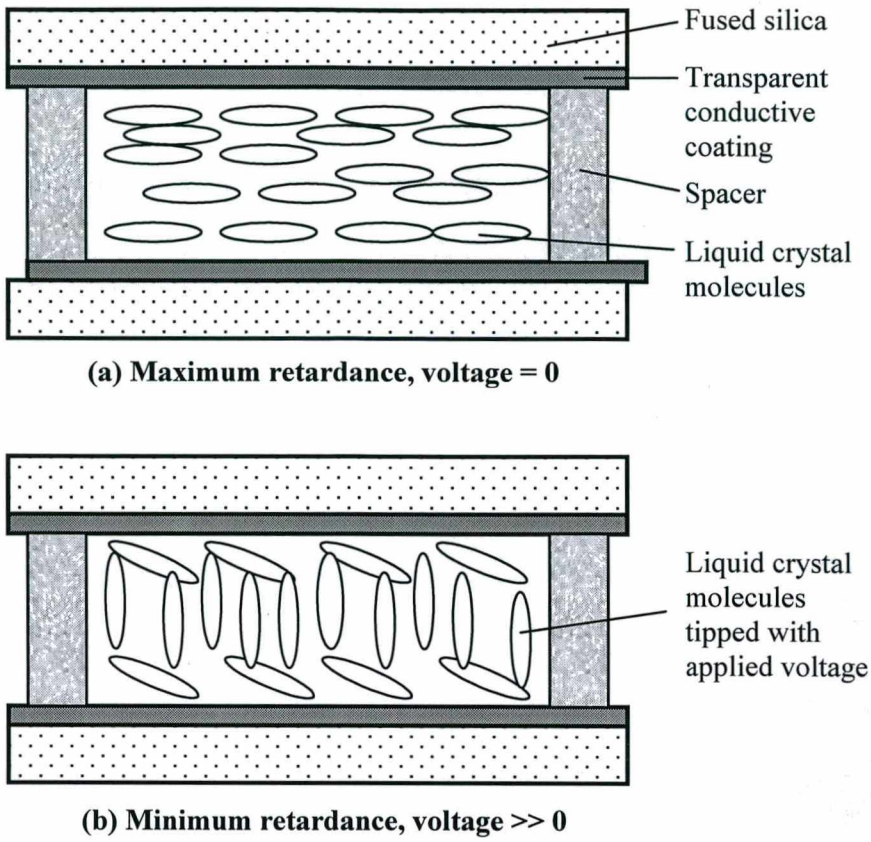

Figure 7.1 Liquid crystal variable retarder construction showing retardance (a) without and (b) with applied voltage

(4) Inhomogeneous illumination

The observation of varying mean intensity from the cylinder due to varying retardation at the metal cone can be avoided by applying a white paint to the inner side of the cylinder. The white paint depolarizes the laser light so that the speckle pattern from the cylinder, selected by polarizer P2 (figure 5.1), exhibits minimum background variation.

(5) Measurement uncertainty

The measurement uncertainty can be improved choosing a pulsed laser whose output power remains stable between consecutive pulses. Small power instabilities can be compensated by scaling the interferograms before and after deformation. Necessary factors could be determined by analyzing the mean intensity of each interferogram which should remain constant for stable output power.

The measurement uncertainty could also be improved if each channel would capture multiple interferograms of the same deformation state, instead of only a single one. For each pair of simultaneously captured interferograms a measurement result is calculated. The final result represents the average of the individual results.

(6) Economy and compactness of the interferometer

The prototype interferometer so far is very bulky and heavy. For a portable ESPI system, size and weight need to be reduced by utilizing robust but small and light-weight optical-mechanical components.

The size and weight of many optical components can be greatly reduced since the clear aperture needed for observation is only ∅ = 10 mm. All optical components that transmit light should be provided with at least a single layer anti-reflection coating to minimize overall reflection losses.

For illumination of inner cylindrical surfaces, laser power can be concentrated into a collimated ring of light by special refractive optics. One possibility is to use two conjugate conical lenses. Figure 7.2 illustrates the basic design and operation of this device.

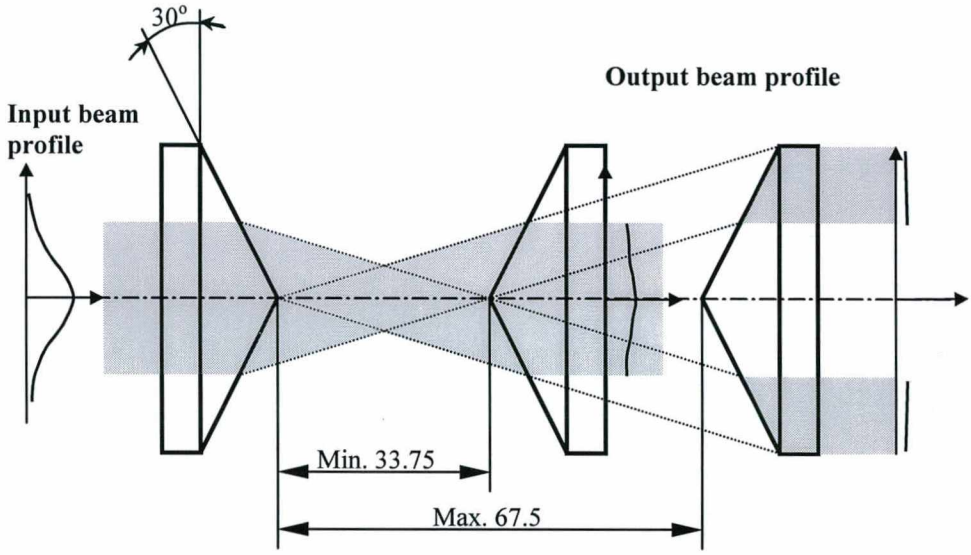

Figure 7.2 Generation of a collimated light ring of homogeneous intensity from collimated Gaussian beam input, material: acrylic (refraction index n = 1.491)

Conjugate conical lenses (∅ = 50 mm) have been fabricated from acrylic for test purposes. The plastic material was chosen because it is cheap and can be easily machined and polished. Further, it has good and stable transmission. Optical surfaces can be even anti-reflection coated by chemical vapor deposition (CVD). For the test, the optical surfaces were diamond turned and polished until sufficient surface finish was obtained.

Due to larger form errors at the center of the cone, some portion of incoming laser light was scattered. Usually, this scattered light does not reach the conical mirror. Tight form tolerances are not required since small form errors of the conical lenses do not introduce significant changes to the radial direction of the system's sensitivity vector and, thus, do not significantly influence the performance of the interferometer.

Experimental evaluation confirmed theoretical arguments that this device, apart from economizing precious laser power, flattens significantly the Gaussian beam profile of a laser beam and, thus, provides more homogeneous illumination of that cylinder region at which radial displacement measurements are feasible.

Some simplifications of the optical setup can be made which decrease the number of optical components and turn the interferometer more compact, robust and economic.

A beam splitting Glan-Thompson polarizer may be applied that combines the function of polarizers P1, P2 and beam splitter BS2, thus, minimizing reflection losses. Its operation is illustrated in figure 7.3. Compared to the beam combiner in figure 5.1 the transmittance is greatly increased making better use of laser power.

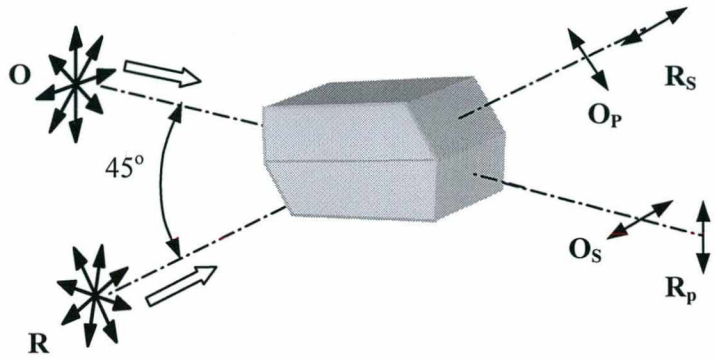

Figure 7.3 Double beam splitting Glan-Thompson prism polarizer p-polarization and s-polarization of reference beam (R) and object beam (O)

A depolarized object beam is obtained by the white paint, whereas the reference beam contains sufficient large p- and s-components of polarization as it experiences several reflections (at least one metal surface introducing > 20° retardation). The p-components are reflected while s-components are transmitted, obtaining excellent extinction ratios of $2 \cdot 10^{-5}$. The polarizations are inherently perpendicular so that alignment of polarizers is no longer required. The angular polarized field is 15° – 17° which is more than necessary for the present application containing telecentric rays.

P3 and P4 are high transmission sheet polarizers (42% transmittance) to control the intensity ratio for each channel.

(7) Attachment between cylinder and specimen

In order to allow measurements in blind holes, total internal reflection at an substrate-air interface could be used. Figure 7.4 illustrates the basic idea. Second reflections from the plane front surface and the circumference do not pass through the 10 mm hole of mirror M3.

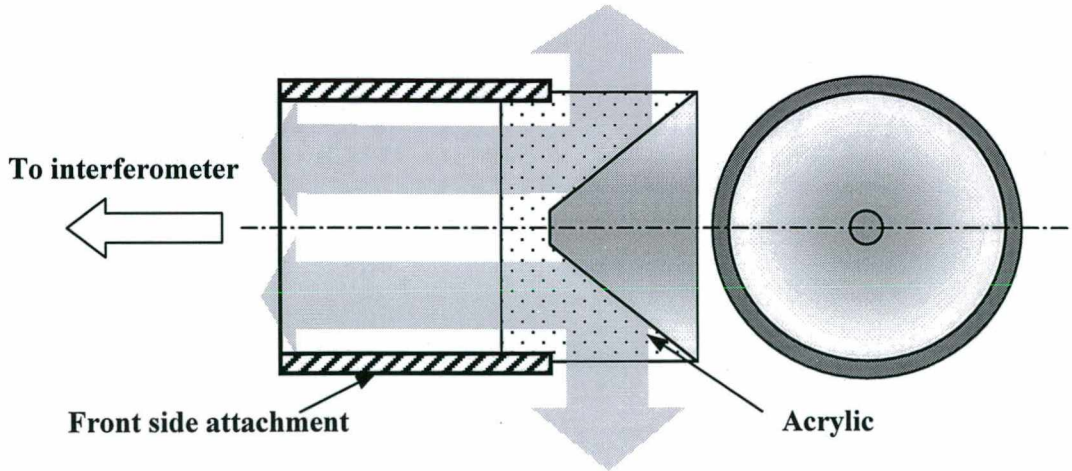

Figure 7.4 Conical mirror using total internal reflection for radial illumination and observation

7.2 Functional Project

Optical components that were mentioned above could not be acquired which is the reason why a portable prototype has not been realized yet. Figure 7.4 shows the functional plan of a portable interferometer for measurements of radial displacements in inner cylindrical surfaces.

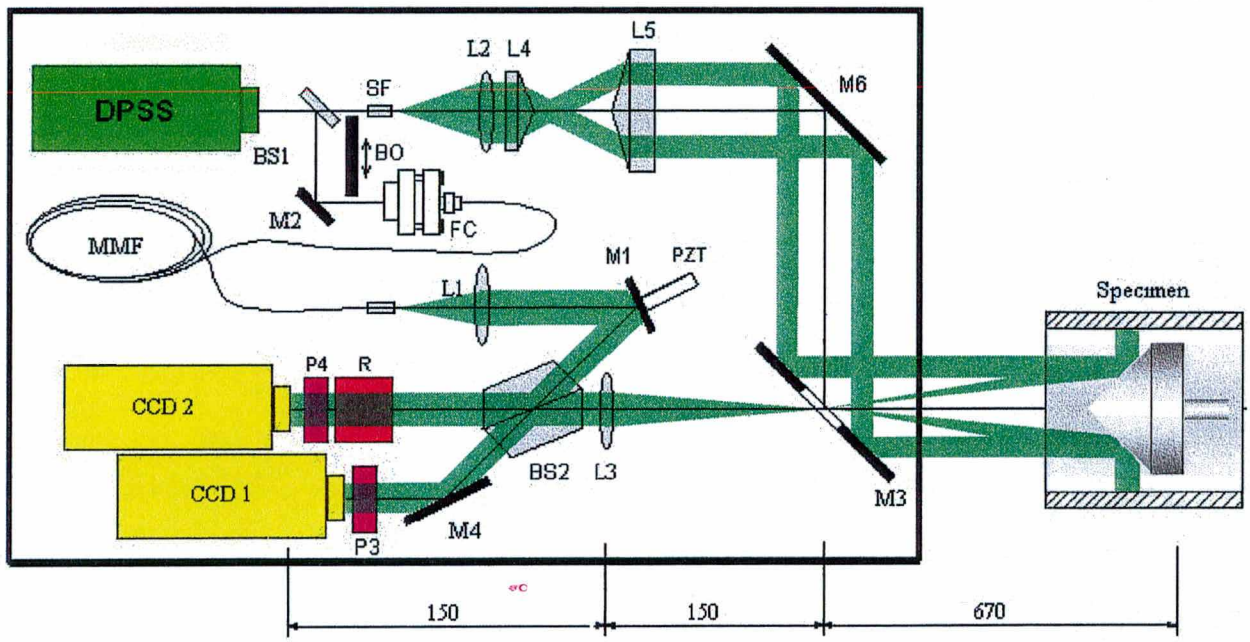

Figure 7.4 Compact interferometer for measurements of radial displacements; BS: beam splitter, DPSS: diode pumped solid state laser, BO: beam obstructer, SF: spatial filter, M: mirror, L: lens, FC: fiber coupler, MMF: mono mode fiber, CM: conical mirror, R: liquid crystal variable retarder, P: sheet polarizer

It uses the same principle as the interferometer shown in figure 5.1b, although it incorporates several improvements. The most important improvement is the Q-switched laser offering sufficient energy in pulse lengths of typically 10...100 ns to freeze any mechanical vibrations. However, the pulsed laser is far from perfect. Its temporal coherence is significantly reduced compared to a cw Ar+ laser. Therefore, by means of a robust fiber coupler (FC) the reference beam is coupled into a mono mode fiber (MMF) to assure a simple setup, equal length of interferometer legs and, hence, optimal fringe contrast.

The fiber, together with the metal reflection at mirror M1, has to produce nearly circular polarized light at the input of the beam splitting Glan-Thompson prism polarizer. Necessary phase retardation is obtained by "coiling" the fiber which introduces stress on it and, therefore, produces birefringence due to the photoelastic effect.

The amount of birefringence is inversely proportional to the radius squared of the fiber coil [51]. Adjusting the radius of the coil and the number of turns, any desired fiber wave plate can be created, which greatly reduces alignment and cost. In addition to that, the mono mode fiber acts as a spatial filter. A smooth reference beam is produced by lens L1. A PZT attached to mirror M1 also allows measurements by temporal phase-shifting.

The high energy object beam is spatially filtered and collimated by lens L2. Then the beam is enlarged to a ring of homogeneous intensity by means of the conical lenses L4 and L5. Control of ring size is achieved by moving lens L5 relative to L4. Tolerances for alignment and movement of L4 and L5 are very tight. Therefore, they are mounted in a precision tubular construction.

As for the prototype already evaluated, the object beam is directed toward the conical mirror CM by mirror M3, obtaining both: radial illumination and observation simultaneously. Its 10 mm hole positioned at the front focal point of lens L2 (f = 150 mm) defines the entrance pupil and, therefore, the size of the speckles ($f^{\#} = 15$).

The object beam forms image sided telecentric rays. The symmetrical cones of light exhibit half angles $\leq 2^{\circ}$. For security, polarizing optical components were specified tolerating even larger angle of view.

In order to achieve a concise unit which is mechanically robust, the number of moving components is reduced to a minimum. Most of them are found in the imaging system. After alignment, movable components need to be locked.

For example, the two cameras are mounted on a guide rail to be translated along the optical axis for focus. Then, the guidance is locked and the polarizers are rotated as close as possible to the CCD for selection of intensity ratio between object and reference beam. However, small rotations of the polarizer cause small image movements due to the wedge form of the polarizer. For that reason, mirror M4 is configured as alignment mirror that allows beam steering around x- and y-axes ($\pm 5^{\circ}$) in order to guarantee that both channels view the same scene before measurements are initiated.

Due to the very short laser pulses, the mean intensity of the speckle pattern has to be calculated from the individual intensity patterns of the object and reference beam. This can be achieved by sequentially obstructing, by means of BO, one of the beams during exposure.

8 Conclusions

A new robust interferometer for radial displacement measurements has been developed. The new ESPI system makes it feasible to investigate radial displacement fields of cylindrical surfaces in adverse ambient conditions like typically found for light manufacturing, which represents a contribution to the field of possible applications with ESPI.

The principal error sources, encountered by the ESPI system on the shop floor, are temperature turbulence and mechanical vibration. The proposed interferometer uses thermal shields against air flow and fast image acquisition to freeze mechanical vibrations into the phase map. The measurement signal due to vibration is compensated by dedicated software algorithms.

The proposed ESPI system is based on a new phase-stepping algorithm, especially designed for spatial phase-stepping ESPI, analyzed in chapter 4. Its practical implementation resulted in an alternative interferometer detailed in chapter 5, whose performance was experimentally evaluated in chapter 6.

8.1 Advantages

Measurement of radial displacements require high spatial resolution of the phase map due to additional fringes introduced by rigid body motions. Therefore, the proposed robust ESPI system freezes mechanical vibrations by means of spatial phase-stepping that preserves the spatial resolution of temporal phase-stepping and, thus, the system's measurement range.

Spatial phase-stepping by polarization control was simplified by application of only a single phase step and two parallel channels to grab necessary information simultaneously. Further, correlation of speckles between channels is no longer needed, relaxing greatly stringent alignment requirements of existent setups. These modifications were primarily introduced to obtain a simpler, cheaper, more compact and robust design that makes measurements in industrial environments a real possibility. The tested interferometer, made up of standard quality optical components, proved to work without vibration isolation, obtaining satisfactory measurement results where standard temporal phase-shifting ESPI fails.

The solutions found for the proposed interferometer are applicable to out-of plane sensitive ESPI systems in general, although the advantages that can be achieved compared to other solutions depend upon the particular measurement problem. For example, the proposed interferometer can easily be adapted to measure radial displacements of outside cylindrical surfaces in adverse conditions.

8.2 Limitations

The entrance pupil of ∅ > 10 mm at the illuminating mirror defines the minimum diameter of the cylinder that can be illuminated. In addition, a sufficient amplification is necessary to resolve phase fringes with rapidly increasing density toward the center of the cone. Therefore, measurable specimen size is limited to cylinder diameters ∅ > 15 mm using the tested interferometer. For investigation of smaller cylinders the amplification of the imaging system has to be increased. This can easily be achieved by collecting lenses of shorter focus length which, in turn, allow smaller hole diameters on the illuminating mirror.

However, with increasing amplification the tolerable limit of in-plane motion between conical mirror and cylinder is diminished. It should be remembered that mechanical vibration between the cylinder and the conical mirror introduces an in-plane and out-of plane component of displacement simultaneously as a function of polar angle. Optical amplification of the tested interferometer was configured such that the limit of in-plane component is well above tolerable fringe density generated by the out-of plane component of vibration. Therefore, maximum vibration amplitude that can be frozen into the phase map and minimum observable cylinder size constitute conflicting parameters that have to be compromised.

Optical amplification also limits the minimum size of the interferometer including the specimen cylinder. Following arguments above, if one considers maximum amplification $\beta = 1$, the 10 % limit of in-plane motion reduces the maximum tolerable vibration amplitude to u = 0.8 µm. Considering further the effective measurement region to make up 2/3 of the CCD target (2.2....6.6 mm) and $f^{\#} = 15$, the focal length of the collecting lens could be, theoretically, reduced to about 33 mm which results in a minimum path length of 132 mm between cylinder surface and CCD target.

In practice, however, already 100 mm of optical path length are necessary to accommodate only optical components of channel 2. Therefore, merely imaging lenses of f ≥ 50 mm are applicable.
With a fixed focal length f = 150 mm the dimensions of the tested interferometer head were about 500 x 400 x 200 mm which were reduced to about 500 x 200 x 100 mm for a compact version.

The maximum measurement error for the tested interferometer was found ±1/10 wave which results in approximately ±26 nm displacement. Although this maximum measurement error is well above those obtainable with standard techniques in controlled environments and 50 % higher than the measurement error confirmed as being possible with the proposed algorithm, the achieved results can be considered satisfactory.

The measurement uncertainty for a single measurement can be reduced until about 1/15 wave. Further improvement can be obtained through averaging of several measurements.

The capability to freeze into phase maps practically any mechanical vibration allowed on the shop floor is achieved at exposure times around 0.1 ms. Yet, since the motion due to vibration has to be compensated, the fringes they add to the phase map need to be resolved and quantified with security. That is why, in practice, the maximum vibration amplitude is limited to half the maximum motion that can be extracted with security from the phase map. This limit is reached with the proposed ESPI system at frequencies ≤ 100 Hz and vibration amplitudes ≥ 1.3 µm.

8.3 Recommendations

(1) Construction of the compact prototype interferometer

In order to increase the versatility of the proposed measurement system, one could provide the possibility to the user to change between several combinations of lenses and illumination mirrors. For example, if smaller sized cylinders are investigated, the focal length of the imaging lens and the hole diameter of the illumination mirror are decreased proportionally until the practical limit of focal length f = 50 mm and aperture $D = 3$ mm are reached.

For decreasing focal length the whole imaging optic, including the proper imaging lens and the two parallel channels with reference collimation, need to be translated closer toward the illuminating mirror. As the reference is guided along a fiber, this can be achieved with relative ease. However, prior to implementation the performance of the interferometer at smaller focal lengths needs to be analyzed experimentally.

(2) Performance

In order to increase the performance and, principally, minimize the measurement uncertainty obtainable with this measurement system it is suggested to:

- use lasers with stable intensity between consecutive pulses to avoid phase errors in the algorithm
- use of precision polarizers with high extinction ratio to provide optimal fringe contrast
- pay attention to carefully align the cameras after changing the intensity ratio of channels
- use high intensity resolution cameras to increase intensity modulation
- develop and apply an algorithm to automatically detect optimal cut-off frequency for the low-pass frequency filter
- average several measurements to reduce uncertainty of the mean

(3) Outlook

For the future, several simplifications may be expected. They include smaller and cheaper lasers offering more power as well as cheaper but more sensitive (10bit), high resolution cameras that offer special features like very fast frame acquisition. Together with phase-shifters made of very fast polarization rotators (45° - rotation of the crystal's fast axis in several microseconds) a revival of temporal phase-stepping using two 90° phase-stepped interferograms is in sight. They would combine simple setup, low processing complexity and high speed with large measurement range, high spatial resolution and low phase measurement uncertainties.

Further, with the spread of the IEEE 1394 standard (Firewire) most of the today's frame grabbers become obsolete which helps to simplify the programming of computer hardware.

Together, these advances in technology are expected to cause a migration of ESPI measurements from the laboratory to the shop floor and, hopefully, wide acceptance in industry.

Appendix A: Interferometric Metrology

In two-beam interferometry two coherent waves from one source are superposed. Let

$$\begin{aligned}\vec{E}_{\mathrm{O}}(\vec{r},t) &= \mathrm{Re}\left\{\vec{E}_{\mathrm{O0}}\, e^{j(2\pi f_{\mathrm{O}} t - \vec{k}_{\mathrm{O}}\vec{r} + \Phi_{\mathrm{O}})}\right\} \\ \vec{E}_{\mathrm{R}}(\vec{r},t) &= \mathrm{Re}\left\{\vec{E}_{\mathrm{R0}}\, e^{j(2\pi f_{\mathrm{R}} t - \vec{k}_{\mathrm{R}}\vec{r} + \Phi_{\mathrm{R}})}\right\}\end{aligned} \tag{A1}$$

denote the electrical field strength of object and reference wave respectively at position $\vec{r} = (x,y,z)^T$ and at time *t*. $\vec{E}_{O0}$ and $\vec{E}_{R0}$ are the amplitudes of the waves, $f_{\mathrm{O}}, f_{\mathrm{R}}$ specify the frequencies of the waves and $\vec{k}_{\mathrm{O}}, \vec{k}_{\mathrm{R}}$ indicate the wave vectors on the location of superposition. The wave vectors are assumed to be real and equal to

$$\vec{k}_{\mathrm{O}} = \frac{2\pi}{\lambda_{\mathrm{O}}}\vec{m}_{\mathrm{O}} \quad \text{and} \quad \vec{k}_{\mathrm{R}} = \frac{2\pi}{\lambda_{\mathrm{R}}}\vec{m}_{\mathrm{R}} \tag{A2}$$

where λ_{O}, λ_{R} are the wavelengths in the propagation medium and $\vec{m}_{\mathrm{O}}, \vec{m}_{\mathrm{R}}$ are unitary vectors in $\vec{k}_{\mathrm{O}}, \vec{k}_{\mathrm{R}}$ direction respectively. Φ_{O} and Φ_{R} denote the phase angles achieved before superposition. They include initial phase Φ_{O0}, Φ_{R0} at the origin, phase Φ_{OP_O}, Φ_{OP_R} due to the optical path followed so far, as well as π-phase jumps caused by eventual external reflections.

$$\begin{aligned}\Phi_{\mathrm{O}} &= \Phi_{\mathrm{O0}} + \Phi_{OP_O} + \pi i \quad \text{with} \quad \Phi_{OP_O} = \frac{2\pi}{\lambda_{\mathrm{O}}} GP_{\mathrm{O}}, \quad i = 0,1,2... \\ \Phi_{\mathrm{R}} &= \Phi_{\mathrm{R0}} + \Phi_{OP_R} + \pi i \quad \text{with} \quad \Phi_{OP_R} = \frac{2\pi}{\lambda_{\mathrm{R}}} GP_{\mathrm{R}}\end{aligned} \tag{A3}$$

GP_O and GP_R denote the geometrical path taken by the object and reference beam respectively.
The first simplification made assumes that only linearly polarized waves are superposed. Hence, the scalar form suffices

$$\begin{aligned}E_{\mathrm{O}}(\vec{r},t) &= \mathrm{Re}\left\{E_{\mathrm{O0}}\, e^{j(2\pi f_{\mathrm{O}} t - \vec{k}_{\mathrm{O}}\vec{r} + \Phi_{\mathrm{O}})}\right\} \\ E_{\mathrm{R}}(\vec{r},t) &= \mathrm{Re}\left\{E_{\mathrm{R0}}\, e^{j(2\pi f_{\mathrm{R}} t - \vec{k}_{\mathrm{R}}\vec{r} + \Phi_{\mathrm{R}})}\right\}\end{aligned} \tag{A4}.$$

Interferometric metrology exploits the possibility that the quantity to be measured affects the two coherent waves differently before their superposition. The intensity of the superposition is

$$I(\vec{r},t) \propto \left(\vec{E}_{\mathrm{O}} + \vec{E}_{\mathrm{R}}\right)\left(\vec{E}_{\mathrm{O}} + \vec{E}_{\mathrm{R}}\right)^{*}(\vec{r},t) = I_{\mathrm{O}} + I_{\mathrm{R}} + 2\sqrt{I_{\mathrm{O}} I_{\mathrm{R}}}\cos\left(2\pi\Delta f t - \vec{k}'\vec{r} + \Phi\right) \tag{A5}$$

with $\Delta f = f_{\mathrm{O}} - f_{\mathrm{R}}$, $\vec{k}' = \vec{k}_{\mathrm{O}} - \vec{k}_{\mathrm{R}}$ and $\Phi = \Phi_{\mathrm{O}} - \Phi_{\mathrm{R}}$ indicating the quantities that may affect interference phase. Defining the mean intensity $I_{\mathrm{m}} = I_{\mathrm{O}} + I_{\mathrm{R}}$ and the visibility $V = 2\sqrt{I_{\mathrm{O}} I_{\mathrm{R}}}/(I_{\mathrm{O}} + I_{\mathrm{R}})$, equation (A5) yields

$$I(\vec{r},t) = I_{\mathrm{m}}\left(1 + V\cos\left(2\pi\Delta f t - \vec{k}'\vec{r} + \Phi\right)\right) \tag{A6}.$$

To account for a loss of visibility of the interference pattern due to limited coherence of the source, one usually introduces the complex degree of coherence [12] $|\gamma|$ and the visibility in equation (A6) can be rewritten as

$$V = \frac{2\sqrt{I_{\mathrm{O}} I_{\mathrm{R}}}}{I_{\mathrm{O}} + I_{\mathrm{R}}}|\gamma|; \qquad 0 \le |\gamma| \le 1 \tag{A7}.$$

Appendix B: Multiplexer Board

Nr	Code	Description
6 x	MM74HC157	CMOS high speed Quad 2-to-1 data selector/Multiplexers
44 x	R	Resistance, R = 47 Ω, ¼ W
44 x	D1	Zener Diode, U_z = 3 V, P_{tot} = 1W
44 x	D2	Schottky Diode

Pixel clock CLK = 14.31818 MHz

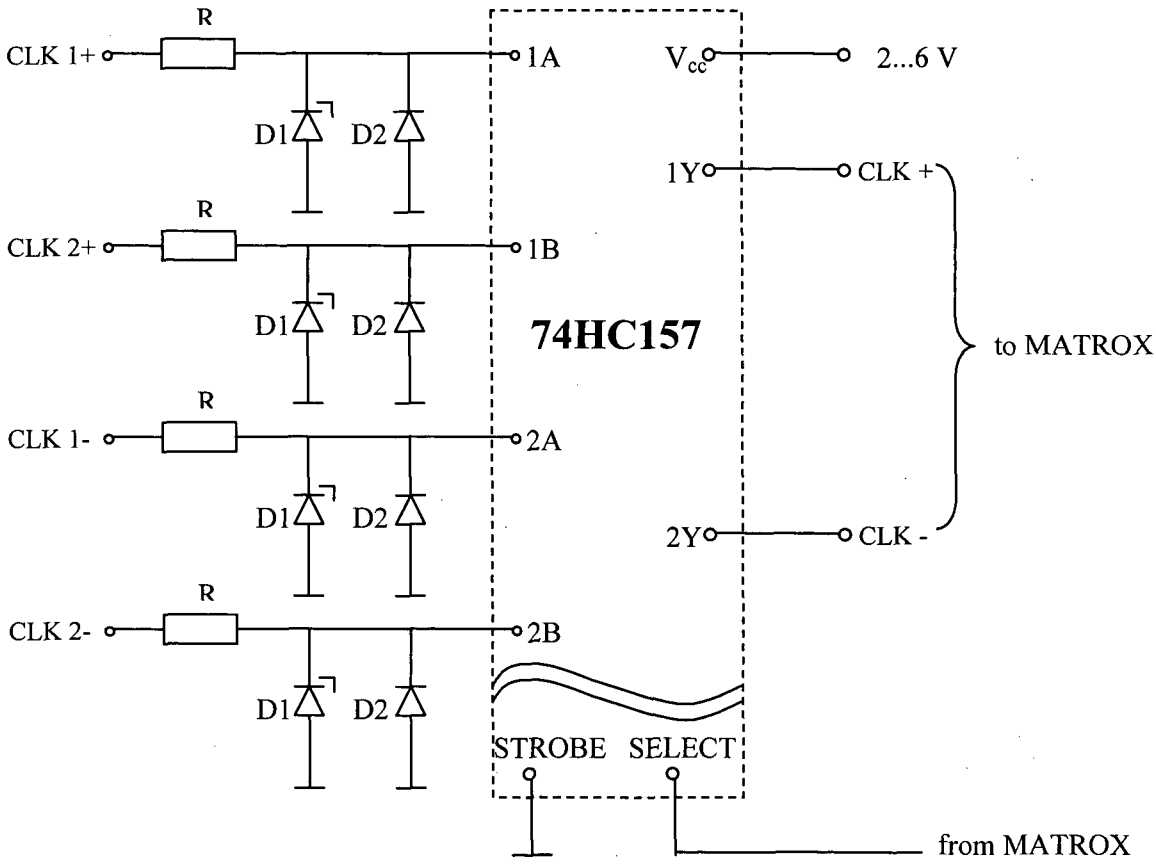

Bibliography

/1/ Ai, C., Wyant, J. C., "Effect of piezoelectric transducer non-linearity on phase shift interferometry,"Appl. Opt. **26**, No. 6, 1112-1116 (1987)

/2/ Bennett, J. M., Bennett, H. E., "Handbook of Optics," section 10, Optical Society of America McGraw-Hill (1978)

/3/ Bergmann, Schaefer, "Lehrbuch der Experimentalphysik," Band III Optik, 7. Aufl. Walter deGruyter Berlin, New York (1978)

/4/ Brotzeit, A., Hinsch, K. D., "Actively phase-compensated fiber-optic electronic speckle pattern interferometer (ESPI) for long-term in-situ measurements," SPIE Vol. 2860, 144-149, San Diego (1996)

/5/ Butters, J. N., Leendertz, J. A., "Holographic and Video Techniques Applied to Engineering Measurements," J. Meas. Control. **4**, 349-354 (1971)

/6/ Colucci, D., Wizinowich, P., "Millisecond phase acquisition at video rates," Appl. Opt. **31**, No. 28, 5919-5925 (1992)

/7/ Creath, K., "Phase-shifting speckle interferometry," Appl Opt. **24**, No.18, 3053-3058 (1985)

/8/ Creath, K., "Phase-measurement techniques for nondestructive testing," SEM Proceedings, 473-479, Baltimore (1990)

/9/ de Groot, P. J., "Vibration in phase-shifting interferometry," J. Opt. Soc. Am. **12**, No.2, 354-365 (1995)

/10/ Donati, S., Martini, G., "Speckle-pattern intensity and phase: Second-order conditional statistics," J. Opt. Soc. Am. **69**, No.12, 1690-1694 (1979)

/11/ Galanulis, K., et al., "Active Stabilization of ESPI Systems for Application under Rough Conditions," SPIE Vol. 2545, 103-107, San Diego (1995)

/12/ Gasvik, K. J., "Optical Metrology," John Wiley & Sons, 2nd edition (1995)

/13/ Gilbert, J. A., Matthys, D. R., Greguss, P., "Optical measurements through panoramic imaging systems," and references therein, SEM Proceedings, 164-171, Baltimore (1990)

/14/ Gilbert, J. A., Matthys, D. R., Hendren, C. M., "Displacement analysis of the interior walls of a pipe using panoramic holo-interferometry," SPIE Vol. 1554B, 128-134, San Diego (1991)

/15/ Gonçalves Jr., A. A., "Generalized least squares approach to compute displacements, strains and rotations from combined single and/or double illumination holographic interferometry," SPIE Vol. 2004,80-89, San Diego (1993)

/16/ Gonçalves Jr., A. A., "Measurement of radial deformation of a long internal cylinder using ESPI," to be published

/17/ Goodman, J. W., "Some fundamental properties of speckle," J.Opt.Soc.Am. **66,** No.11, 1145-1150 (1976)

/18/ Greguss, P., U.S. Patent No.4,566,763, (1984)

/19/ Haferkorn, "Technische Optik," Technik Verlag Berlin, (1996)

/20/ Höfling, R., Osten, W., "Displacement measurement by image-processed speckle patterns," J. Mod. Opt. **34**, No. 5, 607-617 (1987)

/21/ Hrebabetzky, F., "Computer-Controlled, Active Phase Stabilization for Electronic Holography," SPIE Vol. 2861, 152-162, San Diego (1996)

/22/ Hung, Y. Y., "Electronic Shearography versus ESPI for Nondestructive Evaluation," SPIE Vol. 1554B, 692-700, San Diego (1991)

/23/ Huntley, J. M., "Random phase measurement errors in digital speckle pattern interferometry," SPIE Vol. 2544, 246-257, San Diego (1995)

/24/ ISO DP4846

/25/ ISO 2372, "Mechanical vibrations of machines with operating speeds from 10 to 200 rev/s-Basis for specifying evaluation standards," International Organization of Standardization, (1974)

/26/ ISO 2631, "Guide for the evaluation of human exposure to whole-body vibration," International Organization of Standardization, (1978)

/27/ Jenoptik GmbH, Jena, Online Product Catalogue: www.jenoptik.com

/28/ Jin, G. C., Bao, N. K., Chung, P. S., "A new Computer-controlled Polarization Phase-Shifting Technique," SPIE Vol. 2066, 67-71, Boston (1993)

/29/ Joenathan, C., Khorana, B. M., "A simple and modified ESPI system," Optik **88**, No. 4, 169- 171 (1991)

/30/ Joenathan, C., Khorana, B. M., "Quasi-equal-path electronic speckle pattern interferometric system," App. Opt. **32**, No. 29, 5724-5726 (1993)

/31/ Joenathan, C., "Phase-measuring interferometry: new methods and error analysis," Appl. Opt. **33**, No. 19, 4147-4155 (1994)

/32/ Jones, R., Wykes, C., "Holographic and Speckle Interferometry," Cambridge University Press, 2nd edition (1989)

/33/ Kaufmann, G. H., Ruiz, P. D., Galizi, G. E., "Recent developments in double-pulsed video speckle interferometry and its application to the measurement of high speed transient deformations", Proceedings Laser Metrology for Precision Measurement and Inspection in Industry, Florianópolis, pp. 4.43-4.51, Brazil (1999)

/34/ Kerr, D., Santoyo, F. M., Tyrer, J. R., "Extraction of phase data from electronic speckle pattern interferometric fringes using a singel-phase-step method: a novel approach," J. Opt. Soc. Am. A **7**, No. 5, 820-826 (1990)

/35/ Kinnstaetter, K., Lohmann, A. W., Schwider, J., Streibl, N., "Accuracy of phase shifting interferometry," Appl. Opt. **27**, No.24, 5082-5089 (1988)

/36/ Kothiyal, M. P., Delisle, C., "Shearing interferometer for phase shifting interferometry with polarization phase shifter," Appl. Opt. **24**, No. ?, 4439-4442 (1985)

/37/ Kreis, T. M., Geldmacher, J., "Evaluation of interference patterns: a comparison of methods," SPIE Vol. 1554B, 718-724, San Diego (1991)

/38/ Kujawinska, M., *and ref. therein*, "Spatial phase measurement methods, " in Interferogram Analysis, D. W. Robinson and G. T. Reid, pp 141-193, Institute of Physics, Bristol, 1993

/39/ Maak, T., Kowarschik, R., "Camera influence on the phase-measurement accuracy of a phase-shifting speckle interferometer," Appl. Opt. **35**, No. 19, 3514-3524 (1996)

/40/ Macovski, A., Ramsey, D., Schaefer, L. F., "Time Lapse Interferometry and Contouring Using TV System," Appl. Opt. **10**, 2722-2727 (1971)

/41/ Mahr GmbH Göttingen, Optics Product Catalogue (1998)

/42/ Malacara, "Experimental Mechanics," Wiley, (1996)

/43/ Meadowlark Optics Product Catalogue (1996)

/44/ Melozzi, M., Pezatti, L., Mazzoni, A., "Vibration-insensitive interferometer for on-line measurements," Appl. Opt. **34**, No. 25, 5595-5601 (1995)

/45/ Mizunuma, M., Ogawa, S., Kuwano, H., "Deformation detection on the pipe inner wall using a laser-beam scanning displacement sensor," SPIE Vol. 2066, 98-105, Boston (1993)

/46/ Moore, A. J., Tyrer, J. R., Santoyo, F. M., "Phase extraction from electronic speckle pattern interferometry addition fringes," and references therein, Appl. Opt.**33**, No. 31, 7312-7320 (1994)

/47/ Nakadate, S., Saito, H., "Fringe scanning speckle-pattern interferometry" Appl. Opt. **24**, No 14, 2172-2180 (1985)

/48/ Owner-Petersen, M., "Decorrelation and fringe visibility: on the limiting behavior of various electronic speckle-pattern correlation interferometers," J.Opt.Soc.Am. A **8**, No 7, 1082-1089 (1991)

/49/ Owner-Petersen, M., "Digital speckle pattern shearing interferometry: limitations and prospects," Appl. Opt. **30**, No. 19, 2730-2738 (1991)

/50/ Peng, S., Joenathan, C., Khorana, B. M., "Quasi-equal-path electronic speckle pattern interferometric system," Opt. Letters **17**, No.15, 1040-1042 (1992)

/51/ Polarite Ltd., Chino, Technical Note (1997)

/52/ Rodriguez-Vera, R., Barrientos, B., Moore, A. C., "Spatial phase-stepping using a computer-generated diffractive element," Proceedings Laser Metrology for Precision Measurement and Inspection in Industry, Florianópolis, pp. 4.64-4.76, Brazil (1999)

/53/ Sesselmann, M., Gonçalves Jr., A. A., "Single phase-step algorithm for phase difference measurement using ESPI," In. INTERNATIONAL SYMPOSIUM ON OPTICAL SCIENCE, ENGINEERING AND INSTRUMENTATION, Proceedings SPIE, Vol. 3478 , pp. 153 –159 San Diego, (1998)

/54/ Sesselmann, M., Gonçalves Jr., A. A., "A robust spatial phase-stepping ESPI system," Proceedings Laser Metrology for Precision Measurement and Inspection in Industry, Florianópolis, pp. 4.52-4.57, Brazil (1999)

/55/ Slettemoen, G. A., "General analysis of fringe contrast in electronic speckle pattern interferometry," Opt. Acta **28**, No. 3, 313-327 (1979)

/56/ Slettemoen, G. A., Wyant, J. C., "Maximal fraction of acceptable measurements in phase-shifting speckle interferometry: a theoretical study," J. Opt. Soc. Am. A **3**, No. 2, 210-214 (1986)

/57/ Stefani, S. A., Nagarajah, C. R., Toncich, D. J., "Non-Contact Inspection for the Detection of Internal Surface Defects in Hollow Cylindrical Work-Pieces," Int. J. Adv. Manuf. Tecnol. **11,** 146-154 (1996)

/58/ Troncoso, L. H. S., *and ref. therein*, "Desenvolvimento de um Sistema Ativo de Estabilização para Holografia Eletrónica," Tése de Doutorado, Florianópolis (1998)

/59/ van Haasteren, A. J. P., Frankena, H. J., "Real-time displacement measurement using multi-camera phase-stepping speckle interferometer," Appl. Opt. **33**, No.19, 4137-4142 (1994)

/60/ VDI-Berichte 749, "Laser-Interferometrie in der industriellen Messtechnik," Tagung Braunschweig, 26. und 27. April 1989, VDI Verlag Duesseldorf (1989)

/61/ Vikram, C. S., Witherow, W. K., Trolinger, J. D., "Algorithm for phase-difference measurement in phase-shifting interferometry," Appl. Opt. **32**, No. 31, 6250-6252 (1993)

/62/ Vry, U., Fercher, A. F., "Higher-order statistical properties of speckle fields and their application to rough-surface interferometry," J. Opt. Soc. Am. A **3**, No. 7, 988-1000 (1986)

/63/ Wizinowich, P. L., "Phase shifting interferometry in the presence of vibration: a new algorithm and system," Appl. Opt. **29**, No. 22, 3271-3279 (1990)

/64/ Wu, X., Pang, L., Zhang, H., "New optical head and system of ESPI," SPIE Vol. 2003, 410-413, San Diego (1993)